UC San Diego

UC San Diego Electronic Theses and Dissertations

Title

Direct Numerical Simulation of Cosmological Reionization /

Permalink

https://escholarship.org/uc/item/15x851r0

Author

So, Geoffrey C.

Publication Date

2013

Peer reviewed|Thesis/dissertation

eScholarship.org Powered by the California Digital Library
University of California

UNIVERSITY OF CALIFORNIA, SAN DIEGO

Direct Numerical Simulation of Cosmological Reionization

A dissertation submitted in partial satisfaction of the
requirements for the degree
Doctor of Philosophy

in

Physics with Specialization in Computational Science

by

Geoffrey C. So

Committee in charge:

Professor Michael L. Norman, Chair
Professor Randolph Bank
Professor Kim Griest
Professor Dušan Kereš
Professor Jeffrey Rabin

2013

Copyright
Geoffrey C. So, 2013
All rights reserved.

The dissertation of Geoffrey C. So is approved, and it is acceptable in quality and form for publication on microfilm and electronically:

_____

_____

_____

_____

_____
Chair

University of California, San Diego

2013

DEDICATION

To the future of astrophysics and cosmology.

EPIGRAPH

Dream not of today
—Prof. Richard Galen
To boldly go,
where no one has gone before.
—Capt. Jean-Luc Picard

TABLE OF CONTENTS

LIST OF FIGURES

LIST OF TABLES

ACKNOWLEDGEMENTS

Thanks to Feifei, family, friends, colleagues, teachers, committee members, and an advisor who radiates wisdom and illuminates those around him.

The following papers are used in the thesis, so I want to also thank the coauthors Dr. Michael Norman my advisor, Dr. Daniel Reynolds, and Dr. Robert Harkness (who unfortunately passed away), for all their hard work that made this thesis possible.

Chapter 2 is a reprint of a paper submitted to Astrophysical Journal without the abstract, M. L. Norman, D. R. Reynolds, R. P. Harkness, and G. C. So, "Direct Numerical Simulation of Reionization I: Numerical Methods and Tests", (submitted ApJ), (2013).

Chapter 3 is a reprint of a paper submitted to Astrophysical Journal without the abstract, G. C. So, M. L. Norman, D. R. Reynolds, and R. P. Harkness,"Direct Numerical Simulation of Reionization II: Clumping Factor Evolution and the Photon Budget for Reionization", (submitted ApJ), (2013).

Thanks to the universe for being ionized.

VITA

2005	B. S. in Physics, University of California, San Diego
2002-2007	Teaching Assistant, University of California, San Diego
2013	Ph. D. in Physics, University of California, San Diego

PUBLICATIONS

G. C. So, M. L. Norman, D. R. Reynolds, and R. P. Harkness,"Direct Numerical Simulation of Reionization II: Clumping factor evolution and the photon budget for reionization", (submitted ApJ), (2013).

G. C. So, M. L. Norman, D. R. Reynolds, and R. P. Harkness,"Direct Numerical Simulation of Reionization III: Effects of Radiative Feedback on Star Formation", (in preparation ApJ), (2013).

M. L. Norman, D. R. Reynolds, R. P. Harkness, and **G. C. So**, "Direct Numerical Simulation of Reionization I: Numerical Methods and Tests", (submitted ApJ), (2013).

Enzo Collaboration: G. L. Bryan, M. L. Norman, B. W. O'Shea, T. Abel, J. H. Wise, M. J. Turk, D. R. Reynolds, D. C. Collins, P. Wang, S. W. Skillman, B. Smith, R. P. Harkness, J. Bordner, J. Kim, M. Kuhlen, H. Xu, N. Goldbaum, C. Hummels, A. G. Kritsuk, E. Tasker, S. Skory, C. M. Simpson, O. Hahn, J. S. Oishi, **G. C So**, F. Zhao, R. Cen, Y. Li, "Enzo: An Adaptive Mesh Refinement Code for Astrophysics", (submitted ApJ), (2013)

M. L. Norman, D. R. Reynolds, and **G. C. So**, "Cosmological radiation hydrodynamics with enzo", in American Institute of Physics Conference Proceedings, vol. 1171, pp.260-272, (2009)

D. Kirkman, D. Tytler, N. Suzuki, C. Melis, S. Hollywood, K. James, **G. C. So**, D. Lubin, T. Jena, M. L. Norman, and P. Paschos, "The HI opacity of the intergalactic medium at redshifts $1.6 < z < 3.2$", MNRAS, (2005).

T. Jena, M. L. Norman, D. Tytler, D. Kirkman, N. Suzuki, A. Chapman, C. Melis, P. Paschos, B. O'Shea, **G. C. So**, D. Lubin, W. Lin, D. Reimers, E. Janknecht, and C. Fechner,"A concordance model of the lyman α forest at z= 1.95", MNRAS, (2005).

ABSTRACT OF THE DISSERTATION

Direct Numerical Simulation of Cosmological Reionization

by

Geoffrey C. So

Doctor of Philosophy in Physics with Specialization in Computational Science

University of California, San Diego, 2013

Professor Michael L. Norman, Chair

We examine the epoch of hydrogen reionization using a new numerical method that allows us to self-consistently couple all the relevant physical processes (gas dynamics, dark matter dynamics, self-gravity, star formation/feedback, radiative transfer, ionization, recombination, heating and cooling) and evolve the system of coupled equations on the same high resolution mesh. We refer to this approach as *direct numerical simulation*, in contrast to existing approaches which decouple and coarse-grain the radiative transfer and ionization balance calculations relative to the underlying dynamical calculation. Our method is scalable with respect to the number of radiation sources, size of the mesh, and the number of computer processors employed, and is described in Chapter 2 of this thesis. This scalability permits us to simulate cosmological reionization in large cosmological

volumes ($\sim$ 100 Mpc) while directly modeling the sources and sinks of ionizing radiation, including radiative feedback effects such as photoevaporation of gas from halos, Jeans smoothing of the IGM, and enhanced recombination due to small scale clumping.

With our fiducial simulation, we find that roughly 2 ionizing photons per baryon is needed to highly ionize the intergalactic medium. The complicated events during reionization that lead to this number can be generally described as inside-out, but in reality the narrative depends on the level of ionization of the gas one defines as ionized. We have updated the formula observers often use for estimating the ionized volume filling fraction formula with a δ_b and $t_{rec,eff}$ to get from $O(10\%)$ to $O(1\%)$ consistency with our simulation results. This improvement comes from not using the traditional clumping factor, but instead, considering the history and local effects which were neglected in formulating the original expression. And finally, we have a new upper limit for the escape fraction of ~ 0.6 from our simulation, which takes into account the photons in the energy density field and photons used to ionize H I.

Chapter 1

Introduction

1.1 What is Cosmological Reionization?

Immediately after the Big Bang, the universe was filled with a mix of subatomic particles, and as the universe expanded and cooled, the particles including electrons eventually formed larger particles such as protons and neutrons. As the universe cooled further, the protons, neutrons and electrons combined to form neutral hydrogen (H I) and some small fraction of them formed neutral helium (He I). Due to the presence of electrons in these neutral atoms, the universe remained opaque to radiation. When the first generation of stars population three (Pop III) formed, radiation emitted by them was absorbed by the surrounding neutral atoms, bumping the atoms' electrons to a higher energy level. When the energy of a given photon was sufficient, it even ionized the atom it encountered by knocking the electron free from the nucleus altogether. With some of the electrons freed from the nucleus of atoms that formed the intergalactic medium (IGM), which was mostly hydrogen, radiation could then penetrate deeper into the IGM. Having ionized more of the IGM, the radiation from stars caused bigger and bigger bubbles of ionized atoms to form. Finally, these bubbles which were virtually transparent to radiation grew over time, until they overlapped and engulfed the entire universe. With the universe mostly transparent, radiation emanating from different sources can then reach us, enabling us to see distant galaxies, quasars, along with other celestial objects in the sky. Since this was the second time in the history of the

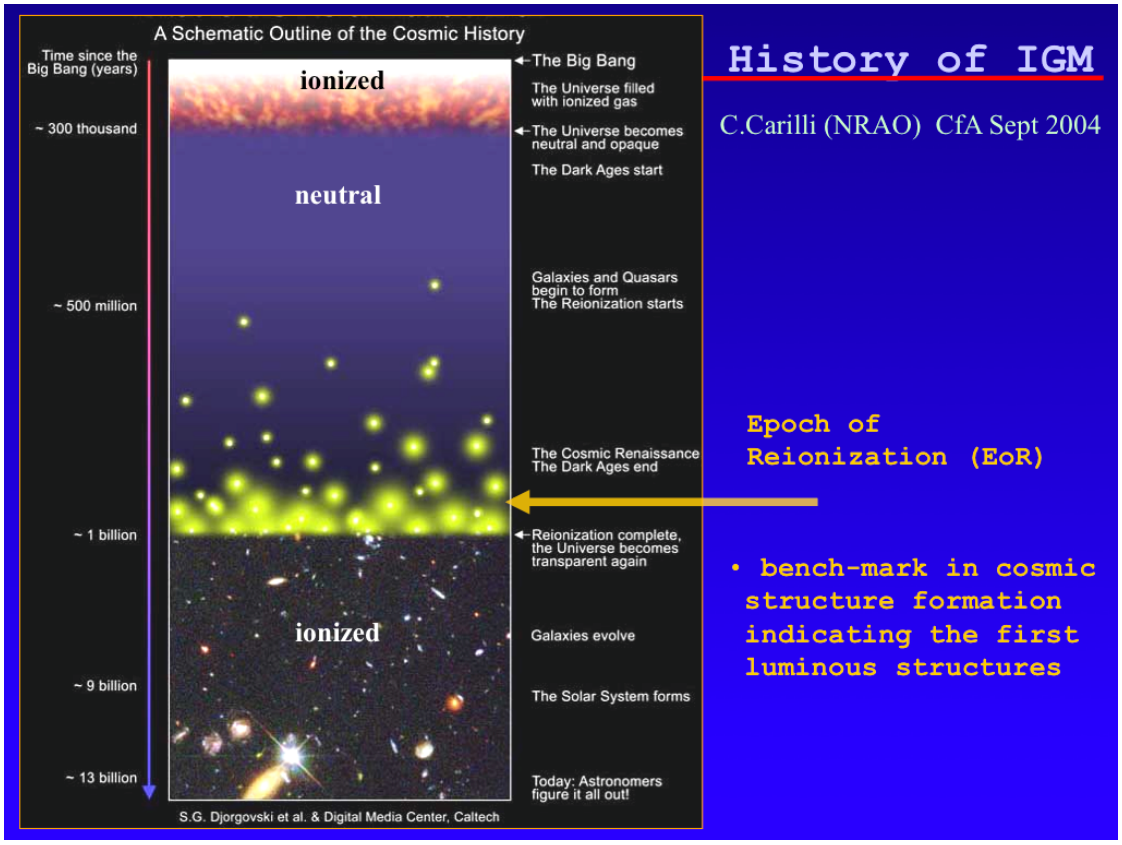

Figure 1.1: History of the universe slide from Carilli (2004). We are focusing on EoR which occured after the "Dark Ages" and before the universe becomes transparent due to radiation from star forming galaxies.

universe where the electrons and protons were separated as ions, we call the process of reaching this second ionized phase of the universe the "Epoch of Reionization" (EoR).

In Figure 1.1, a brief history of the universe is shown (Carilli, 2004). Before any stars formed during EoR, there were no sources of light in the universe, so astronomers termed it the "Dark Ages". Eventually, the universe was able to form more stars that then cluster into galaxies. These galaxies increased in number and emitted enough energetic photons ionize their surroundings, and eventually ionized the universe, so that present day astronomers can look far into the distant past.

1.2 Observational Constraints on Cosmological Reionization

Observers have long sought to understand the evolutionary history of the universe with deep observations of objects far away. However, photons able to reach instruments have to penetrate through the intervening IGM between the sources of the radiation and telescopes. Generally speaking there are two types of indicators that the observers look for when determining the time scale for EoR. First, the more often studied one, is Lyman alpha absorption. These are photons that came from quasar emission and passed through some neutral hydrogen on their way to our telescopes. The high energy photons of the right wavelength and frequency, ~ 1216Å in the UV portion of the spectrum or 2.47×10^{15}Hz, when passing through neutral hydrogen can excite the atom from the quantum ground (n=1) state to the first excited (n=2) state. This excitation will be seen as an absorption line dip in the spectrum formed by the photons. Summing over all the absorption lines, which are each redshifted according to their distance, over a redshift interval Δz gives a mean amount of absorption per unit redshift. Transmission is defined as 1 minus the mean absorption. Figure 1.2 is a graph showing the transmission from quasars at varying redshifts z.

The transmission decreases as z increases. The transmission drops by small amounts between $2 < z < 5$, and dips sharply at $z \sim 6$. The sudden dip in transmission is interpreted as an increase of neutral hydrogen in the IGM at $z \gtrsim 6$. Since only a small (10^{-4} to 10^{-3}) fraction of neutral hydrogen is enough to cause a transmission gap at the rest frame of Lyman α, these photons are not able to show us information when the universe is significantly neutral during EoR, only the z of when EoR approximately ended.

Another observation indicator that constrains the EoR is the Thomson optical depth ($\tau_{\rm T}$) from scattering of cosmic microwave background (CMB) photons off of free electrons. The free electrons came from the EoR when hydrogen was ionized by UV radiation. This scatting will reduce the anisotropy of the CMB signal on all scales, and create a polarization signal on large angular scales. The

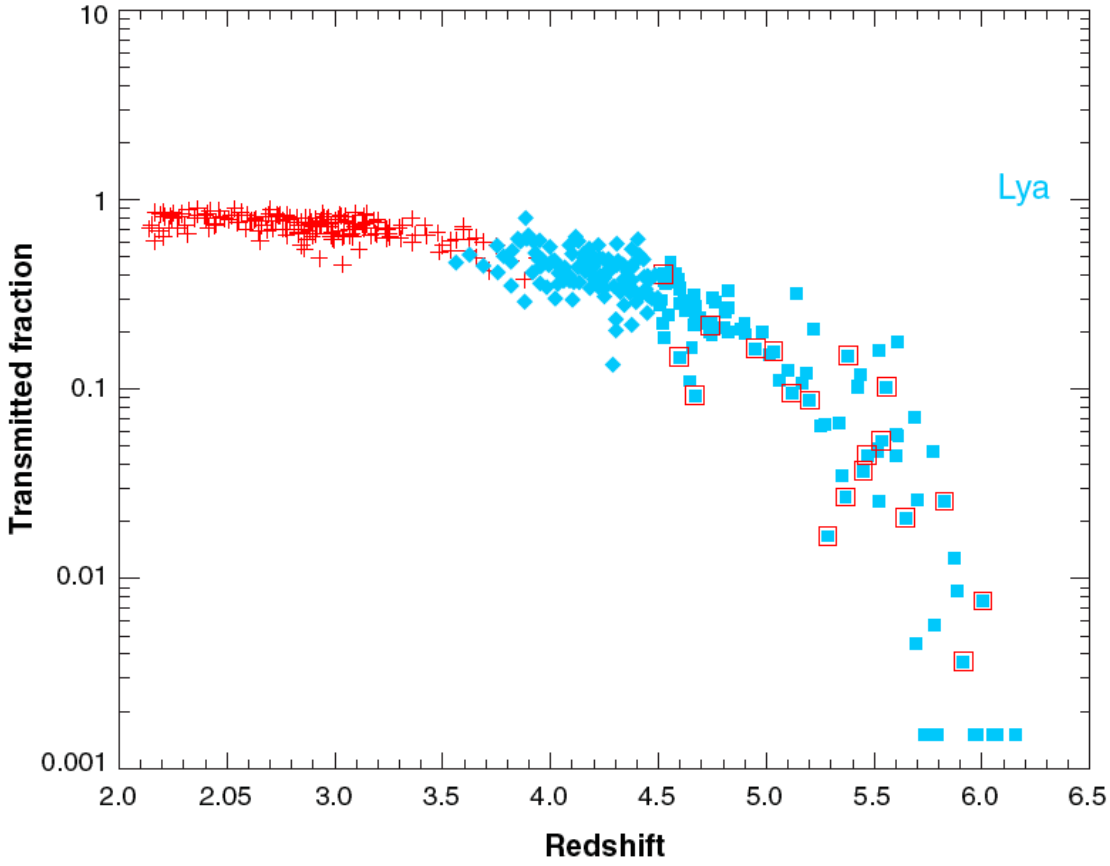

Figure 1.2: Plot of normalized quasar lyman alpha transmission, adapted from Songaila (2004); Fan et al. (2006). *Blue*: Broad absorption line spectrum, *Red*: Normalized by the peak transmission

latest estimation of the optical depth is $\tau_{\rm T} = 0.088 \pm 0.015$ from WMAP7 (Komatsu et al., 2011). For an instantaneous reionization model, where the universe transforms from completely neutral to completely ionized at an instant in time, this model predicts a $z_{\rm reion} = 10.6 \pm 1.2$. However, since we believe from theory and simulations that reionization from sources happens with a patchy history, starting from isolated patches instead of uniformly all at once, this may be seen as the beginning of EoR, when the universe became significantly ionized.

Besides the transmission of the quasars as a whole, observers also look at the individual spectrum. Given enough absorption along the line of sight at different z, this can cause the quasar spectrum to have a transmission gap. Since the photon wavelength will be redshifted, the latest absorption will be at 1216Å, while the absorption features that happened before will now be redshifted to slightly longer than 1216. When many of these dips overlap, they form the transmission gap called the Gunn-Peterson trough (Gunn & Peterson, 1965). Looking at when the trough indicates complete absorption also tells us when the neutral hydrogen increases in density.

The UV luminosity function of high redshift galaxies is another way to put limits on what the likely conditions were during EoR (Fan et al., 2006; Bolton & Haehnelt, 2007; Bouwens et al., 2007, 2012; Robertson et al., 2013). They use the Madau et al. (1999) prescription to predict how many photons are needed to keep the universe ionized. This lower limit on the number of photons translates to an estimate of what the UV luminosity function has to be. We use this as a calibration guide for how representative our simulations are compared to the real world universe. Considering all the observational evidence, they suggest the EoR began before $z \sim 11$ and completed by $z \sim 6$.

1.3 Models of Cosmological Reionization

The basic series of events during EoR is that galaxies form in the peaks of the dark matter density field and drive expanding ionized hydrogen (H II) regions into their surroundings by virtue of the UV radiation emitted from young, massive

stars. These H II regions are initially isolated, but begin to merge into larger, Mpc-scale H II regions due to the clustering of the galaxy distribution (expansion phase). Driven by a steadily increasing global star formation rate and recombination time (due to cosmic expansion) this process goes on until H II regions completely engulf the universe (overlap phase). In this picture, rare peaks in the density field ionize first while regions of lower density ionize later from local sources that themselves formed later. In this picture, referred to as "inside-out reionization", void regions are the last to ionize because they have few local sources of ionization and remain neutral until an I-front from a denser region has swept over them.

The theoretical and simulation communities have tried hard to develop models and theories to describe the reionization process while satisfying the observational constraints. Due to the high computation cost of doing fully self-consistent 3D simulation of the multi-physics phenomena, there have been many efforts to approximate and simplify the complicated equations involved in describing the multi-physics phenomenon that is EoR. To date numerical simulations of reionization have fallen into two basic classes (Trac & Gnedin, 2011): smallscale simulations that resolve the sources and sinks of ionizing radiation; and large-scale simulations that account for the diversity and clustering of sources. While ideally one would like to do both in a single simulation, this has not been feasible until now owing to numerical limitations. Historically, small-scale simulations came first. These simulations self-consistently modeled galaxy formation, radiative transfer, and photoionization/recombination within a hydrodynamic cosmological code. Comoving volumes were typically $(10\mathrm{Mpc})^3$ with spatial resolution of a few comoving kpc sufficient to resolve high redshift dwarf galaxies and the baryonic cosmic web (Gnedin, 2000a; Razoumov et al., 2002; Ricotti et al., 2002; Petkova & Springel, 2011b; Finlator et al., 2012). Large-scale simulations followed, however these were not self-consistent radiation hydrodynamic cosmological simulations. Rather, density fields were simulated with a cosmological N-body or hydrodynamics code, and then ionization was computed in a post-processing step using a standalone radiative transfer code, typically a Monte Carlo or ray-tracing code (Ciardi et al., 2001; Sokasian et al., 2003; Iliev et al., 2006; Zahn et al., 2007a; Trac & Cen, 2007; Trac

et al., 2008; Shin et al., 2008; Finlator et al., 2009b). Additionally, a trend towards more realistic and self consistent treatment of dark matter and baryonic matter along with radiation transport emerged (Zahn et al., 2007a; Petkova & Springel, 2011a).

1.4 Open Questions

Despite the progress that has been made on understanding the process of cosmic reionization, there remains a considerable number of open ended questions that require further observation and theory/simulation results to confirm and answer. Some such questions are, how did the energetic photons ionize the IGM? What is the role of radiative feedback on suppressing star formation in low mass galaxies, and on EoR? How reliable are current analytical models that describe features during EoR? What is the detailed topology of the ionization front during EoR? What is the escape fraction of ionizing photons coming from inside source galaxies? What are the mass functions of these galaxies? What are the effects of X-ray pre-heating and how do different types of stars, and other radiation sources affect EoR? What is the optical depth of the universe during EoR? There are many other mysteries about EoR that we do not yet understand, the ones listed here are just some of the more hotly researched topics. We will not attempt to answer all the questions at once, and will be focusing on a few specific aspects of EoR here.

1.5 This Thesis

This thesis will address the first few of the open-ended question listed before: How do the energetic UV photons ionize the neutral intergalactic medium? What is the role of radiation feedback on suppressing star formation in low mass galaxies, on EoR? And how reliable are current analytical models that describe the EoR? We propose to use a similar implementation as (Petkova & Springel, 2011a), by adopting Flux Limited Diffusion (FLD) scheme to approximate radiation transport, with Enzo as the code base (The Enzo Collaboration et al., 2013).

Instead of assuming that baryons follow dark matter like previous researchers, we now calculate the radiation hydrodynamics with the FLD module, coupling the the two forms of matter together. In this way, the interaction between dark matter, baryons and the presence of radiation are all coupled together during the calculation consistently, instead of being separate effects. With the FLD approximation, we do not have to solve the exact expensive radiation transport equation which is still computationally infeasible. Compared with traditional large box simulations where radiation transport is post-processed, the FLD approximation will give us a better handle of absorption due to small scale inhomogeneities and photo-evaporation dynamics will be calculated self consistently. Also, we are not limited by the amount of radiating sources that can exist in the simulation, a limitation for simulations utilizing the ray-tracing method.

With the tools mentioned above, we first describe the numerical methods and various verification and validation tests in §2. We find that the method generally yields useful results in a reasonable time. We then delve into the details involving the results from our fiducial simulation in §3. Here we discuss our journey and progress in trying to answer how do the UV photons ionize the IGM with the simulated data. We find that a modified version of Madau et al. (1999) model, the one often used by observers, is able to match our simulation to the order of 1%, and along the way we realize that an instantaneous treatment of EoR is not valid because history effects cannot be ignored. In order to arrive at this level of accuracy the integrated history must be taken into account. In §4, we discuss the effects of radiation feedback. This is central in quantifying the differences in having added the radiation transport compared to a hydrodynamics and N-body simulation. We find that having radiation feedback suppresses the trend of star formation for halos with dark matter mass below $\sim 10^9 M_\odot$. The thesis ends with discussion and future work in §5.

Chapter 2

Numerical Methods and Tests

2.1 Introduction

The epoch of reionization (EoR) is a current frontier of cosmological research both observationally and theoretically. Observations constrain the transition from a largely neutral intergalactic medium (IGM) of primordial gas to a largely ionized one (singly ionized H and He) to the redshift interval $z \sim 11 - 6$, which is a span of roughly 500 Myr. The completion of H reionization by $z \approx 6$ is firmly established through quasar absorption line studies of luminous, high redshift quasars which exhibit Ly α Gunn-Peterson absorption troughs (Fan et al., 2006). The precise onset of H reionization (presumably tied to the formation of the first luminous ionizing sources) is presently unknown observationally, however CMB measurements of the Thomson optical depth to the surface of last scattering by the WMAP and Planck satellites indicates that the IGM was substantially ionized by $z \sim 11$ (Trac & Gnedin 2011; Komatsu et al. 2011; Planck Collaboration 2013) Since the optical depth measurement is redshift integrated and averaged over the sky, the CMB observations provide no information about how reionization proceeded or the nature of the radiation sources that caused it.

It is generally believed that reionization begins with the formation of Population III stars at $z \sim 20 - 30$ (Abel et al., 2002; Yoshida et al., 2003; Bromm & Larson, 2004; Sokasian et al., 2004), but that soon the ionizing photon budget becomes dominated by young, star forming galaxies (see e.g., Wise et al. (2012); Xu

et al. (2013)), and to a lesser extent by the first quasars (Trac & Gnedin, 2011). Observations of galaxies in the redshift interval $6 \leq z \leq 10$ using the Hubble Space Telecope support the galaxy reionizer hypothesis, with the caveat that the faint end of the luminosity function which contributes substantially to the number of ionizing photons has not yet been measured (Robertson et al., 2010; Bouwens et al., 2012).

Given the paucity of observational information about the *process* of cosmic reionization, researchers have resorted to theory and numerical simulation to fill in the blanks. As reviewed by Trac & Gnedin (2011), progress in this area has been dramatic, driven by a synergistic interplay between semi-analytic approaches and numerical simulations. The combination of these two approaches have converged on a qualitative picture of how H reionization proceeds assuming the primary ionizing sources are young, star-forming galaxies. The physics of the reionization process is determined by the physics of the source and sinks of ionizing radiation in an expanding universe. Adopting the ΛCDM model of structure formation, galaxies form hierarchically through the merger of dark matter halos. The structure and evolution of the dark matter density field is now well understood through ultra-high resolution numerical N-body simulations (Springel et al., 2005; Klypin et al., 2011) and through analytic models based on these simulations (Cooray & Sheth, 2002). By making certain assumptions about how ionizing light traces mass and the dynamics of HII regions, a basic picture of the reionization process has emerged (Furlanetto et al., 2004b, 2006; Iliev et al., 2006; Zahn et al., 2007a) that is confirmed by detailed numerical simulations; e.g., (Zahn et al., 2011).

The basic picture is that galaxies form in the peaks of the dark matter density field and drive expanding HII regions into their surroundings by virtue of the UV radiation emitted from young, massive stars. These HII regions are initially isolated, but begin to merge into larger, Mpc-scale HII regions due to the clustering of the galaxy distribution (expansion phase). Driven by a steadily increasing global star formation rate and recombination time (due to cosmic expansion) this process goes on until HII regions completely fill the volume (overlap phase). In this picture, rare peaks in the density field ionize first while regions of lower density ionize later

from local sources that themselves formed later. In this picture, referred to as "inside-out reionization", void regions are the last to ionize because they have few local sources of ionization and remain neutral until an I-front from a denser region has swept over it.

To date numerical simulations of reionization have fallen into two basic classes (Trac & Gnedin, 2011): small-scale simulations that resolve the sources and sinks of ionizing radiation; and large-scale simulations that account for the diversity and clustering of sources. While ideally one would like to do both in a single simulation, this has not been feasible until now owing to numerical limitations. Historically, small-scale simulations came first. These simulations self-consistently modeled galaxy formation, radiative transfer, and photoionization/recombination within a hydrodynamic cosmological code. Comoving volumes were typically $\leq (10Mpc)^3$ with spatial resolution of a few comoving kpc–sufficient to resolve high redshift dwarf galaxies and the baryonic cosmic web (Gnedin, 2000a; Razoumov et al., 2002; Ricotti et al., 2002; Finlator et al., 2012). Large-scale simulations followed, however these were not self-consistent radiation hydrodynamic cosmological simulations. Rather, density fields were simulated with a cosmological N-body or hydrodynamics code, and then ionization was computed in a post-processing step using a standalone radiative transfer code, typically a Monte Carlo or ray-tracing code (Ciardi et al., 2001; Sokasian et al., 2001, 2003; Iliev et al., 2006; Zahn et al., 2007a; Trac & Cen, 2007; Trac et al., 2008; Shin et al., 2008; Finlator et al., 2009a).

The need to simulate large cosmological volumes coupled with the cost or limited scalability of available radiative transport methods led to a trend which continues to this day of using different numerical resolutions to model the N-body dynamics and the radiative transfer/ionization calculations. For example Iliev et al. (2006a) simulate N-body dynamics in a volume 100 Mpc/h on a side with a force resolution of 31 kpc/h, while performing the RT calculation on grids with comoving resolutions of 246 and 492 kpc/h. Similarly Trac & Cen (2007,2008) and Shin, Trac & Cen (2008) achieved a force resolution of 8.7 kpc/h in N-body simulations in 50 and 100 Mpc/h boxes, but performed the RT calculation with

a mesh resolution of 278 kpc/h. When the RT is coarse-grained in this way, hydrodynamic effects are lost, and some corrections to the recombination rate due to small scale clumping must be made. This usually takes the form of a clumping factor correction evaluated either locally or globally using the higher resolution N-body data.

An interesting variant of the post-processing approach is the work of Trac, Cen & Loeb (2008) who carried out a hydrodynamic cosmological simulation of reionization in a 100 Mpc/h box with 1536^3 grid cells and particles, taking the emitting source population and subgrid clumping from a much higher resolution ($11,560^3$!) N-body simulation. This is an advance over previous work in that large scale baryonic flows are included self-consistently. However small scale radiation hydrodynamic effects, such as the retardation of I-fronts by minihalos (Shapiro et al., 2004) or the photoevaporation of gas from halos are not modeled.

In this paper we present a numerical method for simulating cosmological reionization in large cosmological volumes in which all relevant processes (dark matter dynamics, hydrodynamics, chemical ionization and recombination, radiation transport, local star formation and feedback) are computed self-consistently on the same high resolution computational grid. We refer to this as *direct numerical simulation*, in analogy with turbulence simulations which solve the Navier-Stokes equations directly. We admit the analogy is not perfect, because not all physical scales are numerically resolved and we must employ a subgrid model for star formation. Nonetheless we use the term to connote that we solve the full set of dynamical and transport equations on a common discrete basis set (cells, particles). Another descriptor for our approach is *resolution matched*, to distinguish our simulations from the fine/coarse dual resolution scheme used in previous large-scale simulations.

The key numerical requirement for performing simulations that *both* resolve the sources and sinks of ionizing radiation *and* correctly model the abundance and clustering of sources is *algorithmic scalability*. Parallel scalability is also important, but of secondary importance to algorithmic scalability. Algorithmic scalability refers to how the time to solution scales with the number of unknowns N. Direct

force evalulation gravitational N-body problems scale as N^2. While this is the most accurate approach, it is impractical for $N \sim 10^{10}$ which characterizes modern cosmological N-body simulations. Reionization simulations pose a similar scaling problem. If N is the number of fluid elements (particles, cells) and S is the number of ionizing sources, then the work scales as $N \times S$. At fixed resolution S scales as N, since both are proportional to the volume simulated. If ray tracing is the method used for radiative transfer, and R is the number of rays propagated per source, then the work scales as N^2R. The factor R is typically of order 100, but may be compensated for by the fact that $S/N \ll 1$. Therefore work scales as N^2 with the commonly used ray tracing approach, and this approach is not tenable for very large N. This is the underlying reason why previous large box simulations perform the radiative transfer calculation on a coarser grid than the dark matter calculation. For example, in the work of Trac & Cen (2007), the disparity in scales is 32.

What is desired is an algorithm that is ideally $\mathcal{O}(N)$, but lacking that, no worse that $\mathcal{O}(N \log N)$. Ray merging is one way to achieve this scaling with ray-based codes (e.g., Wise & Abel 2011). We have achieved $\mathcal{O}(N \log N)$ scaling by numerically representing the radiation field as a *grid field*, and employing optimally scalable geometric multigrid methods for the solution of the radiation field equation. In this work the radiation field is treated in the flux-limited diffusion (FLD) approximation, and discretized on the same grid as used for the dark matter and hydrodynamics. The method we describe below is currently implemented on uniform Cartesian grids within version 2 of the community code *Enzo* (Enz, 2010); an adaptive mesh version of this is under development and will be reported on in a forthcoming paper (Reynolds et al., *in prep*).

In Sec. 2 we describe the mathematical formulation of the problem. In Sec. 3 we present the numerical method of solution, focusing on the solution of the coupled radiation diffusion, chemical ionization, and gas energy equations within the *Enzo* code framework. As *Enzo* has been described elsewhere, only a brief summary of its methods are included. Section 4 contains results from verification tests (Sec. 4.1), validation tests (Sec. 4.2), parallel scaling tests (Sec. 4.3), and

execution speed tests (Sec. 4.4). We then illustrate the applicability of our method to cosmic reionization in Sec. 5, confining ourselves to a qualitative description of the results; a quantitative analysis of the results will be presented in a forthcoming paper (So et al., *in prep*). We present a summary and conclusions in Sec. 6.

2.2 Mathematical Formulation

We solve the coupled equations of multispecies gas dynamics, dark matter dynamics, self-gravity, primordial gas chemistry, radiative transfer, and gas cooling/heating in a comoving volume of the expanding universe. In this paper we assume the governing equations are discretized on a cubic uniform Cartesian mesh in comoving coordinates assuming periodic boundary conditions. In Reynolds et al. (in prep.) we generalize our method to adaptive meshes. The background spacetime is assumed to be a FRW model with ΛCDM cosmological parameters (Komatsu et al., 2011). In this work we consider only the 5 ionic states of H and He and e^-; i.e., the commonly used "6-species" model of primordial gas (Abel et al., 1997; Anninos et al., 1997). Molecular hydrogen chemistry is ignored as we are primarily concerned with the later stages of H reionization driven by star formation in atomic line cooling galaxies. Star formation is modeled phenomenologically through a subgrid model described in the next section. Newly formed stars are sources of UV radiation, and the radiation is transported in the grey flux-limited diffusion approximation. Star formation in spatially distributed galaxies thus sources an inhomogeneous and evolving ionizing radiation field, which is used to calculate the local ionization and thermal state of the gas. This in turn controls the local cooling rate of the gas, and by virtue of the subgrid star formation model, the local star formation rate. We thus have a closed system of equations that we can evolve forward in time subject to the choice of initial conditions. In all but the verification test problems, cosmological initial conditions are generated using standard methods.

The choice of flux-limited diffusion (FLD) is motivated by its simplicity and its ability to smoothly transition between optically thin and thick regimes.

Its properties as well as its limitations are well understood, and efficient numerical methods exist for parallel computation (e.g., Hayes et al. 2006). A second motivation is that we are interested in modeling reionization in large cosmological volumes and field-based solvers scale independently of the number of sources, unlike ray tracing methods. In the early stages of reionization, when HII regions are largely isolated, FLD provides accurate I-front speeds, as shown by our verification tests in Sec. 4.1. At late times, during and after overlap, the gas is bathed in a diffuse radiation field arising from numerous point sources for which the angular structure of the radiation field is unimportant. It is during the early percolation phase when several HII regions merge that FLD is inaccurate with regard to the angular distribution of the radiation field. This leads to some inaccuracies of the shapes of the I-fronts compared to a solution obtained using ray tracing (see Sec. 4.3). However we consider these shape differences of secondary importance since we are interested in globally averaged ionization properties. A well known limitation of FLD is that opaque blobs do not cast shadows if they are illuminated from one side (e.g., Hayes & Norman 2003). Instead, the radiation flows around the backside of the irradiated blob. By contrast, a ray tracing method will cast a sharp shadow (Iliev et al. 2009, Wise & Abel 2011). What matters for global reionization simulations however is how long the opaque blobs remain self-shielded; i.e., their photoevaporation times. We have compared the photoevaporation times for identically resolved blobs using FLD and the ray tracing method of Wise & Abel (2011), and find them comparable despite the inability of FLD to cast a shadow (sec Sec. 2.4.2).

We consider the coupled system of partial differential equations (Reynolds

et al., 2009),

$$\nabla^2\phi = \frac{4\pi g}{a}(\rho_b + \rho_{dm} - \langle\rho\rangle), \tag{2.1}$$

$$\partial_t\rho_b + \frac{1}{a}\mathbf{v}_b\cdot\nabla\rho_b = -\frac{1}{a}\rho_b\nabla\cdot\mathbf{v}_b - \dot{\rho}_{SF}, \tag{2.2}$$

$$\partial_t\mathbf{v}_b + \frac{1}{a}\left(\mathbf{v}_b\cdot\nabla\right)\mathbf{v}_b = -\frac{\dot{a}}{a}\mathbf{v}_b - \frac{1}{a\rho_b}\nabla p - \frac{1}{a}\nabla\phi, \tag{2.3}$$

$$\partial_t e + \frac{1}{a}\mathbf{v}_b\cdot\nabla e = -\frac{2\dot{a}}{a}e - \frac{1}{a\rho_b}\nabla\cdot(p\mathbf{v}_b) - \frac{1}{a}\mathbf{v}_b\cdot\nabla\phi + G - \Lambda + \dot{e}_{SF} \tag{2.4}$$

$$\partial_t \mathtt{n}_i + \frac{1}{a}\nabla\cdot(\mathtt{n}_i\mathbf{v}_b) = \alpha_{i,j}\mathtt{n}_e\mathtt{n}_j - \mathtt{n}_i\Gamma_i^{ph}, \qquad i = 1,\ldots,N_s \tag{2.5}$$

$$\partial_t E + \frac{1}{a}\nabla\cdot(E\mathbf{v}_b) = \nabla\cdot(D\nabla E) - \frac{\dot{a}}{a}E - c\kappa E + \eta. \tag{2.6}$$

The comoving form of Poisson's equation (2.1) is used to determine the modified gravitational potential, ϕ, where g is the gravitational constant, ρ_b is the comoving baryonic density, ρ_{dm} is the dark matter density, and $\langle\rho\rangle$ is the cosmic mean density. The collisionless dark matter density ρ_{dm} is evolved using the Particle-Mesh method, as described in Hockney & Eastwood (1988); Norman & Bryan (1999); O'Shea et al. (2004). The conservation equations (2.2)-(2.4) correspond to the compressible Euler equations in a comoving coordinate system Bryan et al. (1995). These relate the density to the proper peculiar baryonic velocity $\mathbf{v}_b \equiv a(t)\dot{\mathbf{x}}$, the proper pressure p, and the total gas energy per unit mass e. The equations (2.5) model ionizaton processes between the chemical species HI, HII, HeI, HeII, HeIII and the electron density. Here, $\mathtt{n}_i$ denotes the i^{th} comoving elemental species number density, $\mathtt{n}_e$ is the electron number density, $\mathtt{n}_j$ corresponds to ions that react with the species i, and $\alpha_{i,j}$ are the reaction rate coefficients defining these interactions (Abel et al., 1997; Hui & Gnedin, 1997). The equation (2.6) describes the flux-limited diffusion (FLD) approximation of radiation transport in a cosmological medium (Hayes & Norman, 2003; Paschos, 2005), where E is the comoving grey radiation energy density. Within this equation, the function D is the *flux limiter* that depends on face-centered values of E, ∇E and the opacity κ (Morel, 2000),

$$D = \min\left\{c\left(9\kappa^2 + R^2\right)^{-1/2}, D_{max}\right\}, \quad \text{and} \quad R = \max\left\{\frac{|\partial_x E|}{E}, R_{min}\right\}. \tag{2.7}$$

Here the spatial derivative within R is computed using non-dimensional units at the computational face adjoining two neighboring finite-volume cells, $D_{max} = 0.006\,c\,L_{unit}$ and $R_{min} = 10^{-20}/L_{unit}$ with L_{unit} the length non-dimensionalization factor for the simulation, and the face-centered radiation energy density and opacity are computed using the arithmetic and harmonic means, respectively,

$$E = \frac{E_1 + E_2}{2}, \qquad \kappa = \frac{2\kappa_1\kappa_2}{\kappa_1 + \kappa_2}.$$

Among the many available limiter formulations we have tested ((Hayes & Norman, 2003; Morel, 2000; Reynolds et al., 2009)), this version performs best at producing causal radiation propagation speeds in the low-opacity limit typical of the late stages of reionization simulations.

Cosmic expansion for a smooth homogeneous background is modeled by the function $a(t) \equiv (1+z)^{-1}$, where the redshift z is a function of time. $a(t)$ is obtained from a solution of the Friedmann equation for the adopted cosmological parameters. All comoving densities ρ_i relate to the proper densities through $\rho_i \equiv \rho_{i,\mathrm{proper}} a(t)^3$. All spatial derivatives are taken with respect to the comoving position $\mathbf{x} \equiv \mathbf{r}/a(t)$. We use a standard ideal gas equation of state to close the system,

$$e = \frac{p}{2\rho_b/3} + \frac{1}{2}|\mathbf{v}_b|^2. \tag{2.8}$$

2.2.1 Model Coupling

The equations (2.1)-(2.6) are coupled through a variety of physical processes. In defining our grey radiation energy density E, we allow specification of an assumed spectral energy distribution (SED), $\chi_E(\nu)$. Here, we write the frequency-dependent radiation density using the decomposition $E_\nu(\mathbf{x}, t, \nu) = \tilde{E}(\mathbf{x}, t)\,\chi_E(\nu)$. This relates to the grey radiation energy density E through the equation

$$E(\mathbf{x}, t) = \int_{\nu_1}^{\infty} E_\nu(\mathbf{x}, t, \nu)\,\mathrm{d}\nu = \tilde{E}(\mathbf{x}, t) \int_{\nu_1}^{\infty} \chi_E(\nu)\,\mathrm{d}\nu, \tag{2.9}$$

where $\tilde{E}$ is an intermediate quantity that is never computed. We note that this relationship is valid only if the indefinite integral of $\chi_E(\nu)$ exists, as is the case for quasar and stellar type spectra. Implemented in *Enzo* are a variety of user-selectable SEDs including black body, monochromatic, and powerlaw (some of

these are used for the verification tests; see Sec. 4.2). In our application to cosmic reionization, we utilize the SED for low metallicity Pop II stars from Ricotti et al. (2002).

With this in place, we define the radiation-dependent photoheating and photoionization rates (Osterbrock, 1989),

$$G = \frac{cE}{\rho_b} \sum_i^{N_s} \mathtt{n}_i \left[\int_{\nu_i}^{\infty} \sigma_i(\nu) \chi_E(\nu) \left(1 - \frac{\nu_i}{\nu}\right) \mathrm{d}\nu \right] \Big/ \left[\int_{\nu_1}^{\infty} \chi_E(\nu) \, \mathrm{d}\nu \right], \tag{2.10}$$

$$\Gamma_i^{ph} = \frac{cE}{h} \left[\int_{\nu_i}^{\infty} \frac{\sigma_i(\nu) \chi_E(\nu)}{\nu} \mathrm{d}\nu \right] \Big/ \left[\int_{\nu_1}^{\infty} \chi_E(\nu) \, \mathrm{d}\nu \right]. \tag{2.11}$$

Here, $\sigma_i(\nu)$ is the ionization cross section for the species $\mathtt{n}_i$, h is Planck's constant, and ν_i is the frequency ionization threshold for species $\mathtt{n}_i$ ($h\nu_{HI}$ = 13.6 eV, $h\nu_{HeI}$ = 24.6 eV, $h\nu_{HeII}$ = 54.4 eV).

In addition, gas cooling due to chemical processes occurs through the rate Λ that depends on both the chemical number densities and current gas temperature (Abel et al., 1997; Anninos et al., 1997),

$$T = \frac{2\, p\, \mu\, m_p}{3\, \rho_b\, k_b}, \tag{2.12}$$

where m_p corresponds to the mass of a proton, μ corresponds to the local molecular weight, and k_b is Boltzmann's constant. In addition, the reaction rates $\alpha_{i,j}$ are highly temperature dependent (Abel et al., 1997; Hui & Gnedin, 1997). The opacity κ depends on the local ionization states $\mathtt{n}_i$ and the assumed SED χ_E,

$$\kappa = \sum_{i=1}^{N_s} \mathtt{n}_i \left[\int_{\nu_i}^{\infty} \sigma_i(\nu) \chi_E(\nu) \, \mathrm{d}\nu \right] \Big/ \left[\int_{\nu_i}^{\infty} \chi_E(\nu) \, \mathrm{d}\nu \right]. \tag{2.13}$$

The emissivity η is based on a star-formation "recipe" described below.

2.3 Numerical Method

2.3.1 The Enzo Code

Our radiation hydrodynamical cosmology is built on top of the publicly available hydrodynamic cosmology code *Enzo* (Enz, 2010), whose numerical methods have been documented elsewhere (O'Shea et al., 2004; Norman et al., 2007).

Here we provide a brief summary. The basic *Enzo* code couples an N-body particle-mesh (PM) solver, which is used to follow the evolution of collisionless dark matter, with an Eulerian adaptive mesh refinement (AMR) method for ideal gas dynamics. Dark matter is assumed to behave as a collisionless phase fluid, obeying the Vlasov-Poisson equation. We use the second order-accurate Cloud-In-Cell (CIC) formulation, together with leapfrog time integration, which is formally second order-accurate in time. *Enzo* hydrodynamics utilizes the piecewise parabolic method (PPM) (Colella & Woodward, 1984) to evolve the mass density field for each chemical species of interest assuming a common velocity field (i.e., multispecies hydrodynamics.) PPM is formally second order-accurate in space and time. The gravitational potential is computed by solving the Poisson equation on the uniform Cartesian grid using 3D FFTs. When AMR is employed (which is not the case in this work), the subgrid gravitational potential is computed using a local multigrid solve of the Poisson equation with boundary conditions supplied from the parent grid.

The non-equilibrium chemical and cooling properties of primordial (metal-free) gas are determined using optional 6–, 9–, and 12–species models; in this work we restrict ourselves to the 6-species model involving H, H^+, He, He^+, He^{++}, and e^-. This reaction network results in a stiff set of rate equations which are solved with the first-order semi-implicit method described in Anninos et al. (1997), or a new second-order semi-analytic method described below. *Enzo* also calculates radiative heating and cooling following atomic line excitation, recombination, collisional excitation, free-free transitions, molecular line cooling, and Compton scattering of the cosmic microwave background as well as different models for a metagalactic ultraviolet background that heats the gas via photoionization and/or photodissociation.

To this we add our flux-limited diffusion radiation transport solver, which is solved using an optimally scalable geometric multigrid algorithm detailed here. When simulating inhomogeneous reionization, the metagalactic UV radiation field is solved for directly as a function of position and time, rather than input to the code as an externally-evaluated homogeneous background (e.g., Haardt & Madau

(2012)).

2.3.2 Star Formation and Feedback

Because star formation occurs on scales not resolved by our uniform mesh simulation, we rely on a subgrid model which we calibrate to observations of star formation in high redshift galaxies. The subgrid model is a variant of the Cen & Ostriker (1992) prescription with two important modifications as described in Smith et al. (2011). In the original Cen & Ostriker recipe, a computational cell forms a collisionless "star particle" if a number of criteria are met: the baryon density exceeds a certain numerical threshold; the gas velocity divergence is negative, indicating collapse; the local cooling time is less than the dynamical time; and the cell mass exceeds the Jeans mass. In our implementation, the last criterion is removed because it is always met in large scale, fixed-grid simulations, and the overdensity threshold is taken to be $\rho_b/(\rho_{c,0}(1+z)^3) > 100$, where $\rho_{c,0}$ is the critical density at z=0. If the three remaining criteria are met, then a star particle representing a large collection of stars is formed in that timestep and grid cell with a total mass

$$m_* = f_* m_{cell} \frac{\Delta t}{t_{dyn}}, \tag{2.14}$$

where f_* is an efficiency parameter we adjust to match observations of the cosmic star formation rate density (SFRD) (Bouwens et al., 2011a), m_{cell} is the cell baryon mass, t_{dyn} is the dynamical time of the combined baryon and dark matter fluid, and Δt is the hydrodynamical timestep. An equivalent amount of mass is removed from the grid cell to maintain mass conservation.

Although the star particle is formed instantaneously (i.e., within a single timestep), the conversion of removed gas into stars is assumed to proceed over a longer timescale, namely t_{dyn}, which more accurately reflects the gradual process of star formation. In time Δt, the amount of mass from a star particle converted into newly formed stars is given by

$$\Delta m_{SF} = m_* \frac{\Delta t}{t_{dyn}} \frac{t - t_*}{t_{dyn}} e^{-(t-t_*)/t_{dyn}}, \tag{2.15}$$

where t is the current time and t_* is the formation time of the star particle. To make the connection with Eq. (2.4), we have $\dot{\rho}_{SF} = \Delta m_{SF}/(V_{cell}\Delta t)$, where V_{cell} is the volume of the grid cell.

Stellar feedback consists of the injection of thermal energy, gas, metals, and radiation to the grid, all in proportion to Δm_{SF}. The thermal energy Δe_{SF}, gas mass Δm_g, and metals Δm_Z returned to the grid are given by

$$\Delta e_{SF} = \Delta m_{SF} c^2 \epsilon_{SN}, \qquad \Delta m_g = \Delta m_{SF} f_{m*}, \qquad \Delta m_Z = \Delta m_{SF} f_{Z*}, \tag{2.16}$$

where c is the speed of light, ϵ_{SN} is the supernova energy efficiency parameter, and $f_{m*} = 0.25, f_{Z*} = 0.02$ is the fraction of the stellar mass returned to the grid as gas and metals, respectively. Rather than add the energy, gas, and metals to the cell containing the star particle, as was done in the original Cen & Ostriker (1992) paper, we distribute it evenly among the cell and its 26 nearest neighbors to prevent overcooling. As shown by Smith et al. (2011), this results in a star formation recipe which can be tuned to reproduce the observed SFRD. This is critical for us, as we use the observed high redshift SFRD to calibrate our reionization simulations.

To calculate the radiation feedback, we define an emissivity field $\eta(x)$ on the grid which accumulates the instantaneous emissivities $\eta_i(t)$ of all the star particles within each cell. To calculate the contribution of each star particle i at time t we assume an equation of the same form for supernova energy feedback, but with a different energy conversion efficiency factor ϵ_{UV}. Therefore

$$\eta = \sum_{\mathrm{i}} \epsilon_{\mathrm{uv}} \frac{\Delta m_{\mathrm{SF,i}} c^2}{V_{\mathrm{cell}} \Delta t} \tag{2.17}$$

Emissivity η is in units of erg/s/cm^3. The UV efficiency factor ϵ_{uv} is taken from Ricotti et al. (2002) as $4\pi \times 1.1 \times 10^{-5}$, where the factor 4π comes from the conversion from mean intensity to radiation energy density.

2.3.3 Operator Split Solution Procedure

We implement the model (3.2)-(3.7) in the open-source community cosmology code, *Enzo* (Enz, 2010). This simulation framework utilizes a method-of-lines approach, in which space and time are discretized separately. To this end, we use a finite-volume spatial discretization of the modeling equations. For this study, all of our simulations were run in *unigrid* mode, so that the cosmological volume is discretized using a regular grid. Although *Enzo* was built to enable block-structured adaptive mesh refinement (AMR) using a standard Berger-Colella formalism (Berger & Colella, 1989), that mode does not currently allow as extreme parallel scalability as the unigrid version. Due to our desire to simulate very large cosmological volumes for understanding reionization processes, this scalability was paramount.

We discretize in time using an operator split time-stepping approach, wherein separate components are treated with solvers that have been tuned for their specific physics. To this end, we break apart the equations into four distinct components. The first component corresponds to the self-gravity equation (3.2),

$$\nabla^2\phi = \frac{4\pi g}{a}(\rho_b + \rho_{dm} - \langle\rho\rangle), \tag{2.18}$$

that solves for the instantaneous gravitational potential ϕ, which contributes to sources in the momentum and energy conservation equations. We perform this solve using our own 3D Fast Fourier Transform solver built on the publicly available FFTE library. These solves take as sources the gridded baryon density and dark matter density fields ρ_b and ρ_{dm}. The former is defined as a grid based Eulerian field. The latter is computed from the dark matter particle positions $\mathbf{x}_i^n$ using the CIC mass assignment algorithm (Hockney & Eastwood, 1988).

The second component in our splitting approach corresponds to the cosmological Euler equations, along with passive advection of other comoving density

fields,

$$\begin{aligned}
\partial_t \rho_b + \frac{1}{a}\mathbf{v}_b \cdot \nabla \rho_b &= -\frac{1}{a}\rho_b \nabla \cdot \mathbf{v}_b, \\
\partial_t \mathbf{v}_b + \frac{1}{a}\left(\mathbf{v}_b \cdot \nabla\right)\mathbf{v}_b &= -\frac{\dot{a}}{a}\mathbf{v}_b - \frac{1}{a\rho_b}\nabla p - \frac{1}{a}\nabla\phi, \\
\partial_t e + \frac{1}{a}\mathbf{v}_b \cdot \nabla e &= -\frac{2\dot{a}}{a}e - \frac{1}{a\rho_b}\nabla\cdot(p\mathbf{v}_b) - \frac{1}{a}\mathbf{v}_b\cdot\nabla\phi, \\
\partial_t E + \frac{1}{a}\nabla\cdot(E\mathbf{v}_b) &= 0, \\
\partial_t \mathtt{n}_i + \frac{1}{a}\nabla\cdot(\mathtt{n}_i\mathbf{v}_b) &= 0, \qquad i = 1,\ldots,N_s.
\end{aligned} \tag{2.19}$$

We point out that the above energy equation does not include photo-heating, chemical cooling, or supernova feedback processes, which are included in subsequent components. These equations are solved explicitly using the *Piecewise Parabolic Method* (Colella & Woodward, 1984), to properly track hydrodynamic shocks, while obtaining second-order accuracy away from shock discontinuities.

The third solver component corresponds to the grey radiation energy equation (3.7),

$$\partial_t E = \nabla\cdot(D\nabla E) - \frac{\dot{a}}{a}E - c\kappa E + \eta. \tag{2.20}$$

Our solver for this component is based on the algorithm described in Reynolds et al. (2009); Reynolds (2010). Specifically, since the time scale for radiation transport is much faster than for hydrodynamic motion, we use an implicit θ-method for time discretization, allowing both backwards Euler and trapezoidal implicit quadrature formulas. Moreover, we evaluate the limiter D using the previous-time solution, E^n when calculating the time-evolved solution, E^{n+1}. Under these approximations, our implicit FLD approximation for the radiative transport results in a linear system of equations over the computational domain, as opposed to a nonlinear system of equations, as used in our previous work (Norman et al., 2007; Reynolds et al., 2009; Norman et al., 2009). This linear system is posed in residual-correction form, in which we solve for the change in the radiation field, $\delta E = E^{n+1} - E^n$, over the course of a time step. To solve this linear system, we employ a multigrid-preconditioned conjugate gradient solver from the *hypre* library (hyp, 2011), that allows optimal $\mathcal{O}(n \log n)$ parallel scalability to the extents of modern supercom-

Table 2.1: Parameters used in the *hypre* linear solver

Parameter	Value
Outer Solver	PCG
CG iterations	50
CG tolerance	10^{-8}
Inner Preconditioner	PFMG
MG iterations	12
MG relaxation type	nonsymmetric Red/Black Gauss-Seidel
MG pre-relaxation sweeps	1
MG post-relaxation sweeps	1

puter architectures. Specific parameters used in this solve are found in Table 2.1.

The fourth physical component within our operator-split formulation corresponds to photoionization, photoheating, chemical ionization and gas cooling processes,

$$\begin{aligned} \partial_t e &= G - \Lambda, \\ \partial_t \mathtt{n}_i &= \alpha_{i,j} \mathtt{n}_e \mathtt{n}_j - \mathtt{n}_i \Gamma_i^{ph}, \qquad i = 1, \ldots, N_s. \end{aligned} \tag{2.21}$$

Since these processes occur on time scales commensurate with the radiation transport, and much faster than hydrodynamic motion, they are also solved implicitly in time, using adaptive-step, time-subcycled solves of these spatially-local processes. We have two different algorithms for solving these equations. The first, more loosely coupled, solver uses a single Jacobi iteration of a linearly-implicit backwards Euler discretization for each species in each cell. Although this solver does not attempt to accurately resolve the nonlinearity in these equations, nor does it iterate between the different species in each cell to achieve a fully self-consistent solution, its adaptive time stepping strategy enables this single iteration to achieve results that are typically accurate to within 10% relative error, and results in highly efficient calculations.

Our second solver for the system (2.21) approximates the equations using an implicit quasi-steady-state formulation, in which the source terms for the energy equation assume a fixed ionization state $(\mathtt{n}_i^{n-1} + \mathtt{n}_i^n)/2$, and the chemistry equations

assume a fixed energy $(e^{n-1}+e^n)/2$ when evolving the time step $t^{n-1} \rightarrow t^n$. Under this quasi-steady-state approximation, we solve the resulting set of differential equations analytically, to obtain the new values e^n and $\mathtt{n}_i^n$. However, since these updated solutions implicitly contribute to the source terms for one another, we wrap these analytical solvers within a nonlinear Gauss-Seidel iteration to achieve full nonlinear convergence. As a result of this much tighter coupling between the gas energy and chemical ionization, this solver is more expensive per time step, but may result in a more accurate and stable solution than the more loosely-split algorithm.

The fifth solver component computes star formation and feedback processes, and evaluates the emissivity field for use in the next step. It corresponds to integrating the equations

$$\partial_t \rho_b = -\dot{\rho}_{SF}, \tag{2.22}$$

$$\partial_t e = \dot{e}_{SF} \tag{2.23}$$

and evaluating Eq. (2.4) using the procedures described in Sec. 2.3.2.

These distinct components are coupled together through the potential ϕ (gravity $\rightarrow$ hydrodynamics+DM dynamics), opacity κ (chemistry $\rightarrow$ radiation), emissivity η (star formation $\rightarrow$ radiation), photoheating G (radiation $\rightarrow$ energy), cooling Λ (chemistry $\rightarrow$ energy), temperature T (energy $\rightarrow$ chemistry), and photoionization Γ_i^{ph} (radiation $\rightarrow$ chemistry). Each of these couplings is handled using one of two mechanisms, direct manipulation of the solution components (Λ, κ, T), or filling new fields over the domain containing each term that are passed between modules $(\nabla\phi, \eta, G, \Gamma_i^{ph})$.

2.3.4 Radiation Subcycling

Since both the radiation (2.20) and chemistry/energy (2.21) subsystems evolve at similar time scales that are typically much faster than the hydrodynamic time scale, consistency between these processes is maintained through an adaptive time-stepping strategy, wherein the radiation system limits the overall time step selection strategy, using a conservative time step to ensure consistency between the

physical processes. This additionally ensures that each radiation solve only requires relatively minor corrections as time evolves, resulting in a highly efficient CG/MG iteration. The time step estimation algorithm is the same as in Reynolds et al. (2009), but in the current work we use the time step tolerance $\tau_{tol} = 10^{-4}$, which ensures a relative change-per-step in the radiation field of 0.01%, when measured in a vector RMS norm.

For increased robustness, we have enabled subcycling within the radiation solver. While this technically allows the radiation solver to subcycle faster than the coupled processes, we only employ this functionality in time steps where the CG/MG solver fails. This situation typically only occurs in the initial step after the first stars are created. Prior to star formation the dynamical time scale due to hydrodynamics and gravity is much longer than the time scales of radiation transport and chemical ionization after star formation. Since we adapt our time step estimates using the behavior in previous steps, our estimation strategy does not predict the abrupt change in physics when the first stars are created, so the step size estimate from the previous step is too large, causing the CG/MG solver to diverge. Once this occurs, the radiation subsystem solver decreases its time step size and then subcycles to catch up with the overall time step of the remaining physics.

When using the loosely-coupled ionization/heating solver, the sequence of these processes within a time step $t^{n-1} \rightarrow t^n$ are as follows:

Set $t_{hydro} = t_{chem} = t_{rad} = t_{dm} = t^{n-1}$.
Set $\Delta t = \min\{\Delta t_{hydro}, \Delta t_{expansion}, \Delta t_{rad}\}$, and $t^n = t^{n-1} + \Delta t$.
While ($t_{rad} < t^n$)

    Try to evolve the $E(t)$ according to (2.20).
    If failure, set $\Delta t_{rad} = 0.1\Delta t_{rad}$.
    Else set $t_{rad} = t_{rad} + \Delta t_{rad}$ and update Δt_{rad} based on
    accuracy estimates.

Post-process $E(t^n)$ to compute G and Γ_i^{ph}.
Compute ϕ using (2.18), and post-process to generate $\nabla\phi$.
Evolve the hydrodynamics sub-system (2.19), $t_{hydro} \rightarrow t_{hydro}+\Delta t$.
While ($t_{chem} < t^n$)

```
        Set Δt_chem based on accuracy estimates.
        Evolve the chemical and gas energy subsystem (2.21),
        t_chem → t_chem + Δt_chem.

    Evolve the dark matter particles, t_dm → t_dm + Δt.
    Compute η using equation (3.15).
```

When using the tightly-coupled ionization/heating solver, this sequence of processes differs slightly:

```
    Set t_hydro = t_chem = t_rad = t_dm = t^{n-1}.
    Set Δt = min{Δt_hydro, Δt_expansion, Δt_rad}.
    While (t_rad < t^n)

        Try to evolve the radiation field according to (2.20).
        If failure, set Δt_rad = 0.1 * Δt_rad.
        Else

            Set t_rad = t_rad + Δt_rad and update Δt_rad based
            on accuracy estimates.
            Post-process E(t_rad) to compute G and Γ_i^ph.
            While (t_chem < t_rad)

                Set Δt_chem based on accuracy estimates.
                Evolve the chemical/energy subsystem (2.21),
                t_chem → t_chem + Δt_chem.

    Compute φ using (2.18), and post-process to generate ∇φ.
    Evolve the hydrodynamics sub-system (2.19), t_hydro → t_hydro+Δt.
    Evolve the dark matter particles, t_dm → t_dm + Δt.
    Compute η using equation (3.15).
```

2.4 Tests

2.4.1 Verification Tests

The radiation, hydrodynamics and chemistry solvers in *Enzo* have been verified in previous work (Reynolds et al., 2009), so we will not focus on the performance of each individual solver here. However, what is new in this work is our updated coupling strategy between the radiation transport and chemistry, that unlike the fully coupled implicit solver in Norman et al. (2007); Reynolds et al.

(2009); Norman et al. (2009), now splits these solvers apart, with coupling instead based on our adaptive time-stepping strategy.

To this end, we focus our verification tests in this paper on two tests with analytical solutions that exercise only the radiation transport and chemical ionization/recombination components of *Enzo*. These tests were previously described in Reynolds et al. (2009) (sections 4.5 and 4.6); we summarize them again here.

Isothermal ionization of a static neutral hydrogen region

This verification test problem, matching test 1 in Iliev et al. (2006), focuses on the expansion of an ionized hydrogen (HII) region in a uniform gas surrounding a radiation source. The problem is simplified through assumption of a static gas field, and a fixed temperature. Under these assumptions, the emitted radiation should rapidly ionize the nearby hydrogen, and then this ionized region should propagate spherically outward until it reaches a terminal radius at which ionizations balance with recombinations, called the Strömgren radius. The radius of this ionization front, $r(t)$, may be analytically computed as

$$r(t) = r_s \left(1 - e^{-t/t_{rec}}\right)^{1/3}, \quad \text{where} \quad r_s = \left(\frac{3\,\dot{N}_\gamma}{4\pi\,\alpha_B\,n_H^2}\right)^{1/3}. \tag{2.24}$$

Here, r_s is the Strömgren radius, $t_{rec} = (\alpha_B\,n_H)^{-1}$ is the recombination time, $\dot{N}_\gamma$ is the photon emission rate, n_H is the hydrogen number density of the gas, and α_B is the case B hydrogen recombination rate.

In our tests, we use parameters $\dot{N}_\gamma = 5\times10^{48}$ photons s^{-1}, $n_H = 10^{-3}$ cm^{-3}, $\alpha_B = 2.59\times10^{-12}$ cm^{2}s^{-1}, domain $[0, 6.6\,\mathrm{kpc}]^3$, temperature $T = 10^4$ K, and time interval $[0, 5\,\mathrm{Myr}]$. The ionization source is assumed to be monochromatic, at the HI ionization frequency $h\nu = 13.6$ eV, and is located at the location $(0, 0, 0)$. For initial conditions, we use $E = 10^{-45}$ erg cm^{-3} and ionization fraction HII/H = 0.0012. We employ reflecting boundary conditions for the radiation field at the $x = 0$, $y = 0$, and $z = 0$ faces, and outflow boundary conditions at the other three faces.

We plot spherically-averaged radial profiles of the radiation energy density and the ionization fractions at 10 Myr, 100 Myr and 500 Myr from a simulation

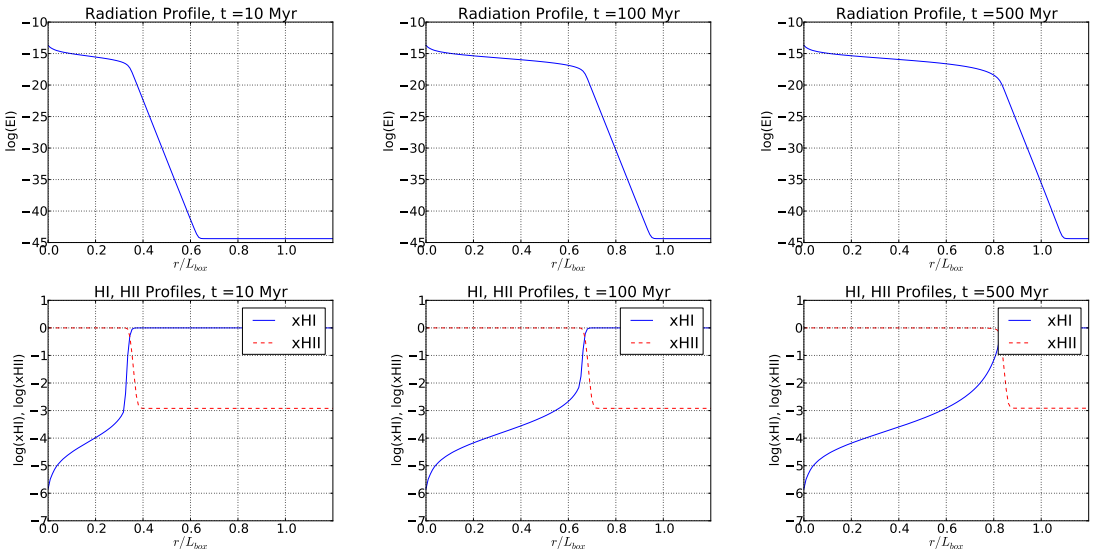

Figure 2.1: Spherically-averaged radial profiles of radiation energy density and ionization fractions for the isothermal ionization test in section 2.4.1 using a 128^3 mesh and time step tolerance $\tau_{tol} = 10^{-4}$. Plots are shown at 10, 100 and 500 Myr (left to right), with the radiation energy density on the top row and ionization fractions on the bottom row.

using a 128^3 spatial grid and time step tolerance $\tau_{tol} = 10^{-4}$ in Figure 2.1, showing the expected propagation of the radiation front and resulting I-front in time. Plots of the computed and analytical I front position and resulting error for this run are provided in Figure 2.2. To further investigate the accuracy of our new splitting approach between the radiation and chemistry solvers, we then performed these same tests at a variety of mesh sizes and time step tolerances τ_{tol}. For mesh sizes of 16^3, 32^3 and 64^3, and for tolerances 10^{-2}, 10^{-3}, 10^{-4} and 10^{-5}, we compute the error in the I front position as

$$error \;=\; \left\| \frac{r_{computed} - r_{true}}{r_s} \right\|_{RMS} \;=\; \left(\frac{1}{N_t} \sum_{i=1}^{N_t} \left(\frac{r_{computed,i} - r_{true,i}}{r_s} \right)^2 \right)^{1/2} . \quad (2.25)$$

In Figure 2.3, we plot the solution error as a function of the average time step size, as well as the total runtime as a function of the average time step size. As can be seen in these plots, as the tolerance decreases, the temporal solution accuracy increases linearly until we reach a maximum accuracy (minimum error) that results

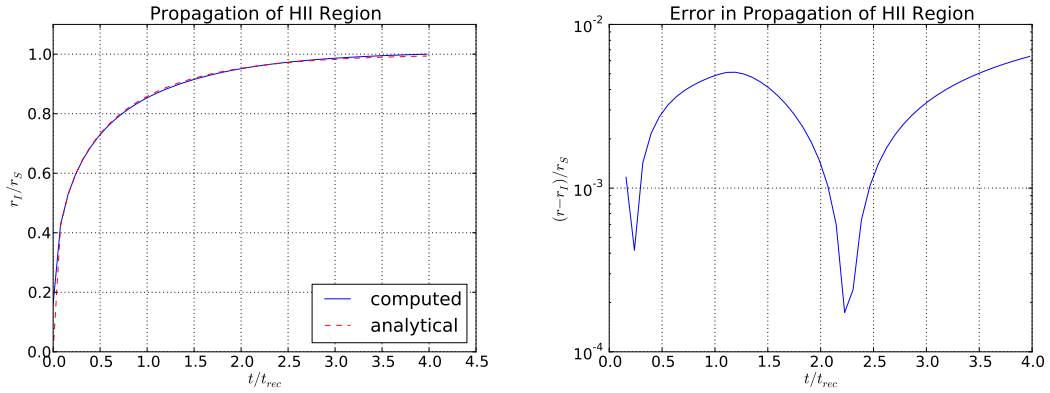

Figure 2.2: Comparison between computed and analytical I front position for the isothermal ionization test in section 2.4.1 using a 128^3 mesh and time step tolerance $\tau_{tol} = 10^{-4}$. Solution on left, error on right.

from other components in Enzo (spatial discretization accuracy, accuracy within Enzo's chemistry solver, etc.). Moreover, it is evident that as we decrease the time step tolerances, the required runtime increases linearly. These results imply that there is a "sweet spot" in our approach, wherein a tolerance of $\tau_{tol} = 10^{-4}$ achieves the solution with optimal accuracy before we begin to waste additional effort without achieving accuracy improvements. While this specific value is likely problem-dependent, we use it as a starting point in subsequent simulations.

Finally, in Figure 2.4 we plot a slice of the computed HII region through the center of the domain, perpendicular to the z-direction (other directions are equivalent), to show the convergence of the ionized region to a sphere at varying spatial resolutions.

Cosmological radiative ionization

This verification test is a slight variation of the previous problem, adding only the additional complication of a cosmologically expanding universe. Due to the cosmological expansion, the Strömgren radius itself increases due to the expansion of space, that reduces the hydrogen number density n_H as time proceeds,

$$r_s(t) = \left(\frac{3\,\dot{N}_\gamma}{4\pi\,\alpha_B\,n_H(t)^2} \right)^{1/3}. \tag{2.26}$$

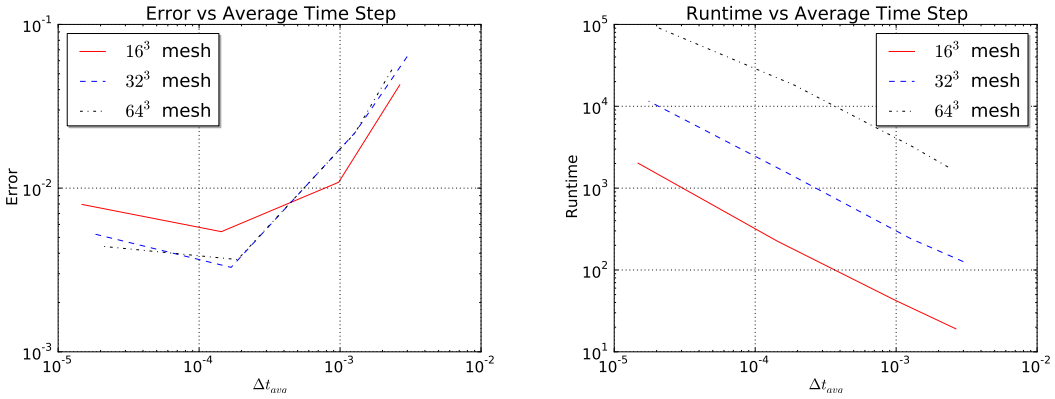

Figure 2.3: We ran tests using mesh sizes of 16^3, 32^3 and 64^4, and time step tolerances of 10^{-2}, 10^{-3}, 10^{-4} and 10^{-5}, and plot the I front position error (2.25) as a function of the average time step size. As expected, the runtime scales linearly with the inverse Δt_{avg}, and the error scales linearly with Δt_{avg}, at least until other sources of error dominate the calculation.

This causes the I front to initially approach r_s, but eventually fall behind as the expansion drives r_s outward. The analytical solution to this problem is given by Shapiro & Giroux (1987),

$$r(t) = r_{s,0}\left(\lambda e^{-\tau(a(t))}\int_1^{a(t)} e^{\tau(\tilde{a})}\left(1 - 2q_0 + \frac{2q_0}{\tilde{a}}(1-z_0)\right)^{-1/2} \mathrm{d}\tilde{a}\right)^{1/3}, \tag{2.27}$$

where

$$\tau(a) = \lambda\left(F(a) - F(1)\right)\left(6q_0^2(1+z_0)^2\right)^{-1}, \tag{2.28}$$

$$F(a) = \left(2 - 4q_0 - \frac{2q_0}{a}(1+z_0)\right)\left(1 - 2q_0 + \frac{2q_0}{a}(1+z_0)\right)^{1/2}. \tag{2.29}$$

Here, the parameter $\lambda = \alpha_B n_{H,0}/H_0/(1+z_0)$, with $r_{s,0}$, z_0 and $n_{H,0}$ as the Strömgren radius, redshift and hydrogen number density at the beginning of the simulation. Additionally, q_0 is the cosmological deceleration parameter, H_0 is the Hubble constant, and $a(t) = (1+z(t))^{-1}$ is the cosmological expansion parameter.

We run this problem using the parameters $q_0 = 0.5$, domain $[0, 80\,\mathrm{kpc}]^3$ (comoving), time/redshift domain $z = [4, 0]$, $H_0 = 0.5$, energy density contributions $\Omega_m = 1$, $\Omega_A = 0$ and $\Omega_b = 0.2$. Our initial conditions are $\rho = 1.175 \times 10^{-28}$ g

cm^{-3}, $T = 10^4$ K and $E = 10^{-45}$ erg cm^{-3}.

We again plot spherically-averaged radial profiles of the radiation energy density and the ionization fractions at redshifts 3.547, 2.423 and 1.692 from a simulation using a 128^3 spatial grid and time step tolerance $\tau_{tol} = 10^{-4}$ in Figure 2.5, showing the expected propagation and eventual stalling of the radiation front and resulting I-front in time. As with the previous test, we investigated the accuracy of our new splitting approach between the radiation and chemistry solvers using the same set of mesh sizes and time step tolerances as the test earlier in this section (2.4.1). Figure 2.6 contains the corresponding plots of the solution error and total runtime as a function of the average time step size. Our results are similar to those from the previous test, indicating that the modified time evolution approach employed in this work successfully achieves accurate solutions of our coupled radiation and ionization system.

2.4.2 Validation Tests

Validation tests are tests without analytic solutions that nonetheless serve as a useful point of comparison between codes implementing different physical models and numerical methods. In this section we test our algorithm against three validation tests that are most relevant to the problem of cosmological reionization. To our knowledge these are the first FLD results published to date, since the other codes running these problems have focused on ray-tracing, Monte Carlo, and variable tensor Eddington approximations of the radiative transfer equations.

Test 4 – Multiple sources in a cosmological density field

As our first validation test we run Test 4 introduced by Iliev et al. (2006) (hereafter RT06) and performed by Wise & Abel (2011) (hereafter WA11) using Enzo's ray tracing radiative transfer algorithm *Moray*. This is a static density field hydrogen ionization test where the cosmological density field is taken from a $z = 9$ snapshot from a simulation defined in a comoving box of size 0.5 h^{-1} Mpc on a mesh of 128^3 cells. There are 16 point sources centered in the 16 most massive halos whose locations and masses are provided as a part of the test. The sources

are assumed to turn on simultaneously at $z = 9$ and radiate for $t_s = 3$ Myr with an SED of a $T = 10^5$ K blackbody. The ionizing photon production rate of each source is taken to be

$$\dot{N}_\gamma = f_\gamma \frac{M\Omega_b}{\Omega_m m_H t_s}, \tag{2.30}$$

where $f_\gamma = 250$, M is the halo mass, $\Omega_m = 0.27$ and $\Omega_b = 0.043$. The simulation is evolved for 0.4 Myr, using a time step tolerance of $\tau_{tol} = 10^{-5}$.

In Fig. 2.7 we display slices of hydrogen neutral fraction and temperature through the center of the cube at two times: t=50 and 200 kyr. Comparing the images of neutral fraction with those of WA11, we see the I-fronts are smoother and rounder than what is obtained with ray tracing, but of comparable size and location. The notches in the I-front surface corresponding to the location of denser gas in filaments are visible but they are less sharply defined compared to the *Moray* results. Larger differences can be seen in the temperature slice, but these are attributable to the difference in spectral models used in the two methods. Our grey FLD model does not account for the penetration of more energetic photons ahead of the I-front as does the 4 frequency group model of WA11, and several of the codes in RT06. As discussed in RT06 and WA11, and documented in Test 5 of Iliev et al. (2009) (hereafter RT09) the high effective temperature of the radiating sources broadens the I-front in the multifrequency treatment, and preheats the gas ahead of the I-front, giving the appearance of a larger ionized region in the temperature slice. By contrast, methods with a simplified spectral model (grey or monochromatic) produce steep I-fronts with no preheating (see e.g., the results of the FTTE code in RT06, or the results of Test 5 in RT09).

In the left half of Fig. 2.8 we show pdf's of the neutral fraction and gas temperature at the two times corresponding to the slice images. The neutral fraction pdfs are in good agreement with results presented in RT06 and WA11. The temperature pdfs are qualitatively different from the results of multifrequency calculations for the reasons discussed above. Our pdfs show a bimodal temperature distribution, which correspond to the hot gas in the interior of the ionized region, and the cold neutral gas. The two peaks in the pdfs are filled in by a small amount of intermediate temperature gas in the I-front transition zone. Preheating of the

cold gas in a multifrequency treatment removes the low temperature spike, and adds more gas to the intermediate temperatures, producing a shoulder distribution function below 10^4 K.

In the right half of Fig. 2.8 we show the evolution of the volume- and mass-weighted ionized fraction in the volume. The volume-weighted fraction curve is in good agreement with the ray tracing results in WA11, with $x_v \approx 0.65$ at $t = 400$ kyr. The mass-weighted curve is at all times somewhat higher than the volume-weighted curve, in agreement with the results presented in RT06. WA11 observe a cross-over of the x_v and x_m curves, something we do not find. This discrepancy may be the result of the different spectral models, or the detailed I-front shapes. Another possibility is that some gas remains self-shielded in the interior of the ionized region at later times in the ray tracing calculation, which is engulfed and ionized in the FLD calculation. This bears further study, preferably with the effects of difference in spectral models removed.

Test 7 – Photoevaporation of a dense clump

As our second validation test we run Test 7 of RT09, also studied by WA11 using *Enzo+Moray*. This is a radiation hydrodynamic test involving ionizing radiation impinging on a dense, opaque spherical cloud which is subsequently photoevaporated. RT09 set this up as a plane wave of ionizing radiation sweeping over the cloud. To facilitate comparison with the WA11 results, we set it up as a spherical wave of ionizing radiation from a point source sweeping over the cloud. If run without hydrodynamics, the I-front is trapped in the dense cloud, and the cloud casts a sharp shadow (ignoring recombination radiation which would partially fill in the shadow zone.) With hydrodynamics engaged, the side of the cloud facing the source photoheats and expands, permitting a deeper penetration of radiation into the cloud. Eventually, the entire cloud is photoevaporated. It is important to check what FLD will do in this circumstance, in particular whether the lack of a shadow has much effect on the photoevaporation time for the cloud. As we will now show, the effect is weak, validating our use of FLD for large scale reionization problems.

The setup is as follows. A cubic domain 6.6 kpc on a side is employed, filled with an ambient medium of $n_H = 2 \times 10^{-4}$ cm^{-3} and T=8000 K. The cloud is in pressure equilibrium with the intercloud medium with density $n_H = 0.04$ cm^{-3} and T=40 K. The cloud is a top-hat sphere with radius $r_c = 0.8$ kpc, and is centered at (x,y,z) = (5, 3.3, 3.3) kpc. The ionized fraction is initially zero everywhere. A single radiation source is located in the center of the $x = 0$ boundary. It has a luminosity of $\dot{N}_\gamma = 3 \times 10^{51}$ photon/s. WA11 use the same four energy group spectral model to represent a 10^5 K blackbody as in Test 4 above. We use our grey FLD approximation which does not model spectral hardening, as discussed above. We thus do not expect our results to be identical with WA11.

Fig. 2.9 shows slices through the cloud midplane of neutral fraction, pressure, temperature, and density at time $t = 10$ Myr. At this time the I-front has propagated roughly 80% through the cloud on the axis, compared to about 50% in WA11. Because in the FLD approximation radiation propagates in the direction of the radiation energy density gradient, it has filled in the “nightside" of the cloud, ionizing the cloud from all sides. By 10 Myr only a small neutral patch remains. Comparing with Fig. 27 of WA11, we find similar structures on the “dayside" of the cloud, but the complete absense of a neutral shadow on the nightside.

Fig. 2.10 shows the same information for the cloud at $t = 50$ Myr. By this time the cloud has expanded considerably and become completely ionized, exhibiting a roughly spherical shape. The results of WA11 are similar, except for a small wedge-shaped neutral patch on the back of the cloud, which casts a small shadow into the diffuse intercloud medium. In reality, ionizing recombination radiation from the denser cloud gas would fill in this shadow and ionize the diffuse gas there, making it more like the FLD solution.

To enable a more quantitative comparison with WA11, we plot in Fig. 2.11 line cuts from the point source through the center of the cloud at $t = 1, 10, 50$ Myr. Because the FLD method ionizes the cloud from all sides with only a small delay between dayside and nightside irradiation, we see a less pronounced dayside-nightside asymmetry in the density and neutral fraction profiles compared with WA11 at 10 and 50 Myr. Both methods show good agreement on the position

and structure of the dense shell swept up by the expanding cloud at 50 Myr at $x/L_{box} \sim 0.4$. Significant differences are seen at 50 Myr for $x/L_{box} > 0.75$ (the cloud's center) due to shadowing effects in the *Moray* result which is absent in the FLD result.

Overall, the FLD calculation ionizes the cloud somewhat faster than predicted by WA11. However by 50 Myr both calculations produce a cloud which is either fully ionized or nearly so, and there is good agreement on the size of the cloud. The most significant difference is that the ray-tracing calculation predicts a small, neutral wedge-shaped patch on the nightside of the cloud which is absent in the FLD calculation. It is unlikely that this difference will be important in large scale reionzation simulations since clouds will be irradiated from multiple directions during the overlap phase.

Consolidated HII region with two sources

As our last validation test we demonstrate the performance of our FLD radiative transfer method on a consolidated HII region with two nearby point sources of equal luminosity. This problem was introduced by Petkova & Springel (2009) (hereafter PS09) and included in the extensive suite of tests carried out by WA11. This is a validation problem because it has no analytic solution (that we know of.) PS09 studied it because their method uses the variable tensor Eddington factor moment method (Stone et al., 1992; Norman et al., 1998; Hayes & Norman, 2003) where the Eddington tensor is computed assuming the medium is optically thin everywhere (Gnedin & Abel, 2001). As discussed in Gnedin & Abel (2001) it is known that the shapes of consolidated HII regions are slightly inaccurate due to the optically thin assumption, in the sense that the HII region is more elongated in the axial direction, and less expanded in the transverse direction than in reality. The solution presented by PS09 shows this elongation. The solution presented in WA11, which shows rounder but still slightly elongated I-fronts, should be a closer approximation to truth since it is calculated using adaptive ray tracing which in principle gets the geometric effects correct. However the omission of diffuse ionizing recombination radiation which becomes dominant near a stalled I-front

means that even the WA11 solution is an approximation to the true shape. It is thus interesting to see what FLD produces for this problem.

The setup is as follows. Two sources with luminosities of 5×10^{48} photons/s are separated by 8 kpc. The ambient medium is static with uniform density 10^{-3} cm^{-3} and T = 10^4 K. The computational domain is 20 kpc in width and 10 kpc in height and depth, and resolved with mesh of $128 \times 64 \times 64$ cells. The problem is evolved for 500 Myr, which is long enough for the consolidated HII region to evolve to a steady state.

Fig. 2.12 shows slices of neutral fraction on $x - y$ and $x - z$ planes through the axis connecting the sources. The consolidated HII region is similar in size to the solution presented by WA11, but noticeably rounder near its extremities. We do not include diffuse ionizing recombination radiation in our formalism, and thus this must be a consequence of FLD. Since we are solving the same problem, we expect the WA11 solution is closer to the truth, but note that the FLD solution is an acceptable approximation to truth given our intended application to large scale reionization.

2.4.3 Parallel Scalability

Excellent scalability of our radiation diffusion solver is fundamentally important to being able to simulate reionization in large cosmological volumes. Once the mass and spatial resolution requirements are established to adequately model the smallest galaxies in the source population, the problem becomes one of "weak scaling"; i.e., increasing the simulated volume at fixed resolution, rather than increasing the resolution in a fixed volume. To test the scaling of our solver, we create a 3D cubic array of isothermal Strömgren sphere test problems as described in Sec. 2.4.1, each resolved by a 64^3 cell subvolume of the global mesh. A point source is placed in the center of each subvolume. Each subvolume is assigned to an MPI task which is in turn executed on one core of the Cray XT5 machine "Kraken" operated by the National Institute for Computational Science (NICS) at ORNL. Thus a simulation with P^3 point sources is simulated with a global mesh of dimension $(64P)^3$ cells, and executes on P^3 cores.

Fig. 2.13 shows the weak scaling result for P=2, 4, 8, 16, 32, corresponding to meshes of size 128^3, 256^3, 512^3, 1024^3, and 2048^3 cells. We see that logarithmic scaling is achieved to at least 32,768 MPI tasks (and point sources) on a 2048^3 test problem with 64^3 tiles. This is the expected optimal scaling results, which reflects the scalability of the *hypre* geometric multigrid routines used to solve the linear system of equations resulting from the discretization and linearization of the FLD equation (see Sec. 2.3).

2.4.4 Execution Speed Tests

Here we examine the relative execution speed between a pair of *Enzo* cosmological simulations with and without FLD radiative transfer engaged, henceforth referred to as RHD and HD models, respectively. The RHD model is a simulation of inhomogeneous cosmic reionization in a 80 Mpc comoving volume resolved by a uniform mesh of 3200^3 cells and the same number of dark matter particles. The problem is partitioned into $25^3 = 15,625$ MPI tasks, each of which evolves a 128^3 tile of the global mesh and is assigned to a different processor core. The physics model is as described in Sec. 2.2. The RHD model includes star formation and feedback (radiative, thermal, and chemical) as described in Sec. 2.3.2, FLD radiative transfer, and 6-species primordial gas chemistry and ionization. The simulation was carried out on the Cray XT5 supercomputer architecture *ORNL Jaguar*. The HD model is identical in all respects to the RHD model except that the FLD solver is not called each timestep. The HD simulation corresponds to a primordial 6-species hydro-cosmological simulation with star formation and supernova feedback which is similar in all respects to a standard Lyman alpha forest simulation in which the IGM is ionized by a homogeneous UV background, treated in the optically thin limit (e.g., Jena et al. (2005)).

Fig. 2.14 shows the cumulative wall time per core for the HD and RHD models plotted as a function of 1/z. The inflection in the curves at $1/z \approx 0.07$ corresponds with the onset of star formation at z=14. Subsequently hot $10^6 - 10^7$ K gas is produced by supernova feedback in growing amounts which Courant limits the timestep (see Fig. 2.14) and increases the cost of the HD simulation per unit

time. The RHD model is more costly than the HD model by a factor which grows from $\sim 2\times$ at early times to $\sim 8\times$ at late times. The reason for this is discussed next.

In Fig. 2.15 we plot the timestep size versus 1/z for the two models. Focusing on the curve labeled HD, we see that the timestep drops suddenly by roughly an order of magnitude at $z \approx 0.07$, which marks the onset of star formation. This is due to a more stringent Courant limit on the timestep arising from shock-heated gas surrounding star forming halos. The sharp downward spikes in the timestep curve are short duration transients associated with restarting the calculation. Upon restart, the timestep is set to a low value, and then allowed to float upward at a certain geometric rate per timestep until it again becomes globally Courant-limited. Focussing on the curve labeled RHD, we see that it tracks the HD timestep curve until $1/\mathrm{z} \approx 0.1$, and thereafter slowly decreases until $1/\mathrm{z} \approx 0.13$ where it is about 1/8 the size of the HD timestep. This means that at this time, the RHD simulation is taking $8\times$ as long as the HD simulation to evolve forward in time. The smaller timestep is a consequence of the radiation subcycling algorithm described in Sec. 2.3.4, which takes as input the relative change tolerance parameter τ_{tol}, taken to be 0.01. The steady decrease in the timestep is understood to be the consequence of the growth in the number of grid points in the I-front transition region, which is proportional to the total area of the I-fronts times some skin depth of the transition region.

In order to speed up the simulation, we increased the accuracy parameter τ_{tol} to 0.02 at $1/\mathrm{z} \approx 0.1$. This resulted in an approximately $3\times$ increase in the timestep, as can be seen in Fig. 2.15. Through separate tests on a smaller (1/64) volume test at the same resolution (i.e., an 800^3 simulation), we determined that this change had a $< 5\%$ change on the redshift of overlap, which in the full simulation is $z_{reion} \approx 5.8$. After overlap, we increased the accuracy parameter to τ_{tol} to 0.03, resulting in a RHD timestep which is smaller than the HD timestep by a factor of about 2.5. Using the small box tests, we have determined that if we raise the radiation solve accuracy parameter to τ_{tol} to 0.05, the timestep becomes equal to the Courant-limited HD timestep.

2.5 Example Simulation: Cosmic Reionization by Stellar Sources

To illustrate the application of our radiation hydrodynamic cosmological code we simulate hydrogen reionization due to stellar sources in a comoving volume of (20 Mpc)^3 with a grid resolution of 800^3 and the same number of dark matter particles. This yields a comoving spatial resolution of 25 kpc and dark matter particle mass of $4.8 \times 10^5 M_\odot$. This resolution yields a dark matter halo mass function that is complete down to $M_h = 10^8 M_\odot$, which is by design, since this is the mass scale below which gas cooling becomes inefficient around the redshift range of reionization. However, due to our limited boxsize, our halo mass function is incomplete above $M_h \approx 10^{11} M_\odot$.

We simulate a ΛCDM cosmological model with the following parameters: $\Omega_\Lambda = 0.73$, $\Omega_m = 0.27$, $\Omega_b = 0.047$, $h = 0.7$, $\sigma_8 = 0.82$, $n_s = 0.95$, where these are, respectively, the fraction of the closure density at the present epoch in vacuum energy, matter, baryons; the Hubble contant in units of 100 km/s/Mpc; the power spectrum normalization; and the slope of the scalar fluctuations of the primordial power spectrum. These are consistent with the 7-year WMAP measurements (Komatsu et al., 2011). A Gaussian random field is initialized at z=99 using the *Enzo* initial conditions generator *init* using the Eisenstein & Hu (1999) fits to the transfer functions. The star formation efficiency parameter f_* is adjusted to match the observed star formation rate density in the interval $6 \leq z \leq 10$ from Bouwens et al. (2011). Further details of the simulation input parameters and assumptions are described in Chapter 3. The simulation consumed 255,000 core-hrs running on 512 cores of the Cray XT5 system *Kraken* operated by the National Institute for Computational Science at ORNL.

Fig. 2.16 shows projections of density, radiation energy density, and temperature at z=9.18, 8, 7, and 5.99 through the simulation volume. Reionization begins at $z \approx 10$ with the first luminous sources inflating isolated HII regions, and completes at $z \approx 6$ after the HII regions merge and overlap. The HII regions are roughly spherical until they begin to merge, which is indicative of the photon bud-

get for reionization being dominated by fewer, more luminous sources, as opposed to numerous low luminosity sources Zahn et al. (2007b). In general appearance they are not dissimilar to the post-processing results of Iliev et al. (2006); Trac & Cen (2007). An inspection of the temperature projections shows photoionized gas in yellow, with smaller pockets of shock heated gas near the centers of HII regions, resulting from thermal feedback from supernovae. This simulation is discussed in detail in two forthcoming papers (So et al. 2013a,b).

2.6 Summary and Conclusions

We have described an extension of the *Enzo* code to enable the direct numerical simulation of inhomogeneous cosmological ionization in large cosmological volumes. By direct we mean all dynamical, radiative, and chemical properties are solved self-consistently on the same mesh, as opposed to a postprocessing approach which coarse-grains the radiative transfer, as is done in other works (Iliev et al., 2006; Zahn et al., 2007a; Trac & Cen, 2007; Trac et al., 2008; Shin et al., 2008; Finlator et al., 2009b). Star formation and feedback are treated through a parameterized phenomenological model, which is calibrated to observations. The goal of this work is to achieve a higher level of self-consistency in modeling processes occuring outside the virial radii of luminous sources to better understand how recombinations in the clumpy intergalactic medium retard reionization and how radiative feedback affects star formation in low mass galaxies.

In its current incarnation, the model has three principal limitations. First, it is formulated on a fixed Eulerian grid, which limits the spatial resolution that can be achieved. With a judicious choice of grid sizes and resolutions, one can sample the dark matter halo mass function over a significant range of scales, thereby including important sources and sinks of ionizing radiation. One can do a good job resolving the Jeans length in the diffuse IGM, which is important for "Jeans smoothing" (Gnedin, 2000b). However one cannot resolve the internal structure of halos, which is important for calculating star formation rates and ionizing escape fractions. In this work we do not claim to be modeling these aspects self-

consistently, but rather calibrate these unknown parameters to observations. In Reynolds et al. (2013) we present the extention of our method to adaptive mesh refinement (AMR), which directly addresses the numerical resolution limitation.

The second model limitation is the use of FLD to model the transport of radiation, as opposed to a higher order moment method such as OTVET (Gnedin & Abel, 2001; Petkova & Springel, 2009). FLD has the well known deficiency of not casting shadows behind opaque objects. However, as we have shown in Sec. 2.4, casting shadows is not required to predict the evolution of the ionized volume fraction in a cosmological reionization simulation, or to compute the photoevaporation time for an opaque cloud. Our *a priori* assumption that small scale features like shadows will have little effect on large scale reionization processses are borne out by these validation test. For simulating smaller scale processes where shadows may be important, such as the effect of halo substructure on the escape fraction of ionizing radiation, we note that our implicit solution methodology is easily extended to higher-order moment methods (Hayes & Norman, 2003; Petkova & Springel, 2009).

The third model limitation is our simplified model for the radiation spectrum, which at the moment consists of monochromatic and grey with an assumed fixed SED. For simulating hydrogen reionization by soft UV radiation from stellar sources this spectral model is quite adequate compared to a multifrequency model (see RT09, Sec. 4.1). However for harder radiation sources, such as Pop III stars and AGN, our model makes I-fronts that are too sharp, and does not produce the preheating of gas ahead of the I-front by more penetrating, higher energy photons ("spectral hardening"). The principal difference between our model and a multifrequency/multigroup model is in the temperature distribution of the gas. Our model will slightly overpredict the temperature inside an HII region, and underpredict the temperature outside of it, because all of the radiation energy is absorbed inside the I-front. Another way to think about this is that in the multifrequency model in which the highest energy photons leak out of the HII region, the characteristic temperature of the radiation field inside the HII region is lower than outside of it. The standard approach for dealing with the limitations of our spectral model

is to move to a multifrequency or multigroup discretization of the radiation field (Mirocha et al., 2012). This is straightforward in practice, however the computational cost increases linearly with the number of frequencies/groups. With the speed and memory of modern supercomputers is this not a severe limitation, except for the very largest grids. Indeed we have implemented a multigroup FLD version of our method which is undergoing testing at the present time.

Despite these limitations, the method is robust and acceptably fast. On verification tests for which analytic solutions are known, we have shown the method to be capable of high accuracy; the accuracy being governed by grid resolution and the error tolerance parameter in the radiation diffusion calculation. In validation tests, for which no analytic solution exists, we have shown that our method gives results which are qualitatively and quantitatively similar with those obtained with ray tracing and Monte Carlo methods (Iliev et al., 2006, 2009; Petkova & Springel, 2009; Wise & Abel, 2011), with what differences exist understood to be the result of the geometric simplification of the radiation field inherent in FLD, and the difference in radiation spectrum modeling.

Regarding the speed of our method, we have shown by direct comparison that a radiation hydrodynamic simulation of cosmological reionization costs about $8\times$ that of a corresponding pure hydrodynamic model in which the IGM is ionized by a uniform UV background. We have not compared it to a postprocessing radiative transfer code using ray tracing, although this would be a useful thing to do. Our method, which exhibits $\mathcal{O}(N \log N)$ scaling, should be competitive with, and possibly even beat ray tracing methods for very large numbers of sources.

Our method is highly scalable, as demonstrated in Sec. 4.3. This is due to two factors: (1) modeling radiation as a *field* instead of a collection of rays, which has no explicit dependence on the number of point sources; and (2) the implementation of our radiation solver using optimally scalable parallel multigrid algorithms. The application of our method to cosmological reionization by stellar sources is briefly discussed in Sec. 5 and graphically illustrated in Fig. 16. The largest simulation we have completed to date with our method is identical to design, physics, and numerical resolution as that in Fig. 16, but in a volume 64 times as

large (80 Mpc vs. 20 Mpc). It was carried out on a mesh of size 3200^3 using 46,875 compute cores on the Cray XT5 architecture *Jaguar*. Although the simulation cost many millions of core-hrs to compute, it is the first simulation to cover the full range of halo masses thought to contribute to reionization and at the same time modeling the gravitational, baryonic and radiative feedback processes self-consistently resolving the Jeans smoothing scale in the ionized IGM. The results of this simulation will be presented in forthcoming papers (So et al. 2013a,b).

This research was partially supported by National Science Foundation grants AST-0808184 and AST-1109243 and Department of Energy INCITE award AST025 to MLN and DRR. Simulations were performed on the *Kraken* supercomputer operated for the Extreme Science and Engineering Discovery Environment (XSEDE) by the National Institute for Computational Science (NICS), ORNL with support from XRAC allocation MCA-TG98N020 to MLN. MLN, DRR and GS would like to especially acknowledge the tireless devotion to this project by our co-author Robert Harkness who passed away shortly before this manuscript was completed.

Chapter 2 is a reprint of a paper submitted to Astrophysical Journal without the abstract, M. L. Norman, D. R. Reynolds, R. P. Harkness, and G. C. So, “Direct Numerical Simulation of Reionization I: Numerical Methods and Tests", (submitted ApJ), (2013).

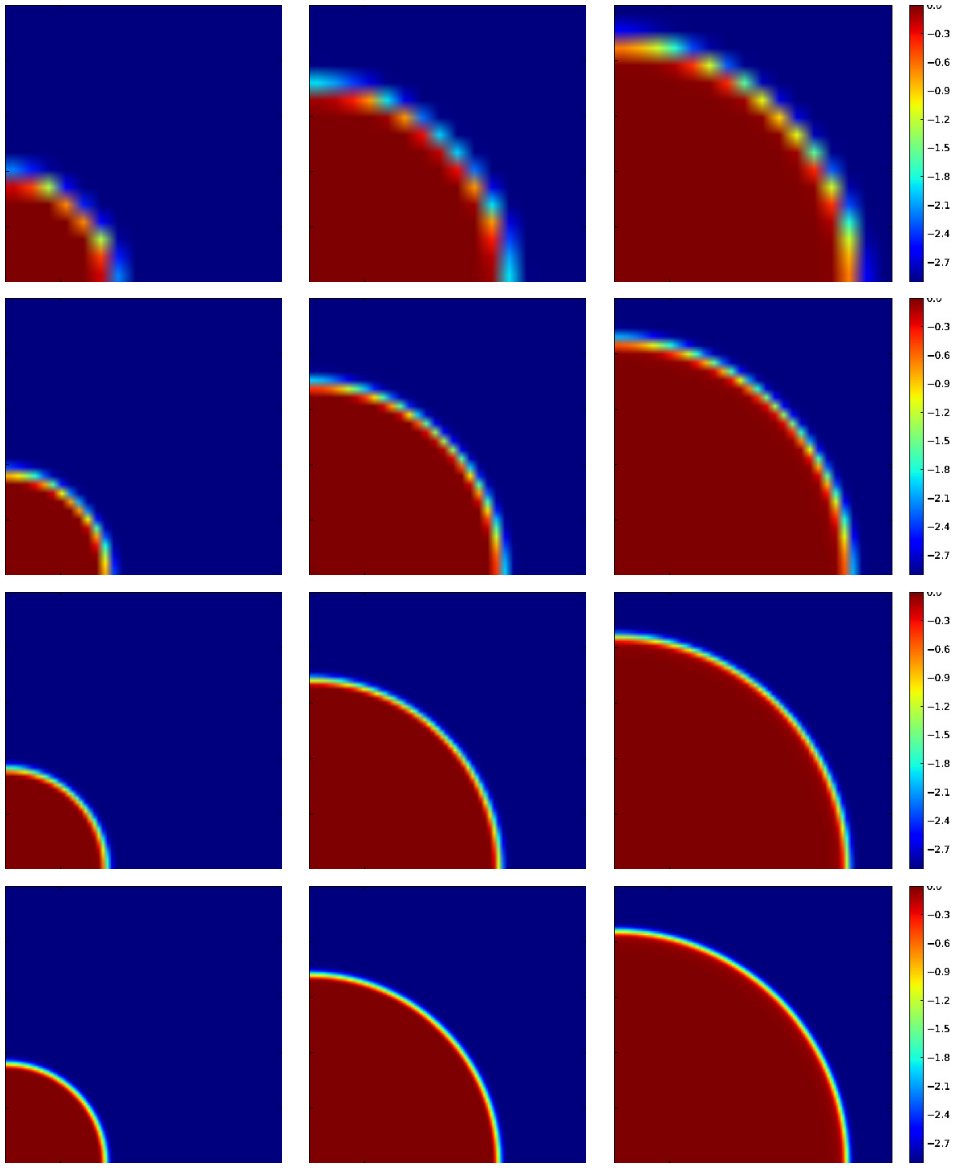

Figure 2.4: HII slices perpendicular to the z axis ($\log_{10}$ scale). We plot the evolution of the ionized region at times of 10, 100 and 500 Myr (columns), and using spatial meshes of 16^3, 32^3, 64^3 and 128^3 (rows), to demonstrate the convergence to a spherical bubble.

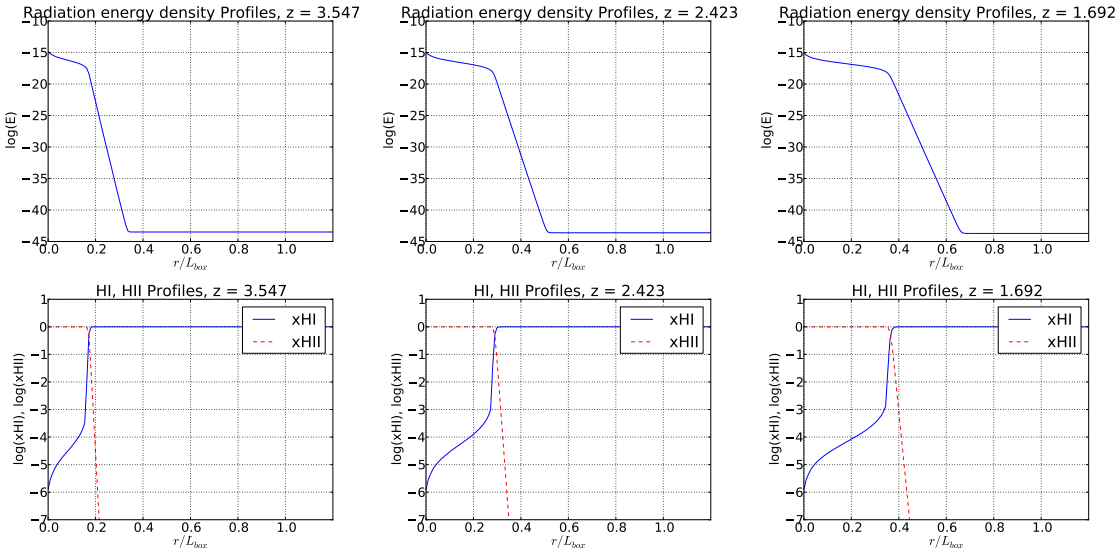

Figure 2.5: Spherically-averaged radial profiles of radiation energy density and ionization fractions for the cosmological ionization test in section 2.4.1 using a 128^3 mesh and time step tolerance $\tau_{tol} = 10^{-4}$. Plots are shown at z=3.547, 2.423 and 1.692 (left to right), with the radiation energy density on the top row and ionization fractions on the bottom row.

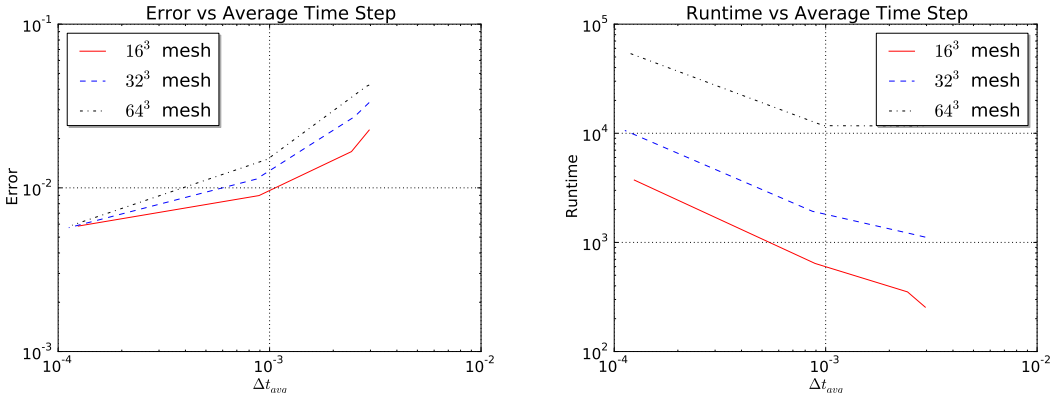

Figure 2.6: We ran tests using mesh sizes of 16^3, 32^3 and 64^4, and time step tolerances of 10^{-2}, 10^{-3}, 10^{-4} and 10^{-5}, and plot the I front position error as a function of the average time step size. As with Figure 2.3, the runtime scales linearly with the inverse Δt_{avg}, and the error scales linearly with Δt_{avg}, at least until other sources of error dominate the calculation.

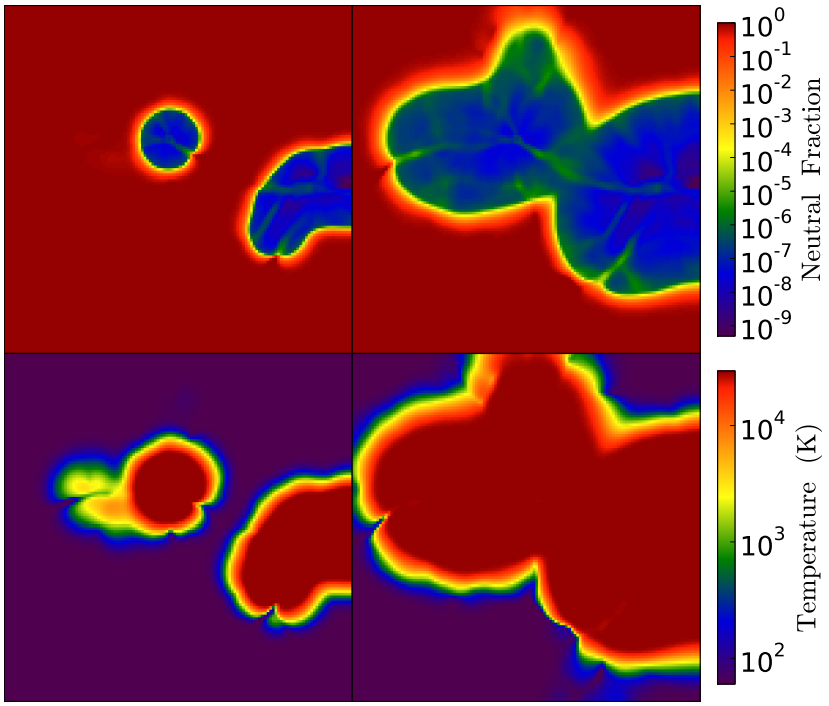

Figure 2.7: Test 4 (reionization of a cosmological density field). Slices of neutral fraction (top) and temperature (bottom) at $t = 50$ kyr (left) and $t = 200$ kyr (right).

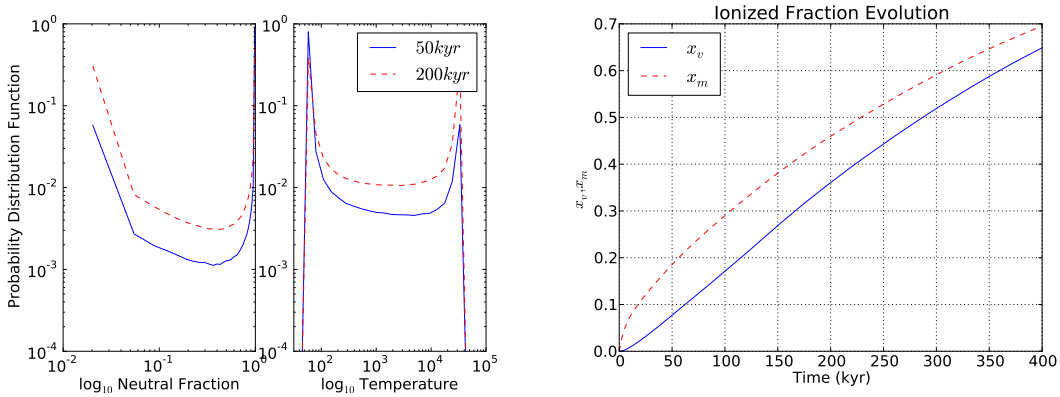

Figure 2.8: Test 4 (reionization of a cosmological density field). Left - probability distribution functions for neutral fraction and temperature at 50 and 200 kyr. Right - evolution of the mass- (dashed) and volume-weighted (solid) ionized fraction.

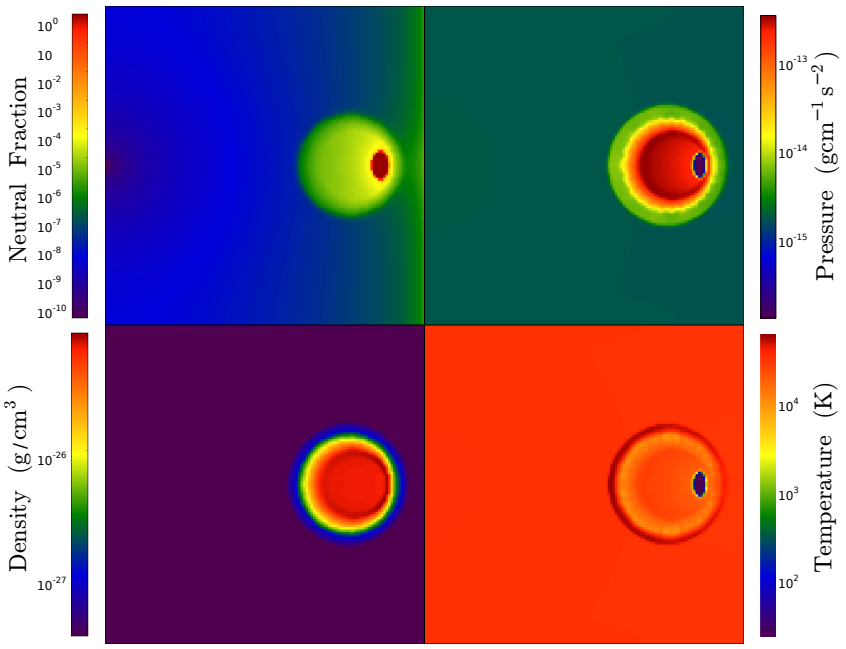

Figure 2.9: Test 7. Photo-evaporation of a dense clump. Clockwise from upper left: Slices through the clump midplane of neutral fraction, pressure, temperature, and density at time $t = 10$ Myr.

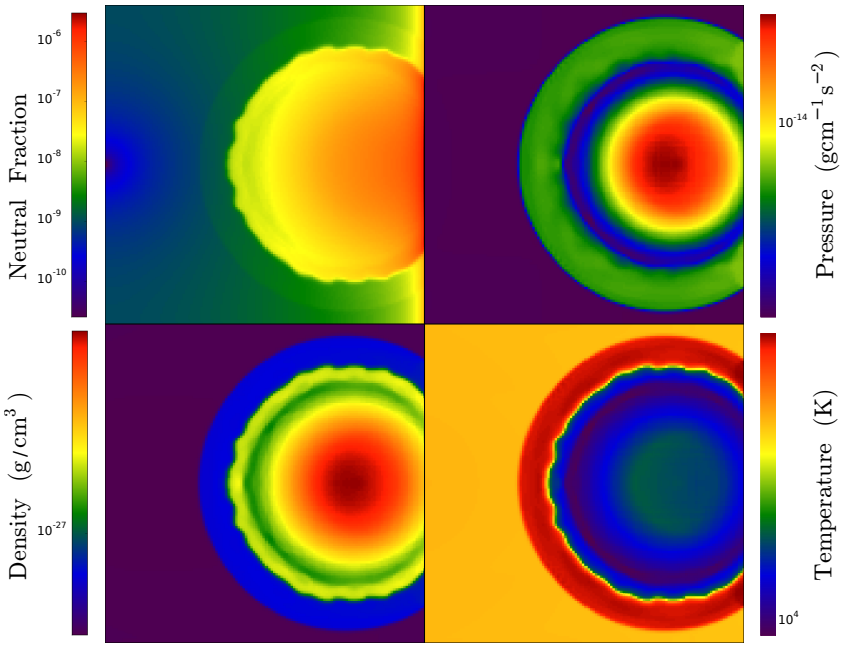

Figure 2.10: Test 7. Photo-evaporation of a dense clump. Same as Fig. 2.9 at time $t = 50$ Myr.

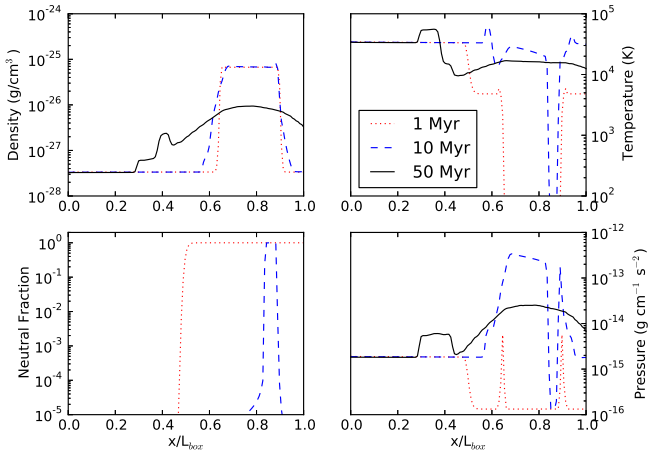

Figure 2.11: Test 7. Photo-evaporation of a dense clump. Line cuts from the point source through the center of the cloud at $t = 1, 10, 50$ Myr for (clockwise from upper left) density, temperature, pressure, and neutral fraction.

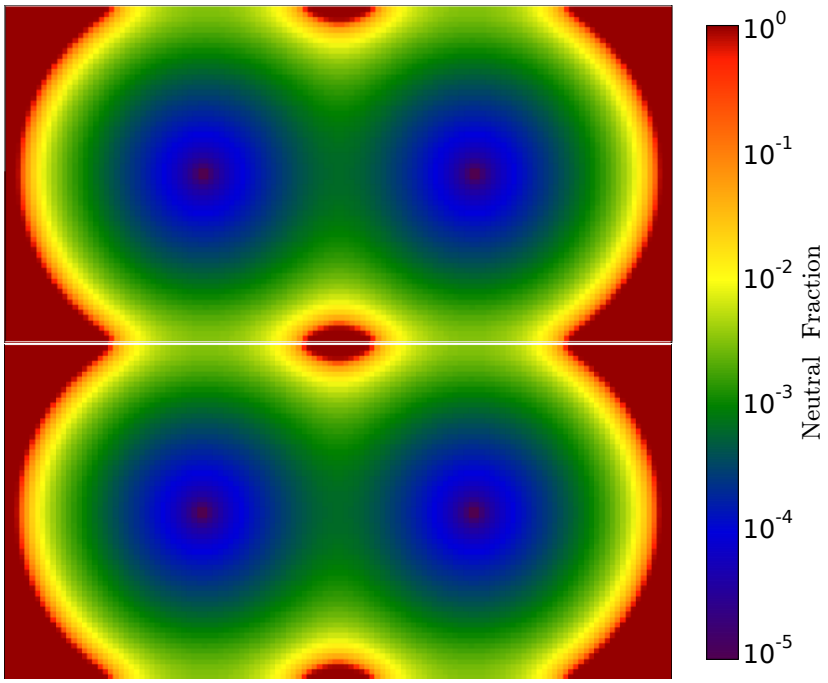

Figure 2.12: Slices of the neutral fraction through the $x - y$ and $x - z$ planes at $t = 500$ Myr in the consolidated HII region test.

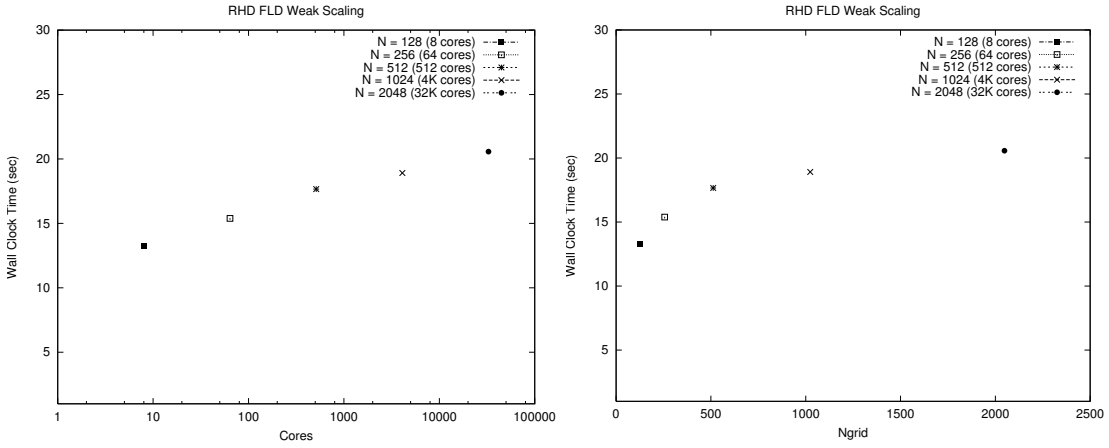

Figure 2.13: Weak scaling test of radiation solver on a Cray XT5 "NICS Kraken". Left: Walltime versus number of cores (1 MPI task per core) for equal workload per core; Right: Walltime versus mesh size, for equal workload per core. Scaling behavior is essentially logN, which is characteristic of geometric multigrid.

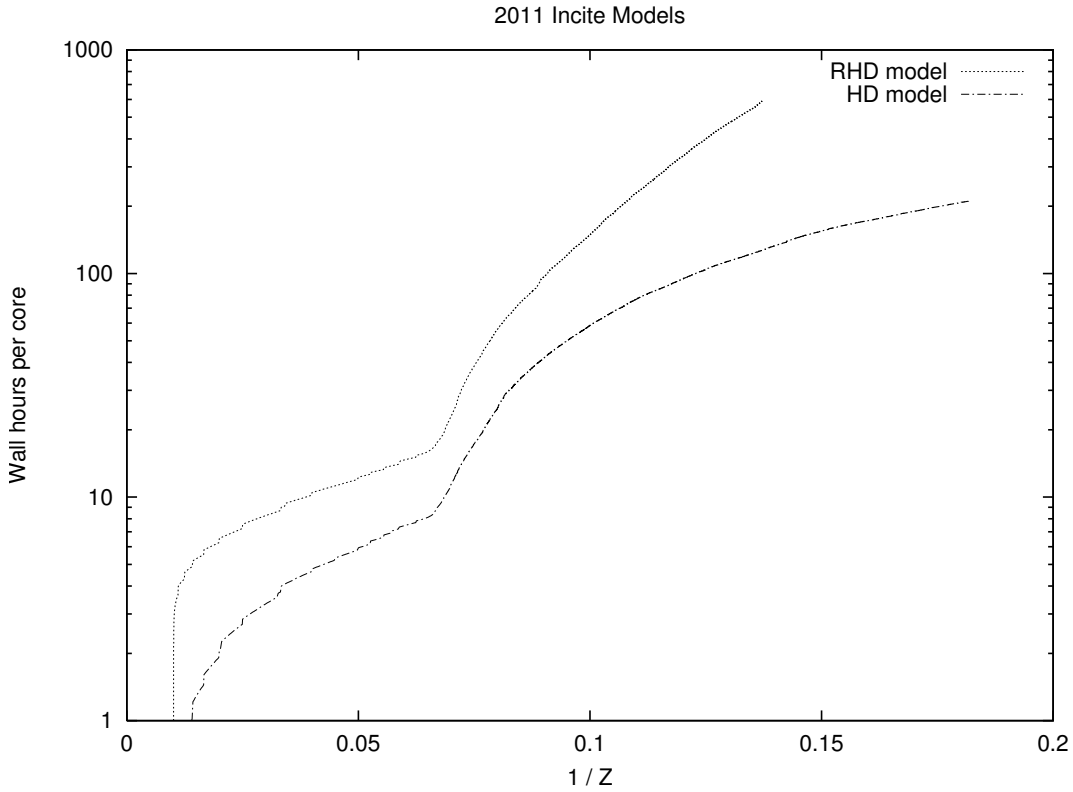

Figure 2.14: Cumulative wall time per processor core as a function of 1/z for the HD and RHD models, which differ only in whether the FLD radiative transfer solver is called (RHD) or not (HD). The inflection in the curves at $1/z \approx 0.07$ corresponds to the onset of Pop II star formation in dwarf galaxies.

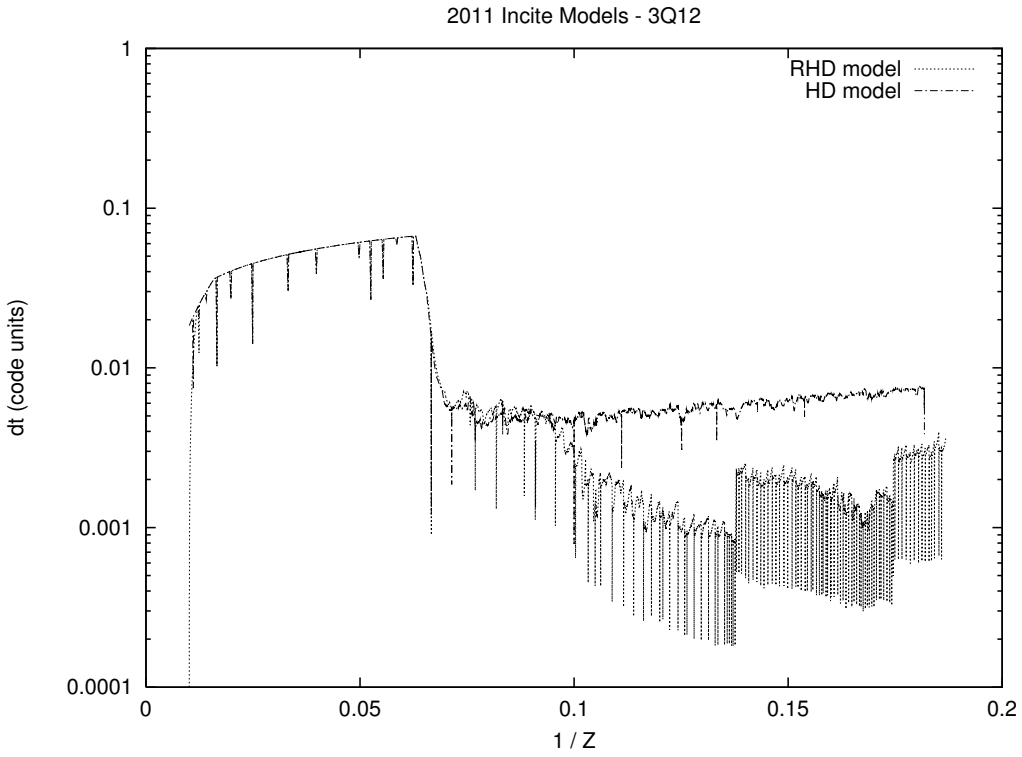

Figure 2.15: Timestep history, measured in code units, for two large cosmological simulations with (RHD) and without (HD) radiative transfer. The simulations use identical cosmological initial conditions within a 80 Mpc periodic box resolved with 3200^3 cells and dark matter particles. The decrease in the RHD timestep at $1/z \approx 0.1$ corresponds to the expansion of the first isolated HII regions. Downward spikes in the curves are transient artifacts resulting from restarting the calculation.

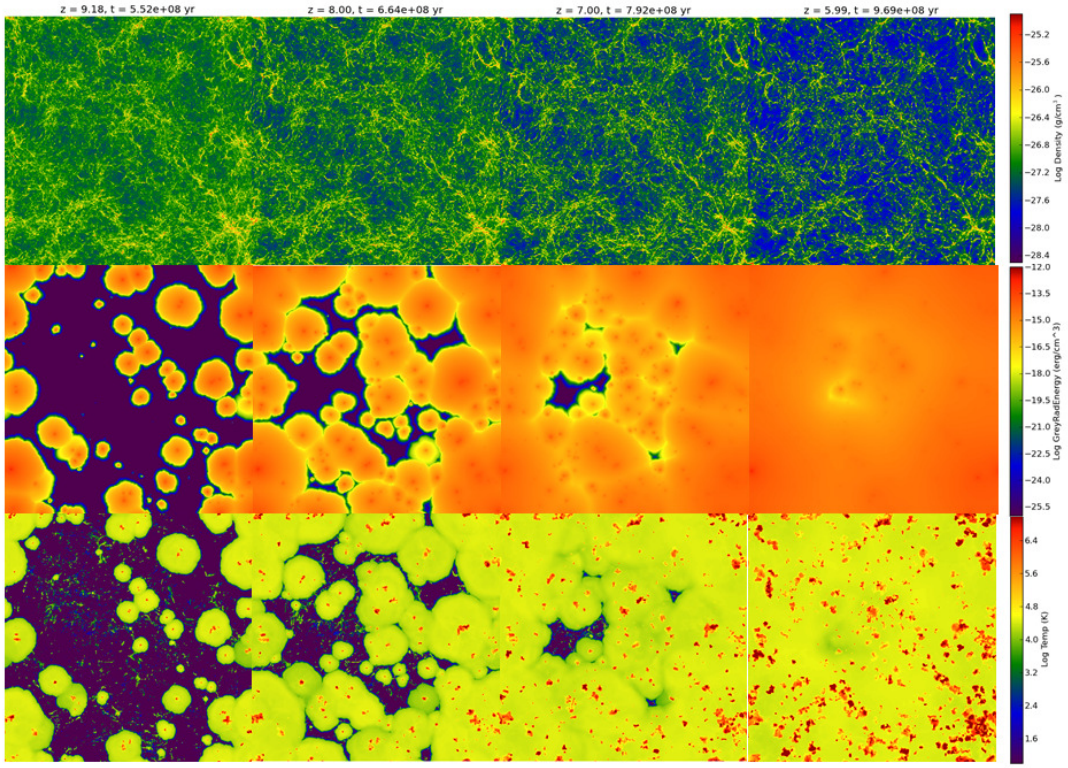

Figure 2.16: Application of the numerical methods described in this paper to cosmological hydrogen reionization. Shown are projections of density, radiation energy density, and temperature at z=9.18, 8, 7, and 5.99 through a (20 Mpc)^3 simulation volume resolved with mesh of 800^3 Eulerian cells and 800^3 dark matter particles.

Chapter 3

Recombinations, Clumping Factors, and the Photon Budget

3.1 Introduction

The Epoch of Reionization (EoR) is an active area of research observationally, theoretically, and computationally. Observations constrain the tail end of hydrogen reionization to the redshift range $z = 6 - 8$ (Robertson et al., 2010). These observations include the presence of Gunn-Peterson troughs in the Ly α absorption spectra of high redshift quasars (Fan et al., 2006), and the strong evolution of Lyman α emitter luminosity function (Robertson et al. 2010 and references therein.) Observations from the WMAP and Planck satellites tell us that the universe was substantially ionized by $z \approx 10$ but can say little about the reionization history or topology (Jarosik et al., 2011; Planck Collaboration et al., 2013). High redshift 21cm observations hold forth great promise of elucidating the details of this transition (Barkana & Loeb, 2007; Pritchard & Loeb, 2012), but these results are still in the future.

It is believed that early star forming galaxies provided the bulk of the UV photons responsible for reionization (Robertson et al., 2010, 2013), but early QSOs may have also contributed (Madau et al., 1999; Bolton & Haehnelt, 2007; Haardt & Madau, 2012). The “galaxy reionizer" hypothesis has been greatly strengthened

by the recent advances in the study of high redshift galaxies afforded by the IR-sensitive Wide Field Camera 3 (WFC3) aboard the Hubble Space Telescope (e.g. Robertson et al., 2010, 2013; Bouwens et al., 2011a,b; Oesch et al., 2013). Within uncertainties, the luminosity function of $z = 6$ Lyman break galaxies (LBGs) appears to be sufficient to account for reionization at that redshift from a photon counting argument (Bolton & Haehnelt, 2007; Robertson et al., 2010; Bouwens et al., 2012). Among the observational uncertainties are the faint-end slope of the galaxy luminosity function (Wise & Cen, 2009; Labbé et al., 2010; Bouwens et al., 2012), the spectral energy distribution of the stellar population (Cowie et al., 2009; Willott et al., 2010; Haardt & Madau, 2012), and the escape fraction of ionizing photons (Wyithe et al., 2010; Yajima et al., 2011; Mitra et al., 2013). Among the theoretical uncertainties are the number of ionizing photons per H atom required to bring the neutral IGM to its highly ionized state by $z = 6$, the clumping factor correction to the mean IGM recombination time (Pawlik et al., 2009; Raicevic & Theuns, 2011; Finlator et al., 2012; Shull et al., 2012; Robertson et al., 2013), and the contribution of Pop III stars and accreting black holes to the early and late stages of reionization (Bolton & Haehnelt, 2007; Trac & Gnedin, 2011; Ahn et al., 2012).

When assessing whether an observed population of high-z galaxies is capable of reionizing the universe (e.g., Bolton & Haehnelt (2007); Robertson et al. (2010)), observers often use the criterion derived by Madau et al. (1999) for the ionizing photon volume density $\dot{\mathcal{N}}_{ion}$ necessary to maintain the clumpy IGM in an ionized state:

$$\dot{\mathcal{N}}_{ion}(z) = \frac{\bar{n}_{\rm H}(0)}{\bar{t}_{rec}(z)} = (10^{51.2} s^{-1} Mpc^{-3}) \left(\frac{C}{30}\right) \times \left(\frac{1+z}{6}\right)^3 \left(\frac{\Omega_b h_{50}^2}{0.08}\right)^2, \tag{3.1}$$

where $\bar{n}_{\rm H}(0)$ is the mean comoving number density of H atoms, $C \equiv \langle n_{\rm H\,II}^2 \rangle / \langle n_{\rm H\,II} \rangle^2$ is the H II clumping factor (angle brackets denote volume average over a suitably large volume that the average is globally meaningful), and the rest of the symbols have their usual meaning. The origin of this formula is a sim-

ple photon counting argument, which says that in order to maintain ionization at a given redshift z, the number of ionizing photons emitted in a large volume of the universe multiplied by a characteristic recombination time, denoted $\bar{t}_{rec}$, must equal the number of hydrogen atoms: $\dot{\mathcal{N}}_{ion} \times \bar{t}_{rec} = \bar{n}_{\rm H}(0)$. The clumping factor enters as a correction factor to account for the density inhomogeneities in the IGM induced by structure formation. We note that $\bar{t}_{rec}$ is not the volume average of the local recombination time of the ionized plasma, as this would heavily weight regions with the *longest* recombination times; i.e. voids. A proper derivation of Equation (3.1) shows that $\bar{t}_{rec} \propto \langle t_{rec}^{-1} \rangle^{-1}$, which weights regions with the *shortest* recombination times; i.e. regions at the mean density and above.

Equation (3.1) is based on a number of simplifying assumptions discussed by Madau et al. (1999), including the assumption $\bar{t}_{rec} \ll t$. It is this assumption that allows history-dependent effects to be ignored, and a quasi-instantaneous analysis of the photon budget for reionization to be done. The validity of this assumption is naturally redshift dependent, but it is also dependent upon the adopted definition of $\bar{t}_{rec}$. A second comment about Equation (3.1) is that it does not ask how many ionizing photons per H atom are required to convert a neutral IGM to a fully ionized one, only how many are required to *maintain* the IGM in an ionized state. Because the recombination time is short at high redshifts, it is expected that this number is greater than one.

In this paper we examine these and related topics within the context of a direct numerical simulation of cosmic reionization based on a new flux-limited diffusion radiation transport solver installed in the *Enzo* code (Norman et al., 2013) (hereafter Paper I). Our approach self-consistently couples all the relevant physical processes (gas dynamics, dark matter dynamics, self-gravity, star formation/feedback, radiative transfer, nonequilibrium ionization/recombination, heating and cooling) and evolves the system of coupled equations on the same high resolution mesh. We refer to this approach as *direct numerical simulation* or *resolution matched*, in contrast to previous approaches which decouple and coarse-grain the radiative transfer and ionization balance calculations relative to the underlying dynamical calculation. Our method is scalable with respect to the number of radi-

ation sources, size of the mesh, and the number of computer processors employed. This scalability permits us to simulate cosmological reionization in large cosmological volumes (L $\sim$ 100 Mpc) while directly modeling the sources and sinks of ionizing radiation, including radiative feedback effects such as photoevaporation of gas from halos, Jeans smoothing of the IGM, and enhanced recombination due to small scale clumping. In this the first of several application papers, we investigate in a volume of modest size (L=20 Mpc) the mechanics of reionization from stellar sources forming in high-z galaxies, the role of gas clumping, recombinations, and the photon budget required to complete reionization.

By analyzing this simulation we are able to critically examine the validity of Equation (3.1) as a predictor of when the end of EoR will occur, and we can calculate the integrated number of ionizing photons per H atom needed to ionize the simulated volume $\gamma_{ion}/H = \int dt \dot{\mathcal{N}}_{ion}/\bar{n}_{\rm H}(0)$. Ignoring recombinations within the virial radii of collapsed halos, we find $\gamma_{ion}/H \approx 2$. This result supports the "photon starved" reionization scenario discussed by Bolton & Haehnelt (2007). We also examine whether modern revisions to Equation (3.1) using alternatively defined clumping factors (Pawlik et al., 2009; Raicevic & Theuns, 2011; Finlator et al., 2012; Shull et al., 2012) are improvements over the original. We find they systematically overestimate the redshift of reionization completion z_{reion} because the condition $\bar{t}_{rec}/t \ll 1$ is never obeyed. We study the accuracy and validity of the time-dependent analytic model of Madau et al. (1999), and find that while it is in better agreement with the simulation, it also overestimates z_{reion} because it ignores important corrections to the ionization term at early and late times.

This paper is organized as follows: in §3.2 we discuss the design criteria for the simulation and briefly outline the basic equations and implementation of the FLD radiation transport model, referring the reader to Paper I for a more complete description of the numerical algorithms and tests. In §3.3, we present some general features of the simulation and demonstrate its broad consistency with the observed star formation rate density and high redshift galaxy luminosity function. In §3.4 we examine the accuracy of different clumping factor approaches to estimating the redshift of complete reionization. In §3.5 we derive a global estimate for the

circumgalactic absorption of ionizing radiation from our simulation. In §3.6 we test a simple analytic model for the evolution of the ionized volume fraction $Q_{\rm H\,II}$ and present an improvement to the model which better agrees with our simulation. In §3.7 we discuss implications of our results on the current understanding of reionization. And finally, in §3.8 we end with a summary of our main results and conclusions.

3.2 Method

3.2.1 Simulation Goals and Parameters

We use the Enzo code (The Enzo Collaboration et al., 2013), augmented with a flux-limited diffusion radiative transfer solver and a parameterized model of star formation and feedback (Norman et al., 2013) to simulate inhomogeneous hydrogen reionization in a 20 Mpc comoving box in a WMAP7 ΛCDM cosmological model. Details of the numerical methods and tests are provided in Paper I. Here we briefly describe the simulation's scientific goals and design considerations to put it into perspective with other reionization simulations. For completeness, the physical equations we solve and the treatment of the ionizing sources and radiation field are included below.

Our principal goal is to simulate the physical processes occurring in the IGM outside the virial radii of high redshift galaxies in a *representative* realization of inhomogeneous reionization. We wish to simulate the early, intermediate, and late phases of reionization in a radiation hydrodynamic cosmological framework so that we may study the nonequilibrium ionization/recombination processes in the IGM at reasonably high resolution self-consistently coupled to the dynamics. In this way we can study such effects as optically thick heating behind the I-fronts (Abel & Haehnelt, 1999), Jeans smoothing (Shapiro et al., 1994; Gnedin, 2000b), photoevaporation of dense gas in halos (Shapiro et al., 2004), and nonequilibrium effects in the low density voids. Because we carry out our simulation on a fixed Eulerian grid, we do not resolve the internal processes of protogalaxies very well. In this sense, our simulation is not converged on all scales. Nonetheless Equa-

tions (3.2) to (3.7) are solved everywhere on the mesh self-consistently, including ionization/recombination and radiative transfer inside protogalaxies. The escape of ionizing radiation from galaxies to the IGM is thus simulated directly, and not introduced as a parameter. We use a star formation recipe that can be tuned to closely reproduce the observed high-z galaxy luminosity function (LF), star formation rate density (SFRD), and redshift of reionization completion. This gives us confidence that we are simulating IGM processes in a realistic scenario of reionization.

We simulate a WMAP7 (Jarosik et al., 2011) ΛCDM cosmological model with the following parameters: $\Omega_\Lambda = 0.73$, $\Omega_m = 0.27$, $\Omega_b = 0.047$, $h = 0.7$, $\sigma_8 = 0.82$, $n_s = 0.95$, where the symbols have their usual meanings. A Gaussian random field is initialized at $z = 99$ using the *Enzo* initial conditions generator *inits* using the Eisenstein & Hu (1999) fits to the transfer functions.The simulation is performed in a comoving volume of (20 Mpc)^3 with a grid resolution of 800^3 and the same number of dark matter particles. This yields a comoving spatial resolution of 25 kpc and dark matter particle mass of $4.8 \times 10^5 M_\odot$. This resolution yields a dark matter halo mass function that is complete down to $M_h = 10^8 M_\odot$, which is by design, since this is the mass scale below which gas cooling becomes inefficient. However, due to our limited boxsize, our halo mass function is incomplete above $M_h \approx 10^{11} M_\odot$ (see Figure 3.4). In a forthcoming paper we will report on a simulation of identical design and resolution as this one, but in a volume 64 times as large, which contains the rarer, more massive halos. With regard to resolving the diffuse IGM, our 25 kpc resolution equals the value recommended by Bryan et al. (1999) to converge on the properties of the Ly α forest at lower redshifts, is 3× better than the optically thin high resolution IGM simulation described in Shull et al. (2012), and nearly 4× better than the inhomogeneus reionization simulation described in Trac et al. (2008).

As described below in §3.2.4, we use a parameterized model of star formation calibrated to observations of high redshift galaxies. The star formation efficiency parameter f_* is adjusted to match the observed star formation rate density in the interval $6 \leq z \leq 10$ from Bouwens et al. (2011a). The simulation consumed

255,000 core-hrs running on 512 cores of the Cray XT5 system *Kraken* operated by the National Institute for Computational Science at ORNL.

3.2.2 Governing Equations

The equations of cosmological radiation hydrodynamics implemented in the Enzo code used for this research are given by the following system of partial differential equations (Paper I):

$$\nabla^2\phi = \frac{4\pi g}{a}(\rho_b + \rho_{\rm dm} - \langle\rho\rangle), \tag{3.2}$$

$$\partial_{\rm t}\rho_b + \frac{1}{a}\mathbf{v}_b\cdot\nabla\rho_b = -\frac{1}{a}\rho_b\nabla\cdot\mathbf{v}_b - \dot{\rho}_{SF}, \tag{3.3}$$

$$\partial_{\rm t}\mathbf{v}_b + \frac{1}{a}\left(\mathbf{v}_b\cdot\nabla\right)\mathbf{v}_b = -\frac{\dot{a}}{a}\mathbf{v}_b - \frac{1}{a\rho_b}\nabla p - \frac{1}{a}\nabla\phi, \tag{3.4}$$

$$\begin{aligned}\partial_{\rm t}e + \frac{1}{a}\mathbf{v}_b\cdot\nabla e = &-\frac{2\dot{a}}{a}e - \frac{1}{a\rho_b}\nabla\cdot(p\mathbf{v}_b)\\ &- \frac{1}{a}\mathbf{v}_b\cdot\nabla\phi + G - \Lambda + \dot{e}_{SF}\end{aligned} \tag{3.5}$$

$$\begin{aligned}\partial_{\rm t}\mathtt{n}_{\rm i} + \frac{1}{a}\nabla\cdot(\mathtt{n}_{\rm i}\mathbf{v}_b) &= \alpha_{\rm i,j}\mathtt{n}_{\rm e}\mathtt{n}_{\rm j} - \mathtt{n}_{\rm i}\Gamma^{ph}_{\rm i},\\ &i = 1,\ldots,N_{\rm s}\end{aligned} \tag{3.6}$$

$$\begin{aligned}\partial_{\rm t}E + \frac{1}{a}\nabla\cdot(E\mathbf{v}_b) = &\nabla\cdot(D\nabla E) - \frac{\dot{a}}{a}E\\ &- c\kappa E + \eta\end{aligned} \tag{3.7}$$

Equation (3.2) describes the modified gravitational potential ϕ due to baryon density $\rho_{\rm b}$ and dark matter density $\rho_{\rm dm}$, with a being the cosmological scale factor, g being the gravitational constant, and $\langle\rho\rangle$ being the cosmic mean density. The collisionless dark matter density $\rho_{\rm dm}$ is evolved using the Particle Mesh method (equation not shown above), as described in Hockney & Eastwood 1988; The Enzo Collaboration et al. 2013. Equations (3.3), (3.4) and (3.5) are conservation of mass, momentum and energy, respectively, in a comoving coordinate system (Bryan et al., 1995; The Enzo Collaboration et al., 2013). In the above equations, $\mathbf{v}_b \equiv a(t)\dot{\mathbf{x}}$ is the proper peculiar baryonic velocity, p is the proper pressure, e is the total energy per unit mass, and G and Λ are the heating and cooling coefficients. Equation (3.6)

describes the chemical balance between the different ionization species (in this paper we used H I, H II, He I, He II, He III densities) and electron density. Here, $\mathtt{n}_{\mathrm{i}}$ is the comoving number density of the i^{th} chemical species, $\mathtt{n}_{\mathrm{e}}$ is the electron number density, $\mathtt{n}_{\mathrm{j}}$ is the ion that reacts with species i, and $\alpha_{\mathrm{i,j}}$ are the reaction rate coefficient between species i and j (Abel et al., 1997; Hui & Gnedin, 1997), and finally Γ_{i}^{ph} is the photoionization rate for species i.

3.2.3 Radiation Transport

Equation (3.7) describes radiation transport in the Flux Limited Diffusion (FLD) approximation in an expanding cosmological volume (Reynolds et al., 2009; Norman et al., 2013). E is the comoving grey radiation energy density. The *flux limiter* D is a function of E, ∇E, and the opacity κ (Morel, 2000), and has the form:

$$D = \mathrm{diag}\left(D_1, D_2, D_3\right), \quad \text{where} \tag{3.8}$$

$$D_{\mathrm{i}} = c\left(9\kappa^2 + R_{\mathrm{i}}^2\right)^{-1/2}, \quad \text{and} \tag{3.9}$$

$$R_{\mathrm{i}} = \max\left\{\frac{|\partial_{\mathrm{x_i}} E|}{E}, 10^{-20}\right\} \tag{3.10}$$

In the calculation of the grey radiation energy density E, we assume $E_\nu(\mathbf{x}, t, \nu) = \tilde{E}(\mathbf{x}, t)\,\chi_E(\nu)$, therefore:

$$\begin{aligned} E(\mathbf{x}, t) &= \int_{\nu_1}^{\infty} E_\nu(\mathbf{x}, t, \nu)\,\mathrm{d}\nu \\ &= \tilde{E}(\mathbf{x}, t) \int_{\nu_1}^{\infty} \chi_E(\nu)\,\mathrm{d}\nu, \end{aligned} \tag{3.11}$$

which separates the dependence of E on coordinate $\mathbf{x}$ and time t from frequency ν. Here χ_E is the spectral energy distribution (SED) taken to be that of a Pop II stellar population similiar to one from (Ricotti et al., 2002).

3.2.4 Star Formation and Feedback

Because star formation occurs on scales not resolved by our uniform mesh simulation, we rely on a subgrid model which we calibrate to observations of star

formation in high redshift galaxies. The subgrid model is a variant of the Cen & Ostriker (1992) prescription with two important modifications as described in Smith et al. (2011). In the original Cen & Ostriker (1992) recipe, a computational cell forms a collisionless “star particle" if a number of criteria are met: the baryon density exceeds a certain numerical threshold; the gas velocity divergence is negative, indicating collapse; the local cooling time is less than the dynamical time; and the cell mass exceeds the Jeans mass. In our implementation, the last criterion is removed because it is always met in large scale, fixed-grid simulations, and the overdensity threshold is taken to be $\rho_b/(\rho_{c,0}(1+z)^3) > 100$, where $\rho_{c,0}$ is the critical density at $z = 0$. If the three remaining criteria are met, then a star particle representing a large collection of stars is formed in that timestep and grid cell with a total mass

$$m_* = f_* m_{cell} \frac{\Delta t}{t_{dyn}}, \tag{3.12}$$

where f_* is an efficiency parameter we adjust to match observations of the cosmic star formation rate density (SFRD) (Bouwens et al., 2011a), m_{cell} is the cell baryon mass, t_{dyn} is the dynamical time of the combined baryon and dark matter fluid, and Δt is the hydrodynamical timestep. An equivalent amount of mass is removed from the grid cell to maintain mass conservation.

Although the star particle is formed instantaneously (i.e., within a single timestep), the conversion of removed gas into stars is assumed to proceed over a longer timescale, namely t_{dyn}, which more accurately reflects the gradual process of star formation. In time Δt, the amount of mass from a star particle converted into newly formed stars is given by

$$\Delta m_{SF} = m_* \frac{\Delta t}{t_{dyn}} \frac{t - t_*}{t_{dyn}} e^{-(t-t_*)/t_{dyn}}, \tag{3.13}$$

where t is the current time and t_* is the formation time of the star particle. To make the connection with Equation (3.4), we have $\dot{\rho}_{SF} = \Delta m_{SF}/(V_{cell}\Delta t)$, where V_{cell} is the volume of the grid cell.

Stellar feedback consists of the injection of thermal energy, gas, and radiation to the grid, all in proportion to Δm_{SF}. The thermal energy Δe_{SF} and gas

mass Δm_g returned to the grid are given by

$$\Delta e_{SF} = \Delta m_{SF} c^2 \epsilon_{SN}, \qquad \Delta m_g = \Delta m_{SF} f_{m*}, \tag{3.14}$$

where c is the speed of light, ϵ_{SN} is the supernova energy efficiency parameter, and $f_{m*} = 0.25$ is the fraction of the stellar mass returned to the grid as gas. Rather than add the energy and gas to the cell containing the star particle, as was done in the original Cen & Ostriker (1992) paper, we distribute it evenly among the cell and its 26 nearest neighbors to prevent overcooling. As shown by Smith et al. (2011), this results in a star formation recipe which can be tuned to reproduce the observed SFRD. This is critical for us, as we use the observed high redshift SFRD to calibrate our reionization simulations.

To calculate the radiation feedback, we define an emissivity field $\eta(x)$ on the grid which accumulates the instantaneous emissivities of all the star particles within each cell. To calculate the contribution of each star particle i at time t we assume an equation of the same form for supernova energy feedback, but with a different energy conversion efficiency factor ϵ_{UV}. Therefore

$$\eta = \sum_{\mathrm{i}} \epsilon_{\mathrm{uv}} \frac{\Delta m_{\mathrm{SF,i}} c^2}{V_{\mathrm{cell}} \Delta t} \tag{3.15}$$

Emissivity η is in units of erg $\mathrm{s}^{-1}\mathrm{cm}^{-3}$. The UV efficiency factor ϵ_{uv} is taken from Ricotti et al. (2002) as $4\pi \times 1.1 \times 10^{-5}$, where the factor 4π comes from the conversion from mean intensity to radiation energy density.

3.2.5 Data Analysis

Due to the enormous amount of data produced by the simulation (one output file is about 100 GB), we needed a scalable tool suited to the task of organizing and manipulating the data into human readable form. We use the analysis software tool `yt` (Turk et al., 2011) specifically created for doing this type of vital task. It is a python based software tool that does "Detailed data analysis and visualizations, written by working astrophysicists and designed for pragmatic analysis needs." `yt` is open source and publicly available at http://yt-project.org.

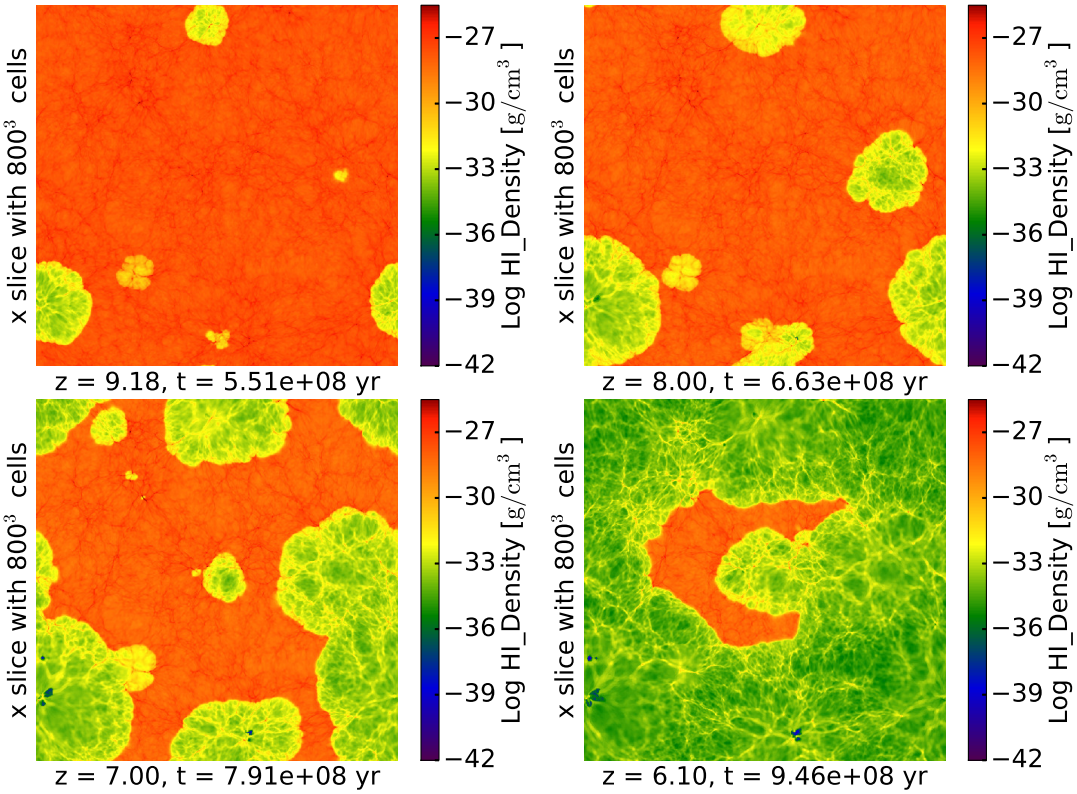

Figure 3.1: H I density on slices through the 20 Mpc volume showing the growth, percolation, and final overlap of H II regions. Panels show $z = 9.18, 8.0, 7.0, 6.1$. The box becomes fully ionized at $z = 5.8$ as the last neutral islands are overrun by the I-fronts. Regions of extremely low H I density are shock-heated bubbles due to supernova feedback.

3.3 General Results

Here we first present the basic properties of the simulation before delving into specific topics in subsequent sections. The star formation and feedback parameters for this simulation are $f_* = 0.1, f_{m*} = 0.25, \epsilon_{SN} = 10^{-5}, \epsilon_{UV} = 1.38 \times 10^{-4}$. Figure 3.1 shows the reionization process as it proceeds through growth, percolation, and final overlap of ionized hydrogen (H II) regions driven by ionizing radiation from star forming galaxies. We plot the neutral hydrogen (H I) density on a slice through the densest cell in the volume at redshifts $z = 9.18, 8.0, 7.0, 6.1$. At $z = 9.18$ several isolated quasi-spherical I-fronts are intersected by the slice

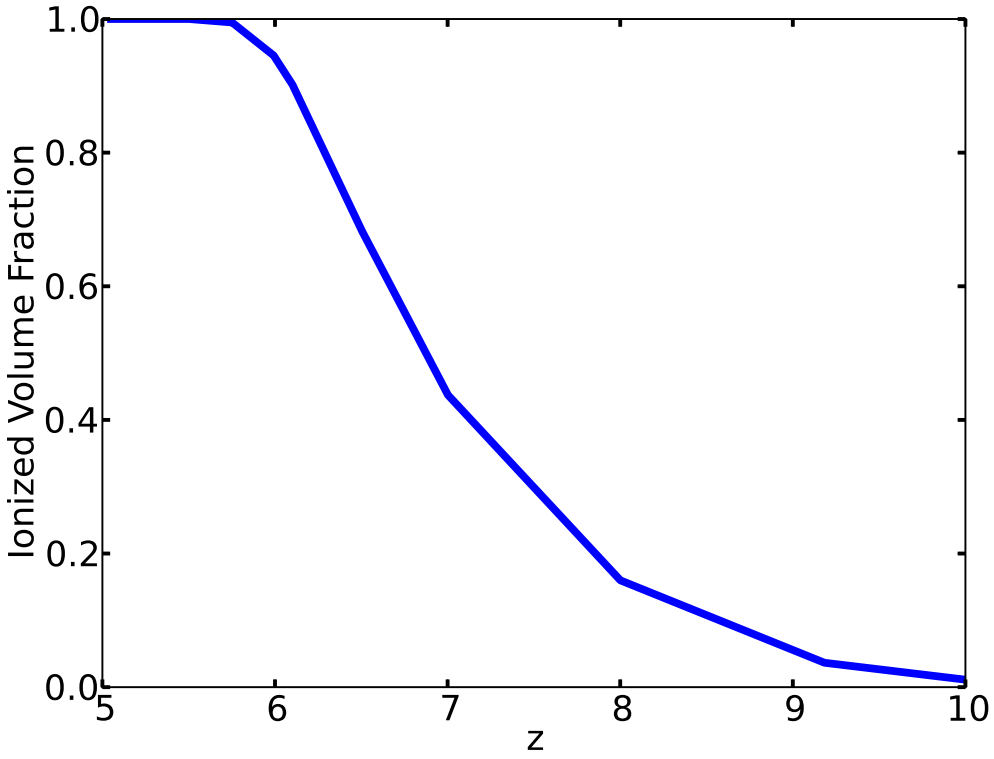

Figure 3.2: Evolution of the ionized volume fraction versus redshift for hydrogen ionized to less than 1 neutral in 10^3 atoms. As redshift decreases, the volume filling fraction grows rapidly until around redshift of 6, at which time the rate of growth slows significantly as the last neutral island is ionized . The sensitivity of this curve to ionization level is discussed in §3.3.1.

plane. These grow and have begun to merge by $z = 8.0$. By $z = 7.0$ the topology is beginning to invert, in that there are now isolated peninsulas of H I gas embedded in an otherwise ionized IGM. By $z = 6.1$ the remaining neutral island has almost disappeared as it is being irradiated from all sides. We can also see in the figure small patches of extremely low H I density; these correspond to bubbles of shock heated gas near galaxies heated to above 10^6K in temperature by supernova feedback.

Figure 3.2 plots the evolution of the ionized volume fraction $Q_{\rm H\,II}$ versus redshift. Here a cell is called ionized if $\rho_{\rm H\,II}/\rho_{\rm H} \geq 0.999$ (In §3.3.1 we discuss the

sensitivity of this curve to level of ionization.) The first ionizing sources turn on at $z \sim 10$ in this simulation. The ionized volume fraction rises rapidly, reaching 0.5 at $z \approx 6.8$, 0.95 at $z \approx 6.0$, and near unity at $z \approx 5.8$. We compare this evolution with the predictions of the simple analytic model introduced by Madau et al. (1999) in §3.6. For now we only draw attention to the flattening of the curve in the redshift interval $5.8 \leq z \leq 6$. This is the signature of neutral islands being ionized by I-fronts converging in 3D, as opposed to being ionized by internal sources.

Our simulation was not designed to complete reionization by a certain fiducial redshift. Rather we adjusted our star formation efficiency parameter f_* so that we can approximately match the star formation rate density (SFRD) in (Bouwens et al., 2011a). Our SFRD is shown in Figure 3.3, along with the Bouwens data, plotted without error bars. For reference we also include the fitting function described in (Haardt & Madau, 2012). This shows that our simulated universe is one that produces approximately the same amount of stars in a given comoving volume, albeit a bit low relative to the data. We also note that the SFRD begins to flatten out at $z \approx 6.5$, and even turns over after overlap at $z \approx 5.8$, rather than continuing to rise as indicated by the data points. This is an artifact of the small box size as a simulation completed in a 80 Mpc comoving on a side box with identical physics, mass, and spatial resolution and star formation/feedback parameters does not show this slowing down of the SFRD. This will be reported on in a future paper.

To check and make sure that our simulation is giving us a fair representation of the universe, we plot several more quantities and look for any anomalies. In Figure 3.4, we see that our halo mass function at redshift of $z \sim 6$ matches well with the Warren fit implemented in `yt` (Warren et al., 2006; Turk et al., 2011). The mass function captures haloes down to $\sim 10^8 M_\odot$, which as previously stated was a simulation design criterion. The haloes are found by first running the parallelHOP halo finder installed in `yt` (Skory et al., 2010), then taking the linked list of dark matter particles for each halo and wrapping the region around them in an ellipsoidal 3D container introduced in `yt` 2.4. The 3D container enables the query of the fluid

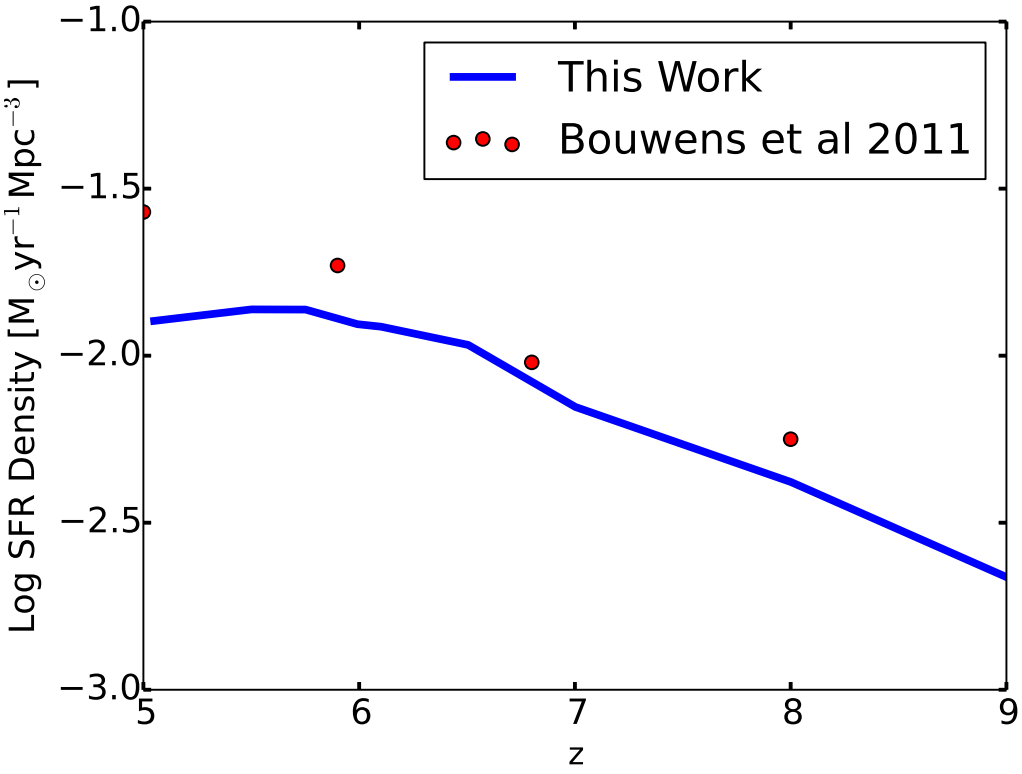

Figure 3.3: A comparison of simulated and observed star formation rate densities (SFRD) in units of $M_\odot yr^{-1}Mpc^{-3}$ comoving. Blue curve labeled "This Work" is from our 20 Mpc / 800^3 simulation, and "Bouwens et al 2011" are observationally derived data points from Bouwens et al. (2011b) plotted without error bars. The leveling off of the simulated SFRD is an artifact of the small volume as a simulation carried out with identical physics, mass, and spatial resolution but in 64 times the volume does not show this effect.

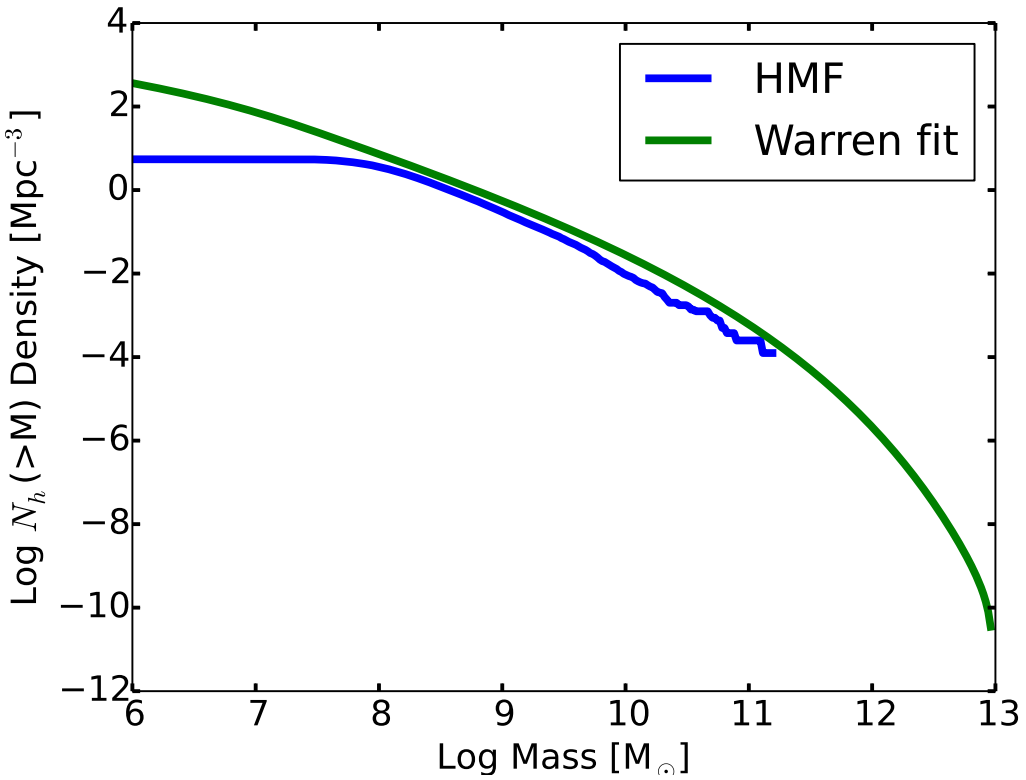

Figure 3.4: The dark matter halo mass function from our simulation (blue line). Green line is the fit from (Warren et al., 2006). Our low-mass HMF is reasonably complete down to $M_{halo} \approx 10^8 M_\odot$; i.e. halos believed to form stars efficiently due to atomic line cooling. Incompleteness at the high mass end is due to the limited volume sampled.

quantities of the haloes, such as baryonic, emissivity, radiation contents in addition to the particle information. Since the dark matter particles used are $\sim 5\times\ 10^5 \mathrm{M}_\odot$, the $10^8 \mathrm{M}_\odot$ dark matter haloes are considered to be resolved (Trenti et al., 2010).

As a final check that our ionizing source population is not wildly unrepresentative of the observed universe, in Figure 3.5 we plot the luminosity function of our simulated galaxies at $z = 6.1$ alongside the observational data points from Table 5 of (Bouwens et al., 2007). The points in red are the bolometric luminosities for our galaxy population calculated directly from the $z = 6.1$ halo catalogue. To calculate the luminosity of a given halo we sum the emissivity field within the

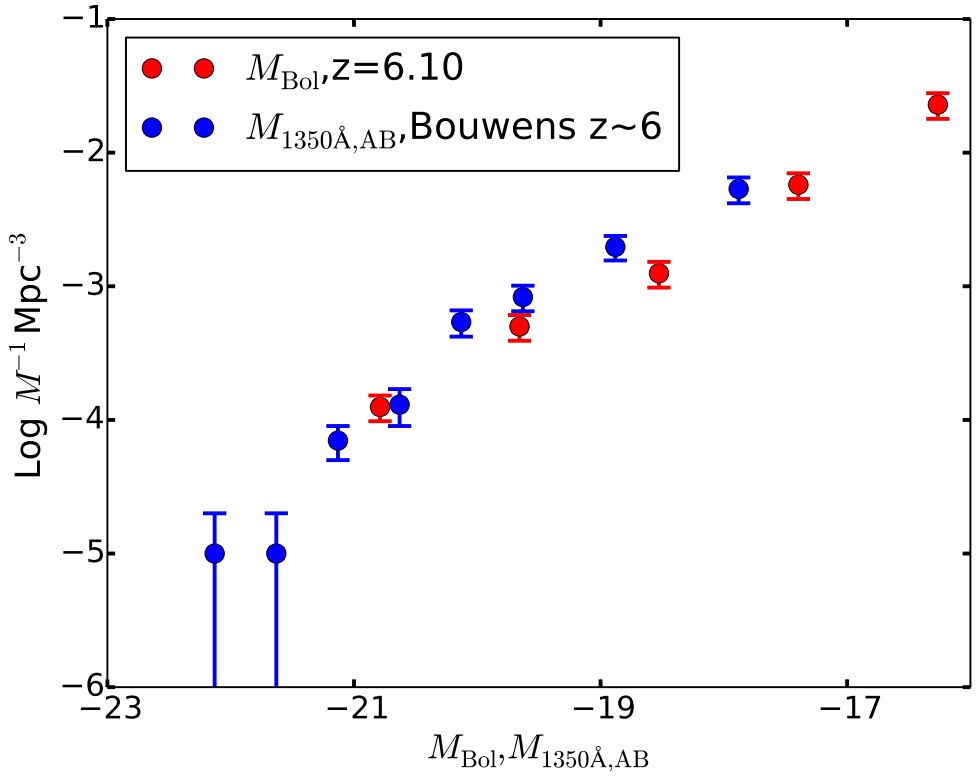

Figure 3.5: Bolometric luminosity function derived from our simulation data (red), compared with observational data points (blue) from (Bouwens et al., 2007).

3D ellipsoidal containers defined by the halos' dark matter particles. Our error bars are taken using one standard deviation of luminosity in the mass bins. Although this is not proof that our simulation is matching observations exactly, it does lend support that our realization of reionization is being driven by sources not too dissimilar to those observed and is sufficient for the purposes of this study.

3.3.1 Quantitative Language

Earlier works on reionization such as Valageas & Silk (1999); Gnedin (2000a); Miralda-Escudé et al. (2000); Iliev et al. (2006) speak of a two phase medium composed of completely neutral and completely ionized hydrogen gas, while more recent works (Ciardi et al., 2003; Zahn et al., 2007a; Shin et al., 2008; Petkova & Springel, 2011b; Finlator et al., 2012) begin to consider the *degree of ionization*

within ionized gas. The simplification of considering a two phase medium helps reduce the simulation complexity and the language needed to describe the results. However, as simulations become more sophisticated, the two phase paradigm becomes ill-suited to convey the wealth of information contained in the larger and more detailed simulations. As people begin to describe the new simulations, the old paradigm lingers and causes ambiguities. As a case in point, consider the ionized volume filling fraction versus redshift, one of the simplest quantitative metrics of any reionization simulation. Within the framework of a two-phase medium, this is uniquely defined at any redshift. For a simulation such as ours which tracks the ionization state in every cell, the volume filling fraction depends on the degree of ionization, as illustrated in Figure 3.6.

This figure shows the evolution of the volume filling fraction of ionized gas which exceeds a minimum local ionization fraction $f_i \equiv \rho_{\rm H\,II}/\rho_{\rm H}$. The three thresholds are $f_i = 0.1$, 0.999, and 0.99999 and are labelled 10%, 1E3, 1E5, respectively in Figure 3.6. We choose three specific levels not because we think they are more important than others, but because it suits our later narrative and gives a range of values. With the ionization state tracked by the simulation, we see that it is now ambiguous to ask at what redshift 50% of the volume is ionized. In our simulation this occurs at $z \approx 7$, 6.8 and 6.5 for f_i=0.1, 0.999, and 0.99999, respectively.

In the rest of this paper we will often report results as a function of these three ionization fraction thresholds. To make the text easier to read we will use the terms "Ionized" to designate f_i=0.1, "Well Ionized" to designate f_i=0.999, and "Fully Ionized" to designate f_i=0.99999 ionization levels.

3.3.2 Inside-out or Outside-in

Besides specifying the amount of ionized volume and levels of ionization, another area where quantitative language is useful is in the description of the reionization history. Since the Outside-in model was proposed by Miralda-Escudé et al. (2000), there is gathering support for the opposing view of the Inside-out model by Sokasian et al. (2003); Furlanetto et al. (2004a); Iliev et al. (2006) to name a few. In Finlator et al. (2009b), the authors go even further and add to the

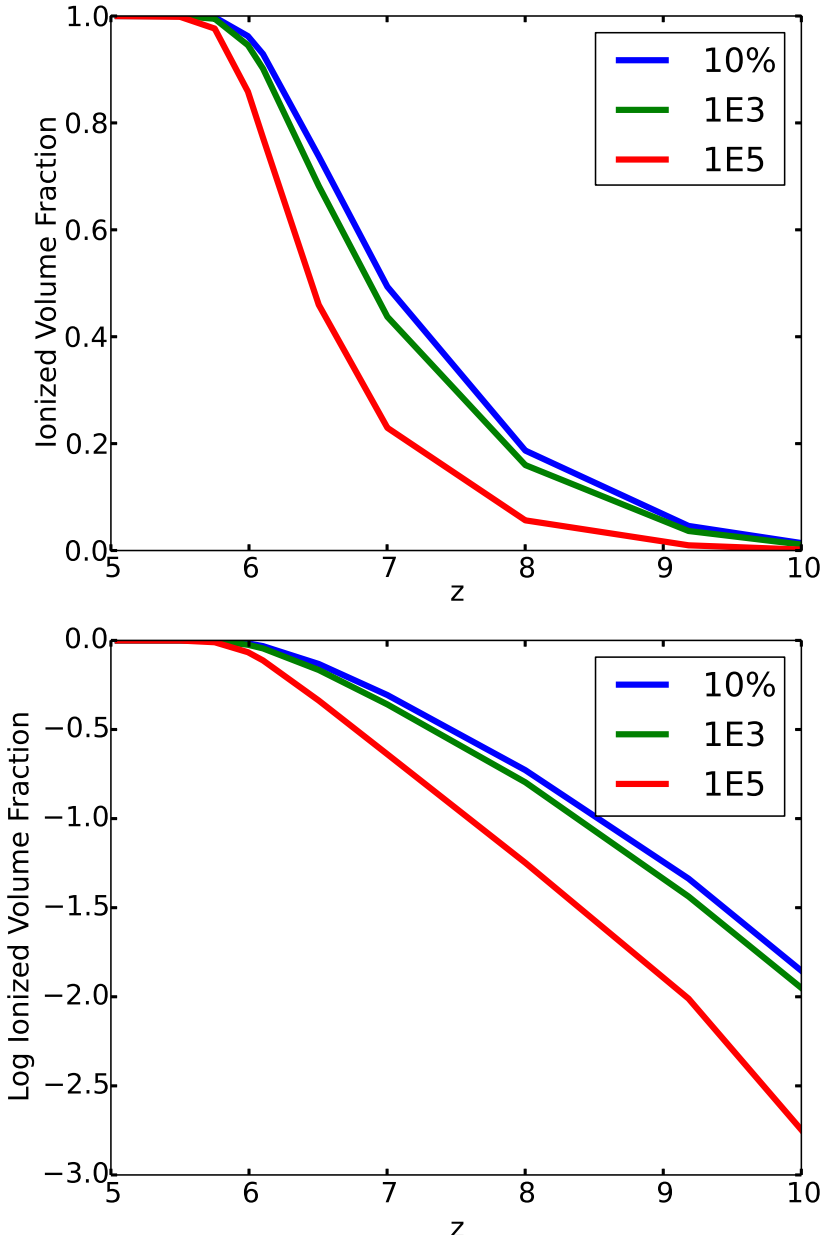

Figure 3.6: Volume filling fraction of ionized gas versus redshift for three ionized fraction thresholds. *Top* linscale; *Bottom* logscale. The three ionization levels are "10%" in blue: fractional volume that have more than 1 ionized hydrogen atom per 10 hydrogen atoms. "1E3" in green: fractional volume that have less than 1 neutral hydrogen atom per 10^3 hydrogen atoms. "1E5" in red: fractional volume that have less than 1 neutral hydrogen atom per 10^5 hydrogen atoms.

lexicon "Inside-outside-middle", trying to describe the rich detail in a reionization scenario. The basic Inside-out picture is that galaxies form in the peaks of the dark matter density field and drive expanding H II regions into their surroundings (*expansion phase*). These H II regions are initially isolated, but begin to merge into larger, Mpc-scale H II regions due to the clustering of the galaxy distribution (*percolation phase*). Driven by a steadily increasing global star formation rate and recombination time (due to cosmic expansion) this process goes on until H II regions completely fill the volume (*overlap phase*). In this picture, rare peaks in the density field ionize first while regions that of lower density ionize later from local sources that themselves formed later.

To investigate how reionization progresses in regions of different density, we plot in Figure 3.7 the hydrogen neutral fraction ($\rho_{\rm H\,I}/\rho_{\rm H}$) versus overdensity $\Delta_b \equiv \rho_b/\langle\rho_b\rangle$ in the left column, and in the right column a slice of the gas temperature, with redshift decreasing from top to bottom. One would expect if inside-out ionization is the case, that the neutral fraction of higher density regions should drop down more quickly than lower density regions. Below, we will describe each row of the figure in more detail.

Looking at the redshift $z = 10$ row, we see in the gas temperature slice that two isolated regions of ionization appear due to UV feedback from new stars, indicated by the $\sim 10^4$K gas . These regions correspond to places on the neutral fraction vs. overdensity phase plot where a small amount of volume emerges around Δ_b of $10^{-1} - 10^1$, reaching Well Ionized to Fully Ionized levels. The T $\sim 10^7$K region corresponds to the extended tail of very low neutral fraction gas in the left column, and indicates gas shock heated by supernova feedback. Although the cell count of shock heated gas will grow, it remains orders of magnitude smaller compared to the photoionized regions that we will emphasize. Even at this early stage, there are high density regions above Δ_b of 10^2-10^3 that are Well Ionized; this is due to their close proximity to the ionizing sources, supporting the Inside-out paradigm.

Looking at the next row of figures at a redshift of $z = 7$, we see that the volume of Well Ionized regions has increased greatly, and so has the shock heated region in the phase plot. We also see that most, but not all the $\Delta_b > 10^2$ cells

have reached the Well Ionized level. Although a large portion of the volume is in the Well Ionized regime, the majority of the volume (the red pixels) is still neutral, as we can see in the corresponding temperature slice plot. Most of the volume is still well under 10^4K, where we expect the temperature to hover once the ionization front has passed through the region and the gas has had time to come into photoionization thermal equilibrium.

By a redshift of $z = 6.1$, we see from the left column that the region that is ionized beyond the Fully Ionized level (an irony in terms, which means there is definitely room for improvement in the naming convention), dominates the simulation volume. There are still some regions not yet consumed by the ionization front, as is seen on the top of the neutral fraction plot and on the right according to the temperature slice.

The next row at redshift of $z = 5.5$ is after the entire volume has been swept over by ionization fronts. Most of the volume is beyond the Well Ionized level, except for a few cells around $\Delta_b \sim 10^2$. There are also some cells that are still neutral around $\Delta_b \sim 10^4$. They remain neutral because their densities are so high, leading to high recombination rates. Over time these cells will shift up and down the neutral fraction plot with waves of star formation and supernova explosions since they are likely close to the source of the radiation and kinetic energy.

The last row of Figure 3.7 is at redshift $z \sim 5$, where we can see that the previous few cells that have yet to reach Well Ionized levels around $\Delta_b \sim 10^2 - 10^3$ have now disappeared. The cells that have not reached Well Ionized level before are cells where either the radiation is not strong enough due to shielding effects or the density is so high the gas recombines quickly even after being ionized. After the ionization front has passed though and highly ionized the IGM, there is little material left to shield against the radiation background and we see all but the densest few cells become Well Ionized. The high density region reaching the same ionization level after the under dense void, would fit well with the description for the Outside-in model. Note that the remaining cells that finally reached Well Ionized levels are orders of magnitude smaller in total volume compared to the rest of the cells at the same density. So if we call cells of $\Delta_b \sim 10^2$ filaments, not all

dense filaments get Well Ionized until late in the EoR. Before the volume is filled with radiation, these dense filaments are able to remain relatively neutral.

Unfortunately, the evolution of these redshift panels is not enough to capture the propagation of radiation fronts from the initial sources, but they do convey the overall ionization history of the universe. The panels suggest that the regions surrounding the ionization sources, whether they are dense cores, filaments, or voids, are all affected by the radiation on roughly the same time scale. However, the degree to which they are ionized is different. It is this difference, that is the key to answering the original question, whether the universe ionizes inside-out or outside-in.

When focusing on the ionization of the IGM, we temporarily neglect the $\Delta_b \sim 10^4$ cells that shift ionization level with waves of star formation which comprise a tiny fraction of the volume. If we use the "Ionized" level to characterize something as completely ionized and draw the line for neutral fraction at 10%, then the universe reaches end of EoR before $z \sim 5.5$. Since radiation propagates from sources outward, that would correspond to the Inside-out picture. If we were to instead draw the completely ionized line at "Well Ionized" level, then we can see that even at $z \sim 5.5$, there is a small peak in the dense region of the phase diagram ($\Delta_b \sim 2.4 \times 10^2$) that has yet to reach below the line to be considered completely ionized. This would correspond to the Outside-in picture which reaches end of EoR sometime before $z \sim 5$ (or Inside-outside-middle if one uses the Finlator et al. (2009b) terminology and considers the neutral peak to be a part of the filaments). And finally, if we were to draw the line at the "Fully Ionized" level, the universe has yet to ionize even for regions that are only $10\times$ over dense. Thus the ionization history is a story with many perspectives, and it really depends on how the story teller draws the line as to whether Inside-out, Outside-in, or Inside-outside-middle is a better qualitative description.

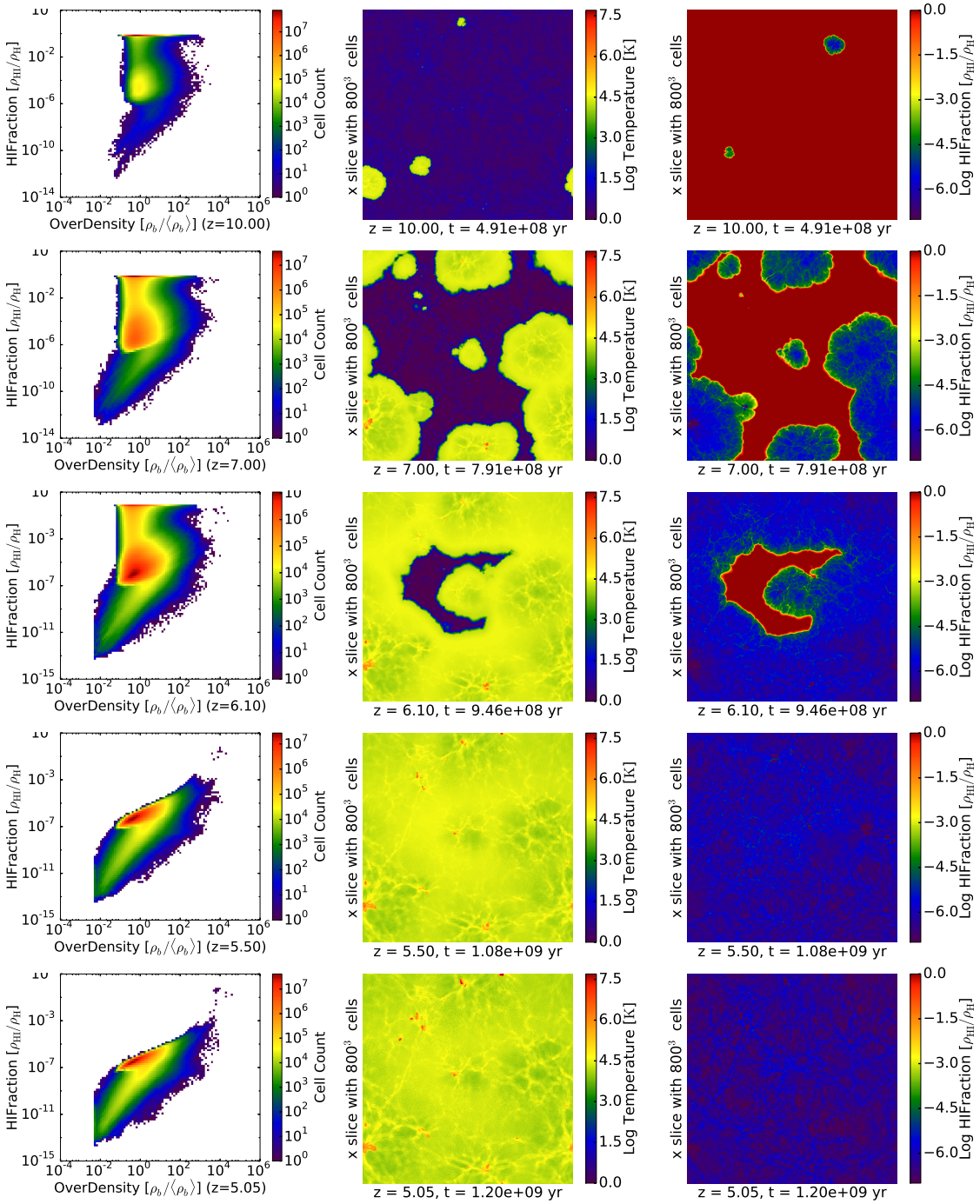

Figure 3.7: *Left*: Phase diagram of neutral hydrogen fraction versus baryon overdensity with decreasing redshift from top to bottom. *Middle*: Slices of Log Temperature [K] through a region that remained mostly neutral until just before overlap at redshift of ∼5.8. *Right*: Slices of neutral hydrogen fraction through the same region as before. Please refer to §3.3.2 for detailed description.

3.4 Clumping Factors and the Photon Budget for Reionization

3.4.1 Clumping Factor Analysis of Madau

In this section we begin our examination of Equation (3.1) from Madau et al. (1999) as an accurate predictor of when reionization completes, focusing on the clumping factor. While it is true that the Madau-type analysis was not designed to predict the precise redshift for reionization completion, only the ionization rate density needed to maintain the IGM in an ionized state after reionization has completed, it is effectively being used in this way when it is applied to galaxy populations at increasingly higher redshifts $z = 6 - 7$ (cf. Fan et al. (2006); Robertson et al. (2013)). Our methodology is the following. The simulation supplies $\dot{N}_{sim}(z)$ ionizing photons, which increases with decreasing redshift because the SFRD increases with decreasing redshift. Equation (3.1) poses a minimum requirement on the ionizing emissivity to maintain the IGM in an ionized state at given redshift z. This requirement decreases with decreasing redshift due to the strong z dependence. We look to see if the box becomes fully ionized when these two curves cross; i.e., when $\dot{N}_{sim} \geq \dot{\mathcal{N}}_{ion}$. In subsequent sections we do this for more recent definitions of the clumping factor that have been introduced by various authors, in roughly chronological order.

The way the clumping factor is introduced and used, is to estimate the amount of recombination that radiation has to overcome, in order to keep the universe ionized (Gnedin & Ostriker, 1997; Valageas & Silk, 1999; Madau et al., 1999; Fan et al., 2006). In a homogeneous universe, the hydrogen recombination rate is also homogeneous, and is a simple function of the mean density, ionization fraction, and temperature. The clumping factor is a correction factor to account for density inhomogeneities induced by structure formation, although in principle inhomogeneities in ionization fraction and temperature are also important. The most common definition for the clumping factor is:

$$C = \frac{\langle n_{\rm H\,II}^2 \rangle}{\langle n_{\rm H\,II} \rangle^2} \tag{3.16}$$

where the $\langle\rangle$ brackets denote an average over the simulation volume. To see where this comes from we can look at the change of $n_{\rm H\,II}$ with respect to time due to recombinations:

$$\begin{aligned}
\frac{\partial n_{\rm H\,II}}{\partial t} &= -n_{\rm e} n_{\rm H\,II} \alpha_B(T) \\
\frac{\partial n_{\rm H\,II}}{n_{\rm H\,II}} &= -\partial t n_{\rm e} \alpha_B(T) \\
\int_{n_i}^{n_f} \frac{\partial n_{\rm H\,II}}{n_{\rm H\,II}} &= -\int_{t_i}^{t_f} \partial t n_{\rm e} \alpha_B(T) \\
ln\left(\frac{n_f}{n_i}\right) &= -(t_f - t_i) n_{\rm e} \alpha_B(T), \\
\frac{n_f}{n_i} &= exp(-t_{rec} n_{\rm e} \alpha_B).
\end{aligned} \tag{3.17}$$

In the last step, we have set $(t_f - t_i)$ to be t_{rec}. This leads to

$$t_{rec} = [n_{\rm e} \alpha_B(T)]^{-1} \tag{3.18}$$

being the characteristic time when the fraction $n_f/n_i = 1/e$. Using this expression for the recombination time, one can rewrite the right hand side of the equation as

$$\begin{aligned}
\frac{\partial n_{\rm H\,II}}{\partial t} &= -n_{\rm H\,II} n_{\rm e} \alpha_B(T) = -n_{\rm H\,II}/t_{rec} \\
&= -n_{\rm H\,II}(1 + 2\chi) n_{\rm H\,II} \alpha_B(T) \\
&= -n_{\rm H\,II}^2 (1 + 2\chi) \alpha_B(T)
\end{aligned} \tag{3.19}$$

where in the last two steps, following Madau et al. (1999), we replace $n_{\rm e}$ with $(1 + 2\chi) n_{\rm H\,II}$ assuming helium is fully ionized. Here χ is the cosmic fraction of helium. Taking the volume average we have:

$$\begin{aligned}
\langle \frac{\partial n_{\rm H\,II}}{\partial t} \rangle &= -\langle n_{\rm H\,II}^2 (1 + 2\chi) \alpha_B(T) \rangle \\
&= -\langle n_{\rm H\,II}^2 \rangle (1 + 2\chi) \alpha_B \\
&= -\langle n_{\rm H\,II} \rangle^2 (1 + 2\chi) \alpha_B C \\
&= -\langle n_{\rm H\,II} \rangle / \bar{t}_{rec}.
\end{aligned} \tag{3.20}$$

In the above we have made the oft-used assumption of a uniform IGM temperature of 10^4K, making the Case B recombination coefficient α_B a constant. Note

this is not physically justified, but since the temperature of the IGM is not well determined observationally, it is a useful approximation, and one that is embedded in Equation (3.1). With this simplifying assumption, when taking the volume average on both sides of Equation (3.19), we may rewrite the result in the same form as the end of the first line in Equation (3.19), with a density term dividing by a time term. Therefore, the effective recombination time can be written as

$$\bar{t}_{rec} = t_{\rm Madau} \equiv [(1+2\chi)\langle n_{\rm H\,II}\rangle \alpha_B C]^{-1}. \tag{3.21}$$

This expression is the same as Equation (20) of Madau et al. (1999) if we substitute $\langle n_{\rm H\,II}\rangle$ for $\bar{n}_{\rm H}$. In the case of a fully ionized universe these two quantities are equivalent. We note that $t_{\rm Madau}$ is not at all the volume average of t_{rec} but is $\langle t_{rec}^{-1}\rangle^{-1} C^{-1}$, which weights regions with the *shortest* recombination times; i.e. regions at the mean density and above. If we now make the *ansatz* $\dot{\mathcal{N}}_{ion} \times \bar{t}_{rec} = \bar{n}_{\rm H}(0)$, we may derive Equation (26) in Madau et al. (1999), updated by Fan et al. (2006), repeated here for convenience:

$$\dot{\mathcal{N}}(z) = 10^{51.2} s^{-1} Mpc^{-3} \left(\frac{C}{30}\right) \left(\frac{\Omega_{\rm b} h^2}{0.02}\right)^2 \left(\frac{1+z}{6}\right)^3. \tag{3.22}$$

This equation gives an estimate of the ionizing photon production rate density (in units of $\rm s^{-1}Mpc^{-3}$comoving) that is needed to balance the recombination rate density (the right-hand-side of Equation (3.22)) in a completely ionized universe. Values for C ranging ∼10-30 are often quoted from earlier hydrodynamical simulations such as Gnedin & Ostriker (1997), and ~ 3 for more recent work following Pawlik et al. (2009); Raicevic & Theuns (2011); Shull et al. (2012); Finlator et al. (2012) and the methods there.

We follow these earlier studies using our own simulation data. In Figure 3.8 we plot the ionizing photon production rate density and recombination rate density from our fiducial simulation. The curve in blue labeled $\dot{N}_{sim}$ is the photon production rate density from the simulation, calculated using a time average of the volume integrated ionizing emissivity η (Equation (3.15)) divided by the average energy per photon which we obtain directly from the SED. The other three curves plot Equation (3.22) for three methods for calculating C: green uses the H II density directly (Equation (3.16)); red uses the baryon density $C = \langle \rho_b^2\rangle / \langle \rho_b\rangle^2$; and

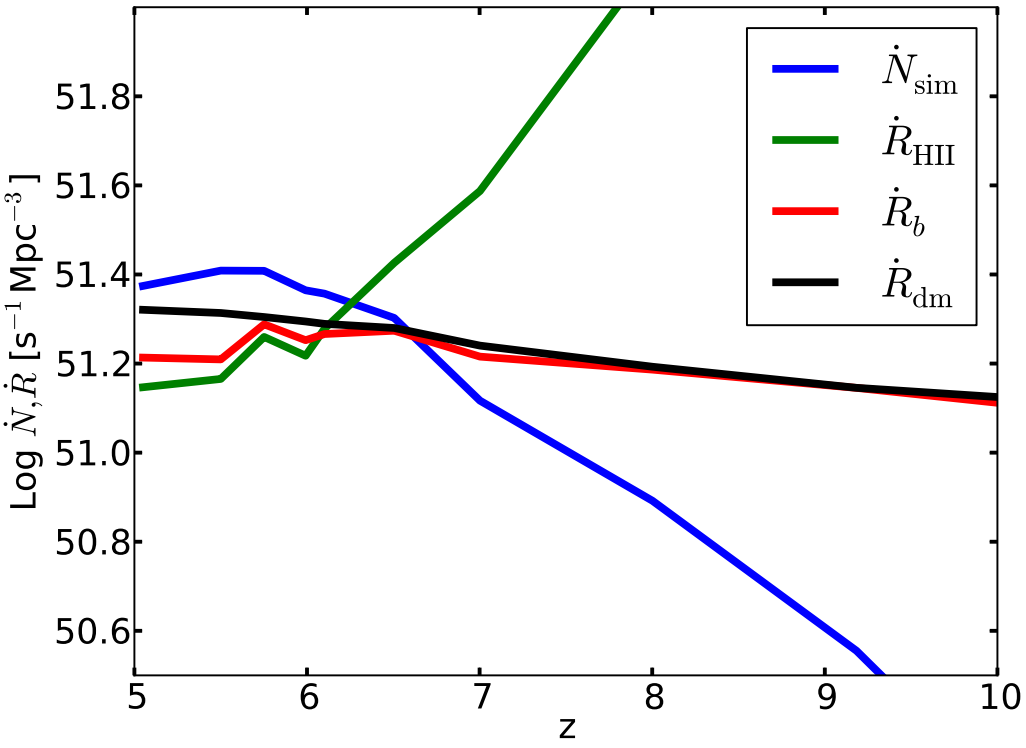

Figure 3.8: Ionizing photon production rate density and various estimates of the recombination rate density versus redshift. The blue curve labeled "$\dot{N}_{sim}$" is the measured photon production rate density averaged over the entire simulation volume. The green curve labeled "$\dot{R}_{\rm H\,II}$" is the recombination rate density estimate from using the clumping factor calculated with Equation (3.16) substituted in Equation (3.22). The red curve labeled "$\dot{R}_b$" is Equation (3.22) evaluated using a clumping factor calculated from the baryon density. The black curve labeled "$\dot{R}_{\rm dm}$" is using a clumping factor calculated with dark matter density.

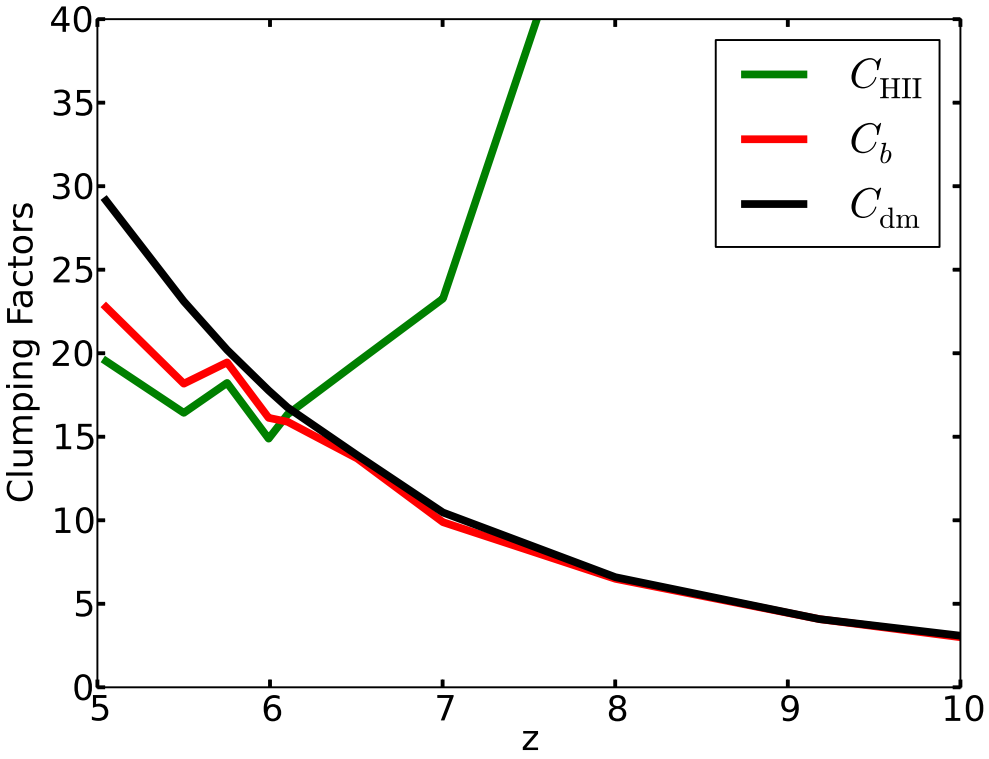

Figure 3.9: Unthresholded clumping factors used in Fig. 3.8. C_{HII}, C_b, C_{dm} are calculated from the unthresholded H II, baryon, and dark matter densities, respectively.

black uses the dark matter density $C = \langle \rho_{dm}^2 \rangle / \langle \rho_{dm} \rangle^2$. In all cases no thresholding is being applied (the effect of thresholding is examined in the next section); the averages are done over every cell in the simulation including those inside the virial radii of galaxies. The H II curve drops sharply with decreasing redshift because C is large when the H II distribution is patchy. The baryon and dark matter curves track one another for $z > 6$ because the clumping factors are nearly the same, but begin to separate after overlap as the baryon clumping factor drops due to Jeans smoothing.

Where the ionization and recombination rate density lines cross is roughly when we expect the universe to become highly ionized. If we define the end of the EoR as when 99.9% of the volume has reached the Well Ionized level, then our simulation reaches that point around $z \sim 5.8$ according to Figure 3.6. The $\dot{N}_{sim}$ curve crosses the $\dot{R}_{\rm H\,II}$ curve at $z \sim 6.2$. This is somewhat reassuring since we are counting every ionizing photon emitted and every recombination, at lease insofar as Equation (3.22) provides a good estimate of that. The recombination rate density curves using clumping factors computed from the baryon and dark matter densities curves cross the $\dot{N}_{sim}$ curve at a somewhat higher redshift of $z \approx 6.6$. By following the original methodology of using the clumping factor to estimate recombinations, we find that the clumping factor calculated with the H II density field to be the closest predictor for the end of EoR in our simulation.

The photon budget that enabled us to reach different levels of ionization is plotted in Figure 3.10. Here we plot the evolution of the ionized volume fraction versus $\gamma_{ion}/H = \int dt \dot{N}_{sim}/\bar{n}_{\rm H}(0)$. So, for the same definition for the end of EoR, we see that we need $\sim$4 photons per hydrogen atom to ionize the universe. This cannot be considered a converged result because this estimate includes the dense gas inside galaxies, which is not well resolved in our simulation. Even though a small fraction of the baryons reside inside galaxies, due to the short recombination time many ionizing photons are required to keep the gas ionized. Since we have not resolved the internal structure of galaxies, and higher resolution would likely result in higher density gas, we must consider $\gamma_{ion}/H = 4$ a lower bound. We eliminate this issue in the next subsection by excluding the dense gas in halos from

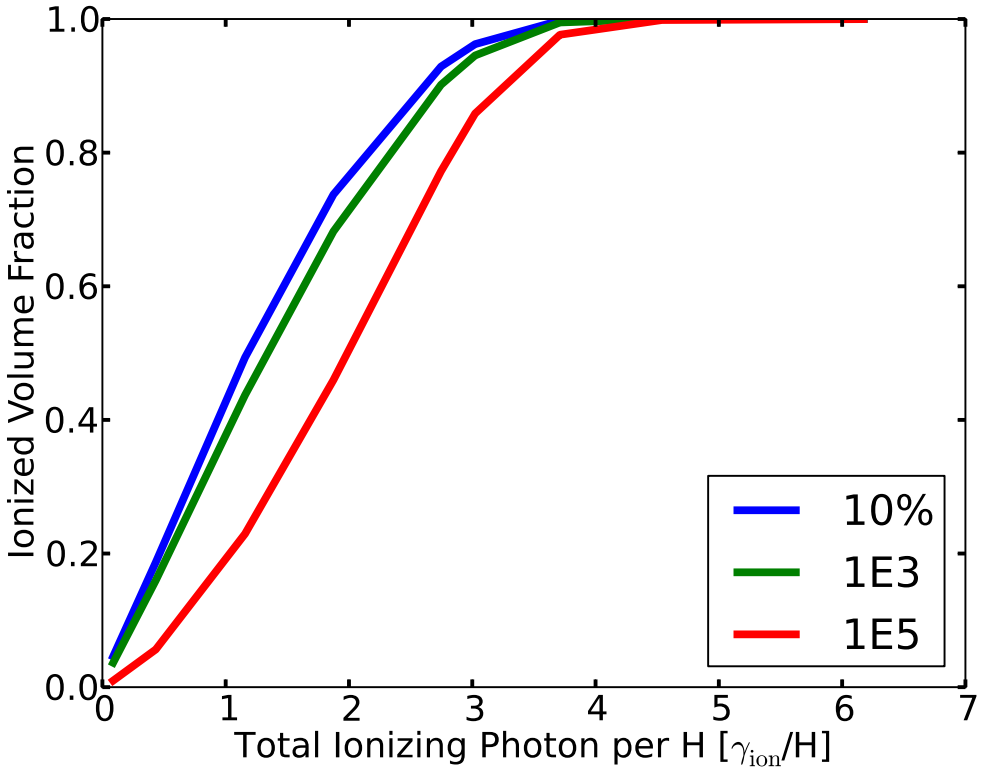

Figure 3.10: Ionized volume fraction as a function of the number of ionizing photons emitted per H atom averaged over the entire simulation volume (including inside halos) for three different ionization levels: $f_i \geq 0.1$ (blue line); $f_i \geq 0.999$ (green line); $f_i \geq 0.99999$ (red line). Compare with Fig. 3.14 which excludes gas inside halos.

the calculation.

3.4.2 Quantitative Analysis of Recombinations

As the clumping factor method grew in popularity, various authors have applied thresholds of one form or another to improve upon its accuracy in predicting the recombination rate density needed to maintain an ionized universe. When thresholds are applied, parts of the volume are excluded from the photon counting analysis. Pawlik et al. (2009); Raicevic & Theuns (2011) and others, limit the calculation of the clumping factor to the low density IGM by using Δ_b

thresholds, usually set at 100. They threshold out gas in virialized halos and the self-shielded collapsed objects, because radiation does not penetrate these objects, or they recombine too fast, which leaves them neutral and not contributing to recombinations in the IGM. More recently Shull et al. (2012) has also thresholded out void regions ($\Delta_b < 1$), arguing that they do not contribute appreciably to the total recombinations due to their long recombination times.

To investigate the contribution of gas of different density to the total recombination rate density, we plot in Figure 3.11, three quantities dealing with recombinations in our simulation. In the left column we have a 2D distribution plot of recombination rate density $\dot{R} = n_{\rm H\,II} n_e \alpha_B(T)$ divided by ionization rate density $\Gamma^{ph}_{\rm H\,I} n_{\rm H\,I}$ versus baryon overdensity Δ_b, where

$$\Gamma^{ph}_{\rm H\,I} = \frac{cE}{h} \left[\int_{\nu_{\rm H\,I}}^{\infty} \frac{\sigma_{\rm H\,I}(\nu)\chi_E(\nu)}{\nu}\,{\rm d}\nu \right] \Bigg/ \left[\int_{\nu_{\rm H\,I}}^{\infty} \chi_E(\nu)\,{\rm d}\nu \right]. \tag{3.23}$$

Here, $\sigma_{\rm H\,I}(\nu)$ and $\nu_{\rm H\,I}$ are the ionization cross section and ionization threshold for H I, respectively, and h is Planck's constant (Paper I). In the middle column we plot the relative bin contribution to the total recombination rate density versus Δ_b. We draw vertical lines at Δ_b=1 and 100, and in the legend box calculate the cumulative contribution to total reionizations to those thresholds. In the right column, we plot the cell recombination time divided by the Hubble time versus Δ_b. All three columns evolve with decreasing redshift from top to bottom.

At $z \sim 9$, in the left column of Figure 3.11, we see that even though there are regions of the volume that are in approximate ionization equilibrium (indicated by the horizontal distribution near 10^0), there is a wide distribution of cells far out of equilibrium, some even off by ~ 120 orders of magnitude. The middle column shows that about 37% of all recombinations happen below a Δ_b of 100, and about 3.2% happen below Δ_b of 1. The phase diagram in the right column shows that there is a bimodal distribution of cells in terms of their recombination time normalized by Hubble time. The top concentration of cells are more neutral, having long recombination times, and the lower concentration of cells are photoionized, having smaller recombination times. The recombination time is lower for the ionized cells simply because there are more free electrons available to recombine with protons. The blue cluster of points at low Δ_b and high $t_{rec}/t_{\rm Hubble}$ are the small number of

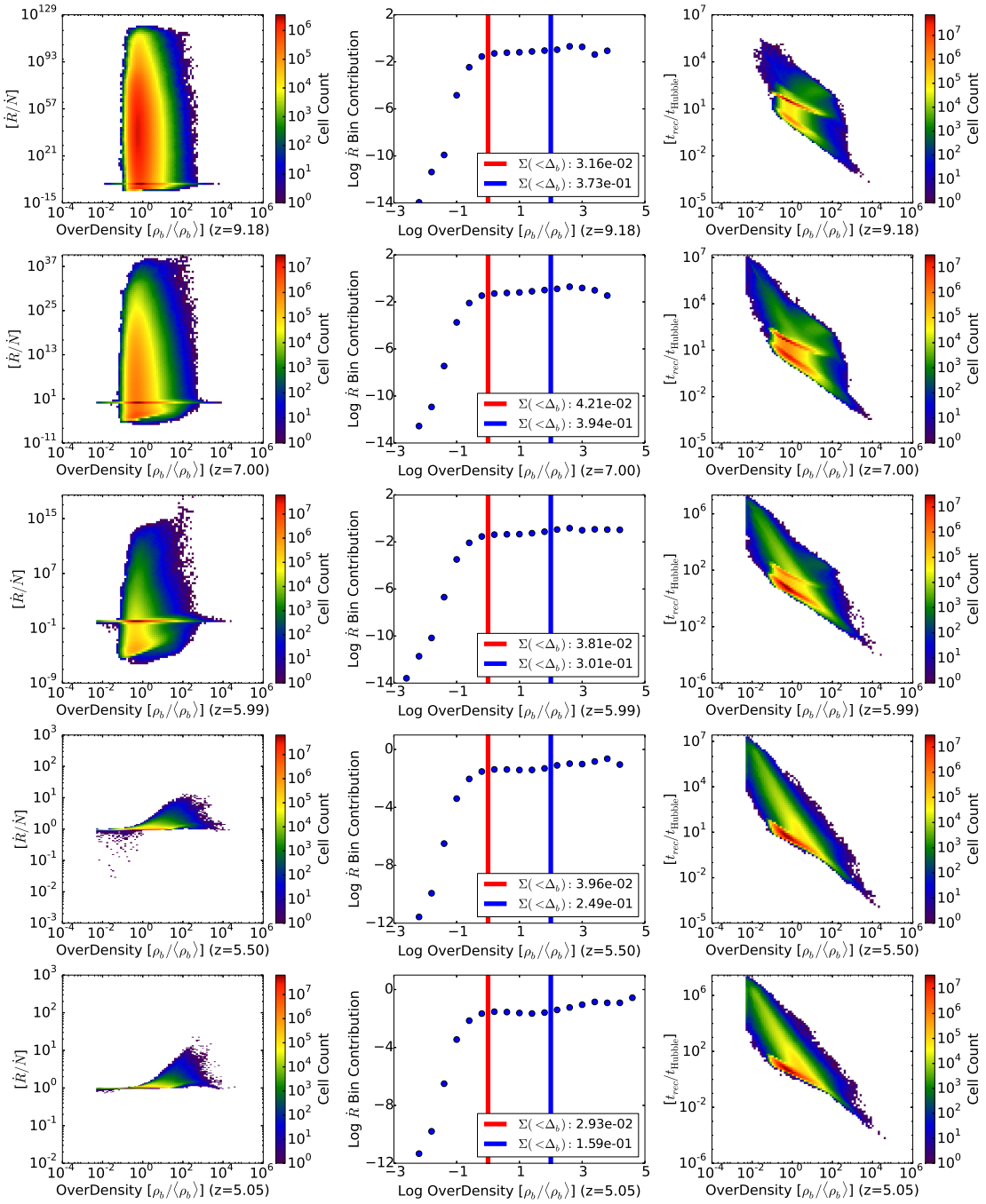

Figure 3.11: Quantifying recombination information. Left column is a 2D distribution of recombination rate density divided by ionization rate density versus overdensity. Middle column is a plot of the relative bin contribution to the total recombination rate density versus overdensity bins. The lines show the sum of all previous bins. Blue line is at Δ_b=100, red line is at Δ_b=1. Right column is plot of recombination time divide by Hubble time versus overdensity.

cells that are shock heated to $T > 10^6$K by supernova feedback. Due to this high temperature, even though there are more free electrons their recombination times remain long.

At $z \sim 7$, more of the volume has reached the Well Ionized level, and we see the size of the out of equilibrium distribution shrink in the left column. Now the maximum is only ~ 37 orders of magnitude higher compared to equilibrium. The middle column shows that about 40% of total recombinations are happening below Δ_b of 100, and about 4.2% happens below Δ_b of 1. In the right column, we see roughly equal numbers of cells in the upper (more neutral) distribution as compared to the lower (more ionized) distribution, whereas the top was much greater in numbers before. As more cells become ionized to a high degree, their recombination time will decrease and their cell counts will shift to the lower distribution.

At $z \sim 6$, looking at the left column, most of the cells are now in equilibrium. This is indicated by the peak of the distribution in red, being near zero on the y-axis. The maximum of the distribution is now less than 19 orders of magnitude apart from equilibrium. The middle column shows 30% to 3.8% recombinations below Δ_b of 100 and 1, respectively. The right column shows that the majority of the cells are now in the more ionized distribution and have a low recombination time. This can be verified by looking at the same redshift in Figure 3.7, where most of the cells are at the Well Ionized level compared to fewer before.

At $z \sim 5.5$, after the entire volume has become Well Ionized, the vertical spread of the distribution has collapsed to about an order of magnitude away from equilibrium with the vast majority of the cells in equilibrium. The fraction of recombinations are 25% and 4% below Δ_b of 100 and 1, respectively. Looking at the recombination time to Hubble time ratio, we no longer see the bimodal distribution of neutral cells and highly ionized cells, we only see the bottom distribution of highly ionized cells now. The small distribution of shock heated gas is still present, but now seems more prominent with the absence of the neutral distribution.

At $z \sim 5$, on the left column, the few cells that are in the low density void which were recombining slower than ionizing are now all near equilibrium. Cells that are higher in Δ_b are more likely to be above equilibrium. In the middle

column, we see that the fraction of recombinations are 16% and 2.9% for regions below Δ_b of 100 and 1, respectively. Not much has changed in the recombination time column except that there are fewer cells above the Δ_b of 10^4, possibly due to the effect of Jeans smoothing.

We see that there is no real one-to-one correspondence between overdensity and the quantities we show on the y-axis. That is because in a given panel, we are only seeing two dimensions of a multidimensional physical process that depends on proximity to sources of radiation, the behavior of said sources at a given moment, the local density of neutral and ionized gas, temperature, among others. It is helpful to speak about the average behavior in any given overdensity as we have done, but we should always keep in mind that the average may not be as representative of the wider distribution as we may think.

3.4.3 Investigating Thresholded Clumping Factor Analyses

Excluding Halos

We saw in §3.4.1 that using the unthresholded H II density field to calculate C via Equation (3.16) yields a reasonably good estimate of when reionization completes (Figure 3.8). This is perhaps not surprising since we count every ionizing photon emitted and every recombination to the accuracy of Equation (3.22). Possible sources of disagreement between theory and simulation are: (1) inaccuracies in estimating the recombination rate density using Equation (3.22); (2) breakdown of the "instantaneous approximation" used to derive Equation (3.22) due to history-dependent effects; (3) finite propagation time for I-fronts to cross voids; and (4) numerical inaccuracies. Regarding possibility (4) we note that our mathematical formalism is photon conserving, and that our I-front tests in Paper I show that I-fronts propagate at the correct speed, which is an indication that numerical photon conservation is good.

To investigate whether improved estimates of the recombination rate density will improve the agreement, we follow the practice of some recent investigators (Pawlik et al., 2009; Raicevic & Theuns, 2011) and threshold out dense gas bound to halos, leaving only the diffuse IGM to consider. The motivation for this is that

since we are only interested in the photon budget required to maintain the diffuse IGM in an ionized state, by excluding the complicated astrophysics within halos we have a simpler problem to model and resolve numerically.

To proceed we must calculate the ionization and recombination rate densities outside of collapsed objects. We estimate the number of ionizing photons escaping halos by multiplying $\dot{N}_{sim}(z)$ by a global escape fraction $\bar{f}_{esc}(z)$ derived in §3.5 and plotted in Figure 3.21:

$$\dot{N}_{IGM}(z) = \bar{f}_{esc}(z)\dot{N}_{sim}(z). \tag{3.24}$$

The recombination rate density outside of halos is calculated using Equation (3.22) where now the clumping factor is thresholded such that only cells for which $\Delta_b < 100$ contribute to the sum. As in Figure 3.8 we plot three curves for the recombination rate density calculated using Equation (3.22) using H II, baryons, and dark matter density fields. These are plotted in Figure 3.12 as green, red, and black curves, respectively. We see that the recombination rate density based on the singly thresholded H II (labeled $\dot{R}_{\mathrm{tH\,II}}$) and on the thresholded dark matter (labeled $\dot{R}_{\mathrm{tdm}}$) curve cross the ionizing emissivity curve labeled "$\dot{N}_{\mathrm{IGM}}$" at $z \approx 6.7$ in Figure 3.12, whereas the thresholded baryon density curve (labeled $\dot{R}_{tb}$) crosses "$\dot{N}_{\mathrm{IGM}}$" at $z \sim 7.2$. Taking the doubly-thresholded H II curve as the best estimate for the recombination rate density, we find that restricting the analysis to only IGM gas yields poorer agreement than the simpler, global model of Madau, which at first blush is a perplexing result. By thresholding out the gas in galaxies we have isolated the thing we care about: the ionization balance of the IGM. Why then should the implied redshift of reionization completion become worse compared to the analysis in §3.4.1? We defer addressing this question until later sections.

Finally, we ask how many ionizing photons per H atom are required to convert the neutral gas residing outside halos to a Well Ionized state. We repeat the analysis of Figure 3.10 and show the result in Figure 3.14. We see that the effect of counting only escaped photons on the photon budget is significant. Previously, we summed $\dot{N}_{sim}(z)$ and divided by the total number of hydrogen atoms in the simulation volume, and used that as our progress variable. In Figure 3.14 we sum $\dot{N}_{IGM}(z)$ and divide by the number of hydrogen atoms in the thresholded volume,

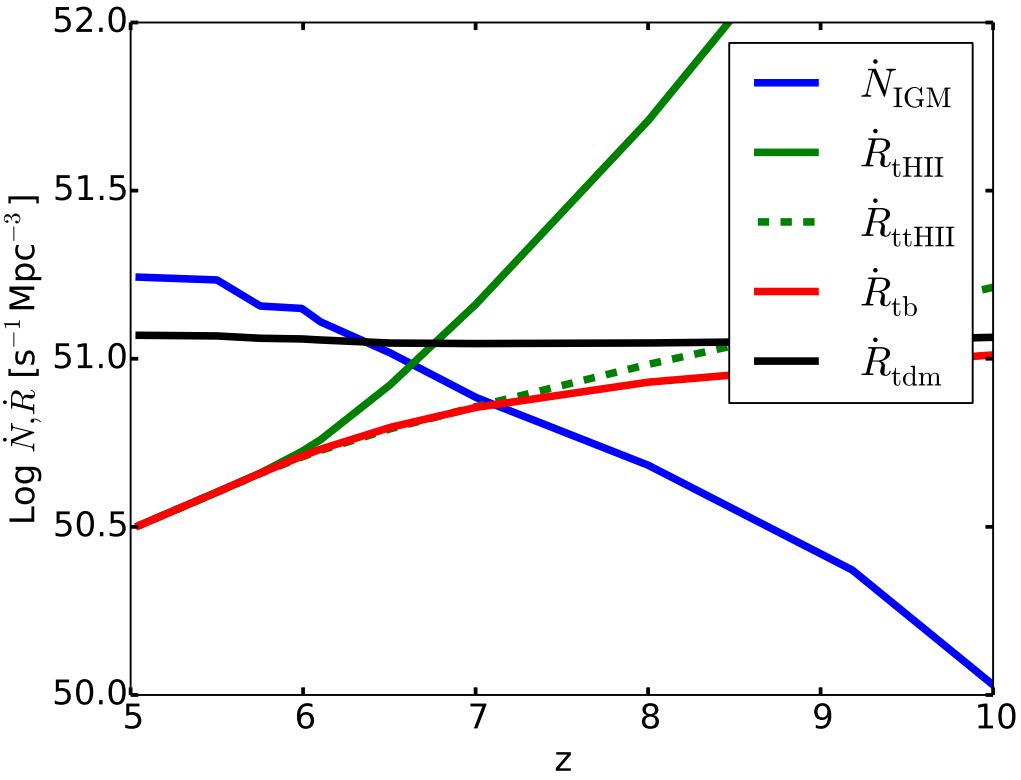

Figure 3.12: Same quantities as Figure 3.8, except now the "$\dot{N}_{\rm IGM}$" curve is the number of ionizing photons which escape into the IGM (see §3.5). The recombination rate densities with a subscript that begins with "t" are calculated as described in the caption for Figure 3.8, except that the clumping factors are computed excluding regions satisfying $\Delta_b > 100$. The curve labelled $\dot{R}_{ttHII}$ is calculated from Equation (22) using the doubly-thresholded clumping factor C_{ttHII} defined in Figure 3.13.

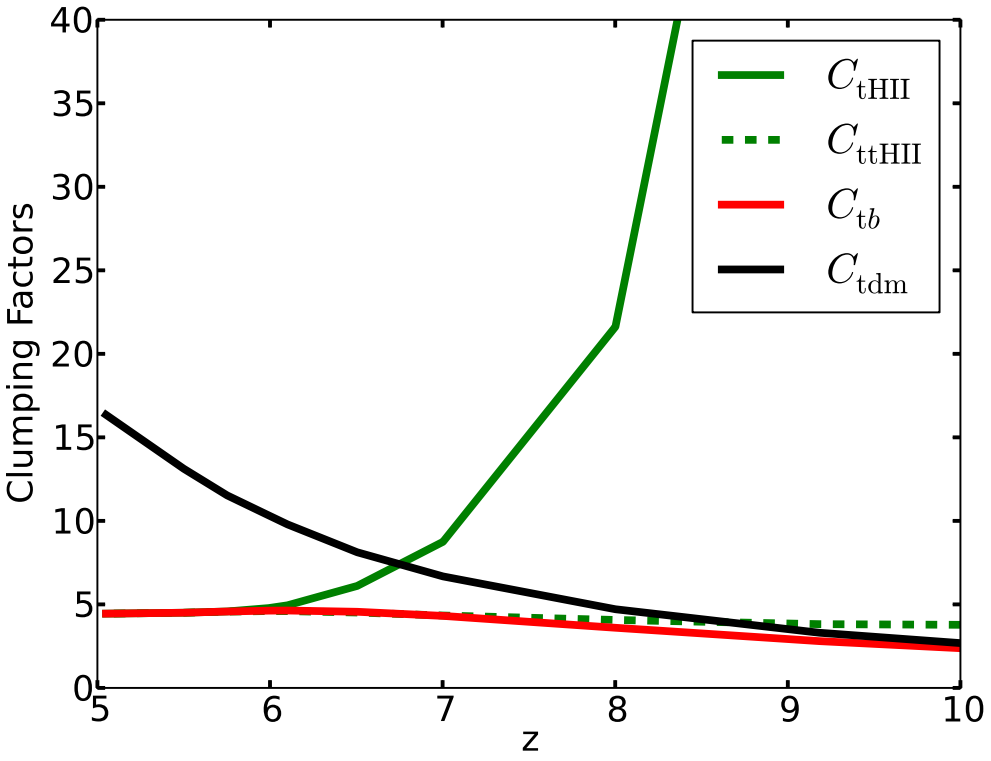

Figure 3.13: Thresholded clumping factors used in Fig. 3.12. $C_{tHII}, C_{tb}, C_{tdm}$ are calculated using thresholded H II, baryon, and dark matter density fields, respectively, where only cells satisfying $\Delta_b < 100$ contribute. C_{ttHII} is calculated from the H II density where only cells satisfying $\Delta_b < 100$ and $f_i > 0.1$ contribute.

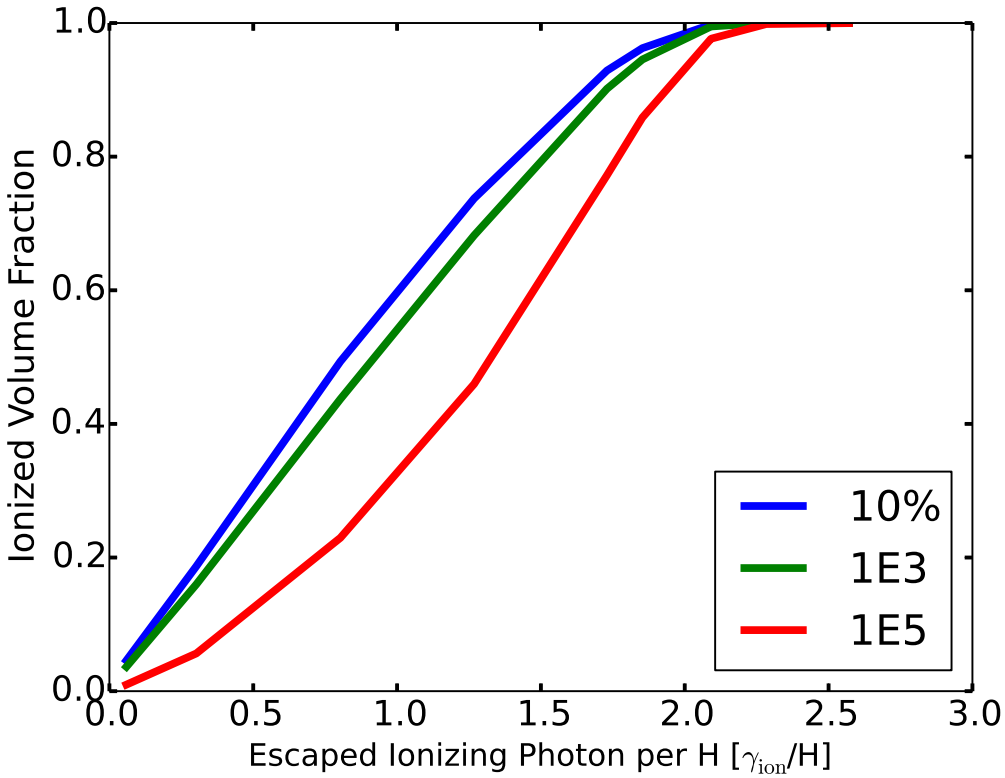

Figure 3.14: Ionized volume fraction as a function of the number of ionizing photons emitted per H atom averaged over the entire simulation volume (excluding gas inside halos) for three different ionization levels: $f_i \geq 0.1$ (blue line); $f_i \geq 0.999$ (green line); $f_i \geq 0.99999$ (red line). Compare with Fig. 3.10 which includes gas inside halos.

and use that as our progress variable. Instead of needing ∼4 to ionize the IGM, now we only need ∼2 photons per hydrogen atom for 99.9% of the universe to reach Well Ionized level. This result supports the "photon starved" reionization scenario discussed by Bolton & Haehnelt (2007).

Including Temperature Corrections

During the preparation of this paper, a new way of estimating the recombinations in the IGM appeared in the literature. The authors (Shull et al., 2012; Finlator et al., 2012) reformulated the expression for the clumping factor taking

the temperature dependence of the recombination rate into account. We briefly investigate their methods here. In order for the calculation of the clumping factor to take into account only IGM gas that is ionized but recombining, several additional thresholds were applied. Equation (15) in Shull et al. (2012) is a new expression for the clumping factor, similar in form to Gnedin (2000a),

$$C_{\rm RR} = \frac{\langle n_e n_{\rm H\,II} \alpha_B(T) \rangle}{\langle n_e \rangle \langle n_{\rm H\,II} \rangle \langle \alpha_B(T) \rangle} \tag{3.25}$$

with the following thresholds applied: $1 < \Delta_b < 100$, $300{\rm K} < T < 10^5{\rm K}$, ${\rm Z} < 10^{-6}{\rm Z}_\odot$, $x_e > 0.05$. Here, Z is metalicity and x_e is the ionized fraction. The reason that a lower limit threshold is applied to the baryon overdensity, the authors argued, is because very little recombinations happen there, due to the low density. Shull et al. (2012) also provide a new formulation for ionizing photon rate density that uses this definition of the clumping factor, in their Equation (10),

$$\frac{dN}{dt} = 4.6 \times 10^{50} {\rm s}^{-1} {\rm Mpc}^{-3} \times \left(\frac{(1+z)}{8} \right)^3 T_4^{-0.845} \left(\frac{C}{3} \right). \tag{3.26}$$

Here, $\rm T_4$ is mean IGM temperature measured in units of 10^4K.

Equation (3.26) is proposed as an improvement over Equation (3.1). To see if this is the case we used our data to evaluate the clumping factor $\rm C_{RR}$ and then used Equation (3.26) to calculate ionizing photon rate density versus redshift needed to maintain an ionized IGM. The result is shown in Figure 3.15. The curve labeled $\dot{R}_{\rm RR,T4}$ in green uses the average temperature, in units of 10^4K, of the region that satisfies the $\rm C_{RR}$ thresholds for $\rm T_4$ in Equation (3.26). The curve $\dot{R}_{\rm RR}$ uses 1 in place of $\rm T_4$ in Equation (3.26), essentially fixing the IGM temperature to a constant 10^4K. The green curve is lower than the red curve because the average temperature in the simulation is higher than 10^4K. The blue curve labeled $\dot{N}_{IGM}$ is as defined previously. We see that Equation (3.26) predicts that reionization completes at significantly higher redshifts than exhibited by the simulation, calling into question the validity of the analysis.

We find it curious that as the clumping factor analysis is refined through physically well-motivated modifications, it yields predictions for the redshift of

reionization completion that become worse and worse, moving to higher redshift rather than lower redshift. This suggests that there is something fundamentally wrong with the whole approach, and that the seemingly good agreement found in §3.4.1 was fortuitous. One worrisome aspect about the utility of Equation (3.26) is that the fraction of simulation volume included in the C_{RR} thresholds is actually quite small. This is illustrated in Figure 3.16. The included volume grows from 3% at $z = 9$ to only 23% of the simulation volume by overlap. One wonders about the validity of making global statements about reionization based on such a restricted sample of the IGM. It is also unclear how we should interpret the redshift at which lines across in Figure 3.15. Should we interpret it as the redshift below which an ionization rate given by Equation (3.26) can keep the whole volume ionized, or only the fraction of the volume satisfying the thresholds? If it is the former, how do we account for the time it takes for I-fronts to cross neutral voids?

At this point the reader may rightfully claim that the Madau-type analysis was never meant to predict the precise redshift for reionization completion, only the ionization rate density needed to maintain the IGM in an ionized state after reionization has completed. We would agree with that. However it is effectively being used in this way when it is applied to galaxy populations at increasingly higher redshifts $z = 6 - 7$ (cf. Fan et al. (2006); Robertson et al. (2013)). Our investigations indicate that formulae such as Equation (3.1) and (3.26) are not reliable estimates of when reionization completes. In §3.7 we examine whether they can be usefully applied at lower redshifts, as originally intended.

3.4.4 Comparing Clumping Factors

For ease of comparison we collect into one plot all the H II clumping factors used in the previous sections. The unthresholded H II calculated using Equation (3.16) is denoted $C_{\mathrm{H\,II}}$. The singly thresholded clumping factor is denoted $C_{\mathrm{tH\,II}}$, in which the threshold $\Delta_b < 100$ is being applied. The curve labeled C_{RR} plots the evolution of Equation (3.25) with the following thresholds: $1 < \Delta_b < 100$, $300\mathrm{K} < T < 10^5\mathrm{K}$, $x_e > 0.05$. For comparison we also plot a doubly thresholded H II clumping factor denoted $C_{\mathrm{ttH\,II}}$ with thresholds $\Delta_b < 100$ and $x_e > 0.05$, which can be

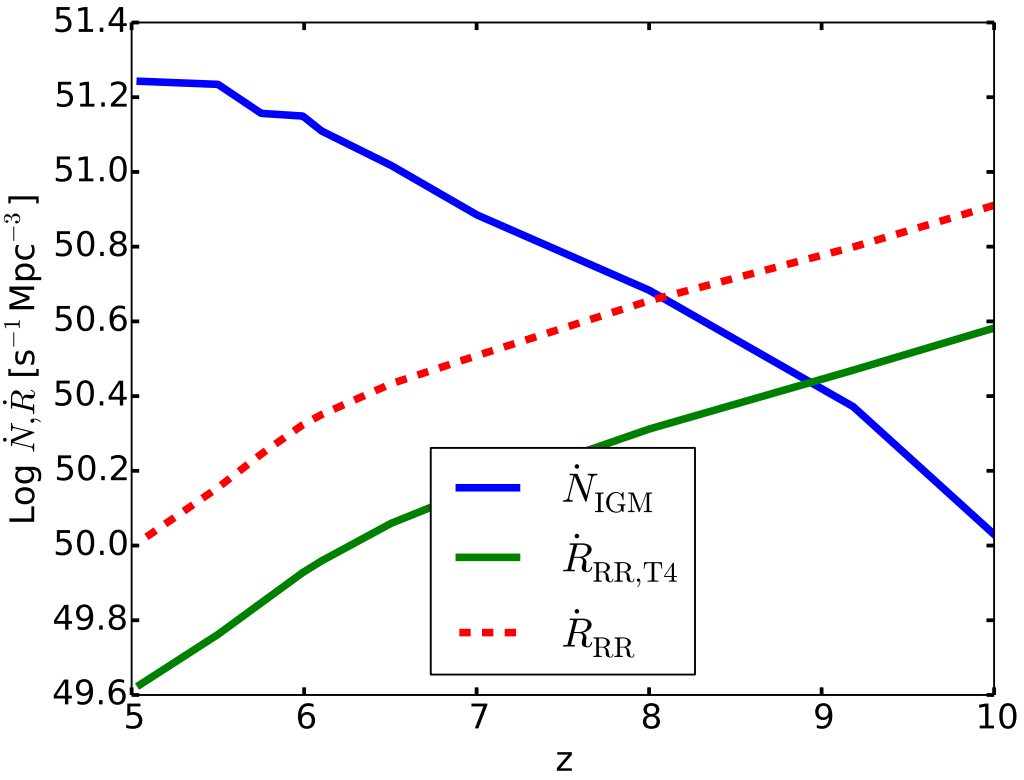

Figure 3.15: Ionizing photon injection rate density in the IGM from the simulation $\dot{N}_{IGM}$ versus the predictions of Equation (3.26), evaluated with two choices for the clumping factor which take temperature corrections into account. The curve labeled "$\dot{R}_{\rm RR,T4}$" is from Equation (3.26), with T_4 being the average temperature in $C_{\rm RR}$ region in units of 10^4K. The curve "$\dot{R}_{\rm RR}$" is calculated the same way as $\dot{R}_{\rm RR,T4}$ except now T_4 is set to 1 in Equation (3.26), for an effective IGM temperature of 10^4K.

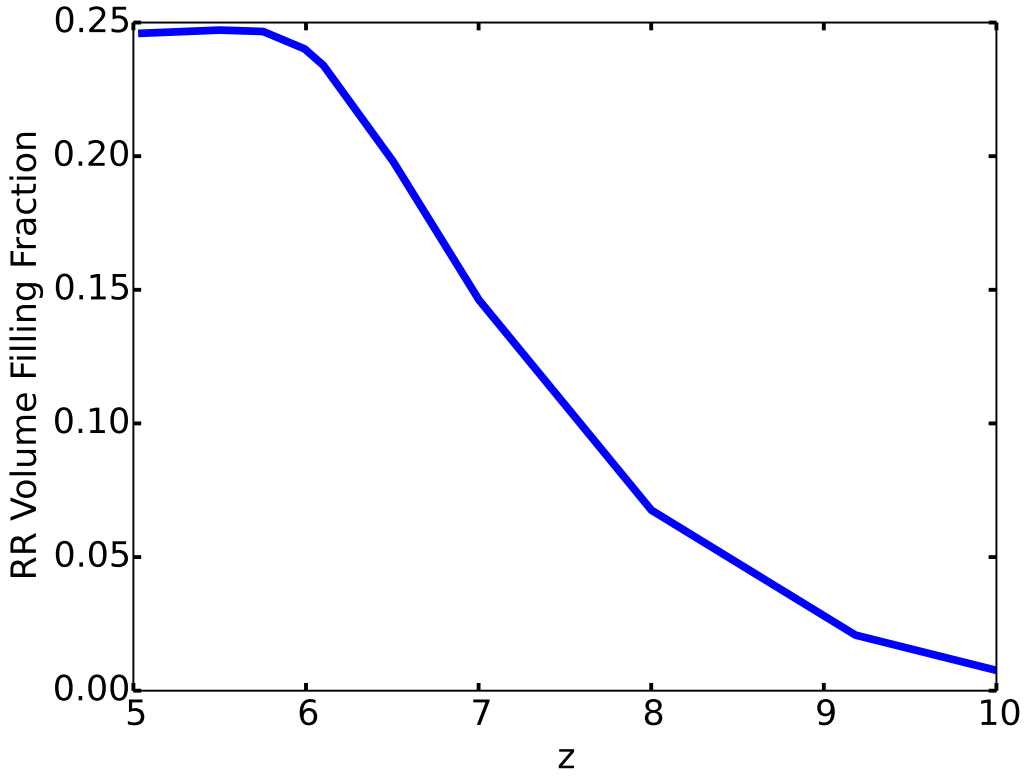

Figure 3.16: Evolution of the volume filling fraction with redshift of regions satisfying the C_{RR} thresholding criteria.

thought of as the clumping factor inside H II regions excluding the dense gas in halos.

We see a clear trend that as more thresholds are applied the lower the value of the clumping factor goes. This is because as more regions of the volume are excluded from the averaging process the remaining regions are more homogeneous exhibiting less variations. If no thresholds are applied, the H II clumping factor starts around 200 at $z \sim 9$ (Figure 3.8). Such high values arise because when the first couple of ionizing sources created high H II, they are localized and spread far apart, making the H II density very clumpy. As more of the universe is ionized, the H II density becomes more homogeneous. We see the single and double thresholded H II clumping factors become the same after overlap with a value of ~ 4.5 because the second threshold $x_e > 0.05$ is satisfied everywhere.

The clumping factor that is not based on the H II density alone is C_{RR}. We see from Equation (3.25) that C_{RR} depends on electron number density, H II number density, and the case B hydrogen recombination coefficient $\alpha_B(T)$, which is itself dependent on the gas temperature T (fit to Table 2.7 in Osterbrock & Ferland (2006) implemented in Enzo). $\alpha_B(T)$ depends on T to a negative power and this causes Equation (3.25) to sometimes have a very low numerator compared to the denominator. This as well as the exclusion of gas in the voids leads to the low clumping factor value of ~ 2 we see in the graph. It is very possible to have a value that is smaller than unity, which can lead to even more confusion with the original definition of the clumping factor in Equation (3.16). There, the clumping factor can only have a value of greater than 1, and 1 occurs only for the homogeneous distribution of the gas number density case.

3.5 A Global Estimate for Circumgalactic Absorption of Ionizing Radiation

The ionizing escape fraction from galaxies is an important parameter in models of reionization. Typically, one thinks about the escape fraction as a property of individual galaxies, determined by the absorption of ionizing radiation on

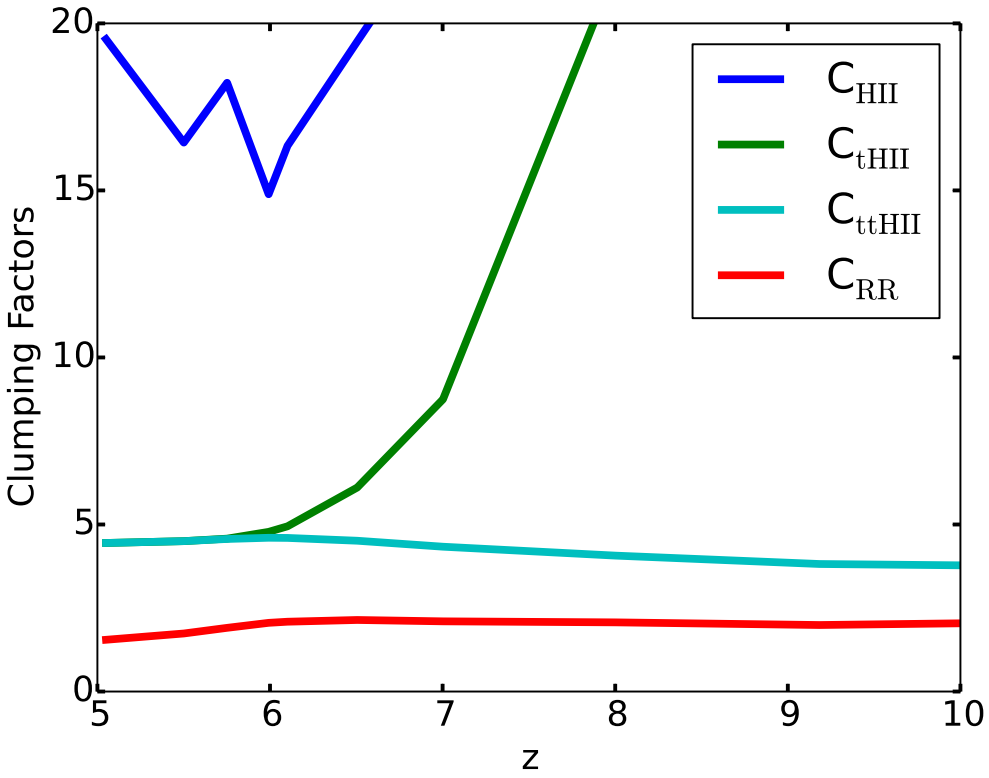

Figure 3.17: Various clumping factors versus redshift. $C_{\mathrm{H\,II}}$ is Equation (3.16) used in $\dot{R}_{\mathrm{H\,II}}$ curve in Figure 3.8, $C_{\mathrm{tH\,II}}$ is used in $\dot{R}_{\mathrm{tH\,II}}$ curve in Figure 3.12, $C_{\mathrm{ttH\,II}}$ is clumping factor with two thresholds applied, $\Delta_b < 100$ and $f_i > 0.1$, shown here solely for comparison. C_{RR} is the value of recombination rate clumping factor from Equation (3.25) with the 5 thresholds applied.

small scales in the ISM. However it is interesting to ask whether there is significant absorption in the denser Circumgalactic Medium (CGM) surrounding galaxies. If we write the total escape fraction as the product of escape fractions, then $f_{esc} = f_{esc}(ISM) f_{esc}(CGM)$. Here we use our simulation to derive an estimate of the globally averaged escape fraction as a function of redshift due to the circumgalactic medium $\bar{f}_{esc}(CGM)$.

Recall from §3.2 that the halo escape fraction is not a model input parameter, but is rather an ouput since the equation of radiative transfer is solved throughout the computational domain. Our halos are not well resolved internally, and so we are underestimating the amount of absorption of ionizing radiation on galaxy ISM scales. However if significant absorption occurs on scales of the virial radius or larger, then that would be simulated reasonably accurately. In the following we assume this is the case, and present results that can be taken to be an upper limit on the total escape fraction (ISM+CGM).

Rather than measure the escape fraction halo by halo and take the average over all halos, we use a simpler method. Since we know every ionization requires an ionizing photon, and we have the ionization rate density as a field defined at every grid cell, then we can estimate $\bar{f}_{esc}(CGM)$ as follows (hereafter we drop the CGM modifier with the reader's understanding that this is what we are estimating):

$$\bar{f}_{esc}(I_t) = \int_{V_t} n_{\rm H\,I} \Gamma^{ph}_{\rm H\,I} d^3x \Big/ \int_V n_{\rm H\,I} \Gamma^{ph}_{\rm H\,I} d^3x, \tag{3.27}$$

where $\Gamma^{ph}_{\rm H\,I}$ is evaluated cell by cell via Equation (3.23), V is the simulation volume and V_t denotes that the integration includes only cells which satisfy $\Delta_b < 100$. In other words, $\bar{f}_{esc}$ is the ratio of the number of ionizations in the IGM, as defined by the overdensity threshold, to the total number of ionizations in the volume. The modifier I_t refers to this method of estimating $\bar{f}_{esc}$ (a superior method is presented below).

The result is plotted in Fig. 3.18. At high redshifts the escape fraction is high and relatively constant at $\bar{f}_{esc} \sim 0.65 - 0.7$. As overlap is approached $\bar{f}_{esc}$ drops considerably, reaching values of ~ 0.2 by $z = 5$. There is no obvious reason why the escape fraction should drop so dramatically at the epoch of overlap.

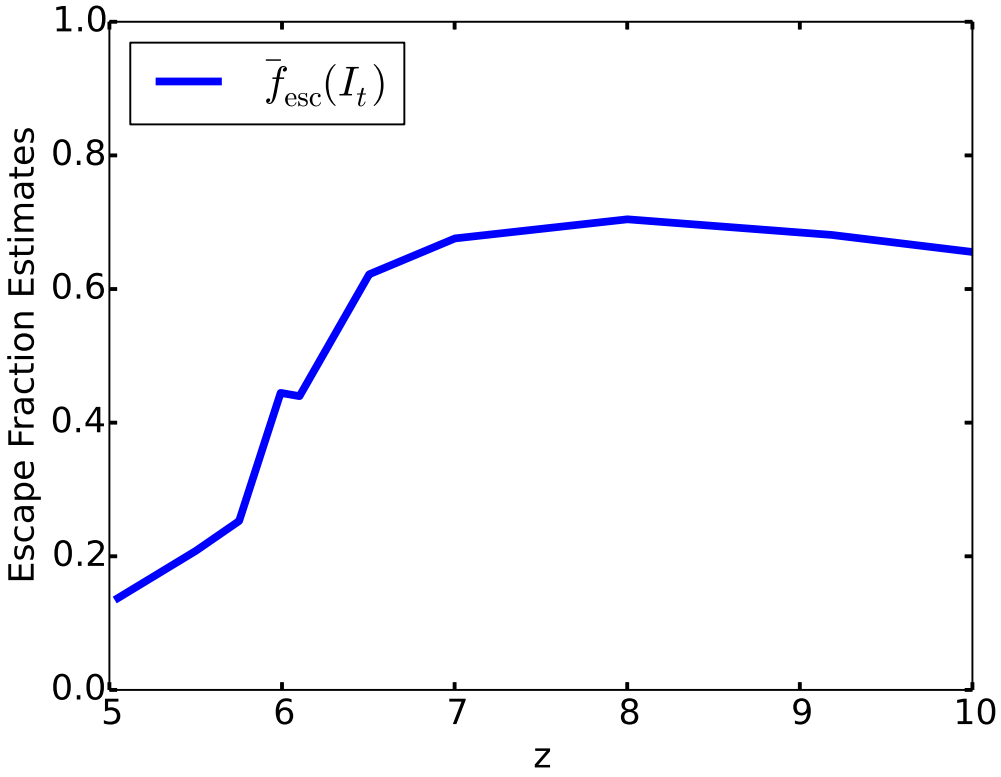

Figure 3.18: Estimate of the globally averaged ionizing radiation escape fraction due to circumgalactic absorption $\bar{f}_{esc}(I_t)$ computed as the ratio of the volume integrated ionization rate in the IGM ($\Delta_b < 100$) to the total ionization rate (Eq. (3.27)).

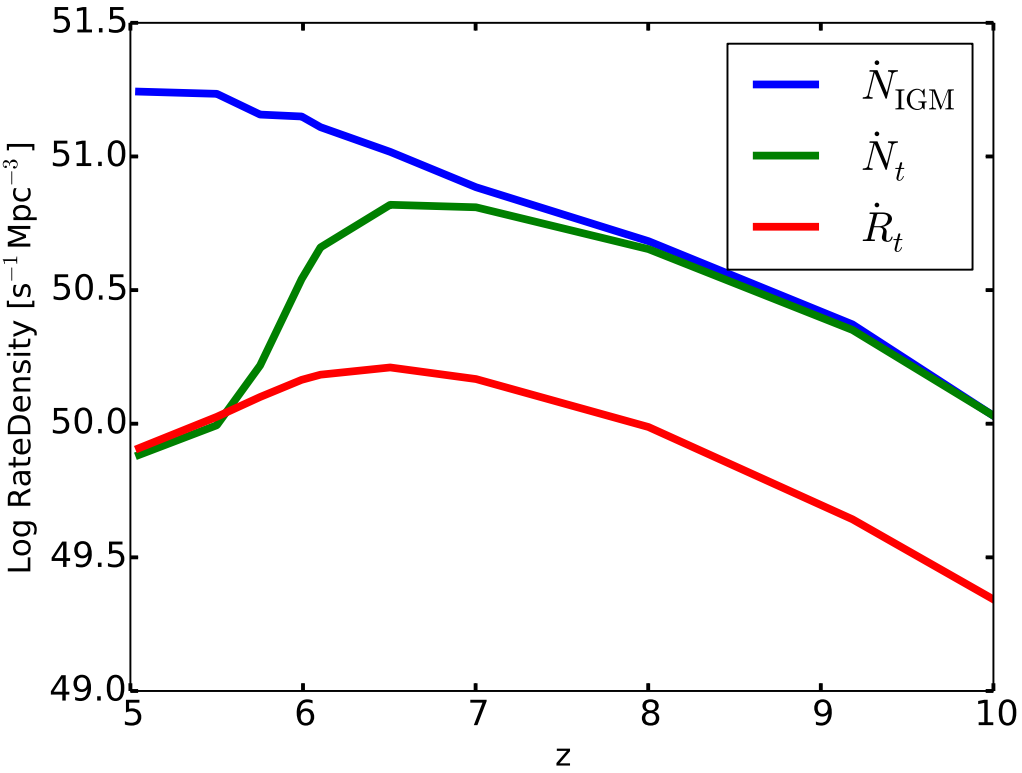

Figure 3.19: Evolution of the volume averaged rate densities for: (1) ionizing photons injected into the IGM ($\dot{N}_{\rm IGM}$), (2) gas photoionization ($\dot{N}_t$), and (3) gas recombination ($\dot{R}_t$) integrated over the singly thresholded volume V_t defined as $\Delta_b < 100$. The ionization rate density curve tracks the photon injection rate density curve in the photon starved regime at high redshifts, but begins to fall below it as the globally averaged ionization parameter approaches unity (Fig. 3.20). After overlap, in the photon abundant regime, the ionization rate density is $\sim 20\times$ the photon injection rate density, but comes into balance with the recombination rate density.

To investigate this properly would require a statistical analysis of individual halo escape fractions, which we defer to a subsequent paper. Perhaps this is an artifact of how we are estimating $\bar{f}_{esc}$. While it is true that every ionization requires an ionizing photon in the photon starved regime (i.e., before overlap), after overlap the volume becomes optically thin to ionizing radiation, and it is not true that every ionizing photon causes an ionization in the box. This is illustrated in Fig. 3.19.

The curve labeled $\dot{N}_t$ is the actual ionization rate density measured in the simulation averaged over the entire 20 Mpc cubic volume satisfying the overdensity threshold $\Delta_b < 100$; i.e. precisely the numerator of Eq. (3.27) divided by 20^3. The curve labeled $\dot{R}_t$ is the recombination rate density averaged over the same volume; i.e.

$$\dot{R}_t = \int_{V_t} n_e n_{\rm H\,II} \alpha_B(T) d^3x. \tag{3.28}$$

We see that ionization rate density $\dot{N}_t$ grows with redshift and reaches a maximum at $z \approx 6.5$, and then drops by roughly 0.8 dex by overlap completion at $z = 5.8$. It continues to decrease thereafter. The reason for this sudden drop is that after overlap there are very few neutral atoms left to ionize ($n_{\rm H\,I}/n_{\rm H} \sim 10^{-5}$).

This can be illustrated by considering the *global ionization parameter*, which is the number of ionizing photons per neutral H atom $\Gamma_{IP} = \langle n_{ph} \rangle / \langle n_{HI} \rangle$ averaged over the entire volume. Specifically, we integrate the grey radiation energy density divided by the mean photon energy $\bar{\epsilon}$ over the singly thresholded volume, and divide by the number of H I atoms in the same volume:

$$\Gamma_{IP} = \int_{V_t} (E/\bar{\epsilon}) d^3x \Big/ \int_{V_t} n_{HI} d^3x. \tag{3.29}$$

We see from Fig. 3.20 that Γ_{IP} grows from $\sim 10^{-3}$ at $z = 10$ to unity at $z \approx 6.5$ just before overlap. Thereafter Γ_{IP} grows very rapidly, reaching a value around 10^5 at the overlap redshift, and leveling off at around 10^6 below that. From the standpoint of the global ionization parameter, reionization begins photon starved but completes photon abundant.

Returning to Fig. 3.19 we see that the recombination rate density $\dot{R}_t$ curve tracks the ionization rate density curve to $z \sim 7$, but is about 0.7 dex lower in

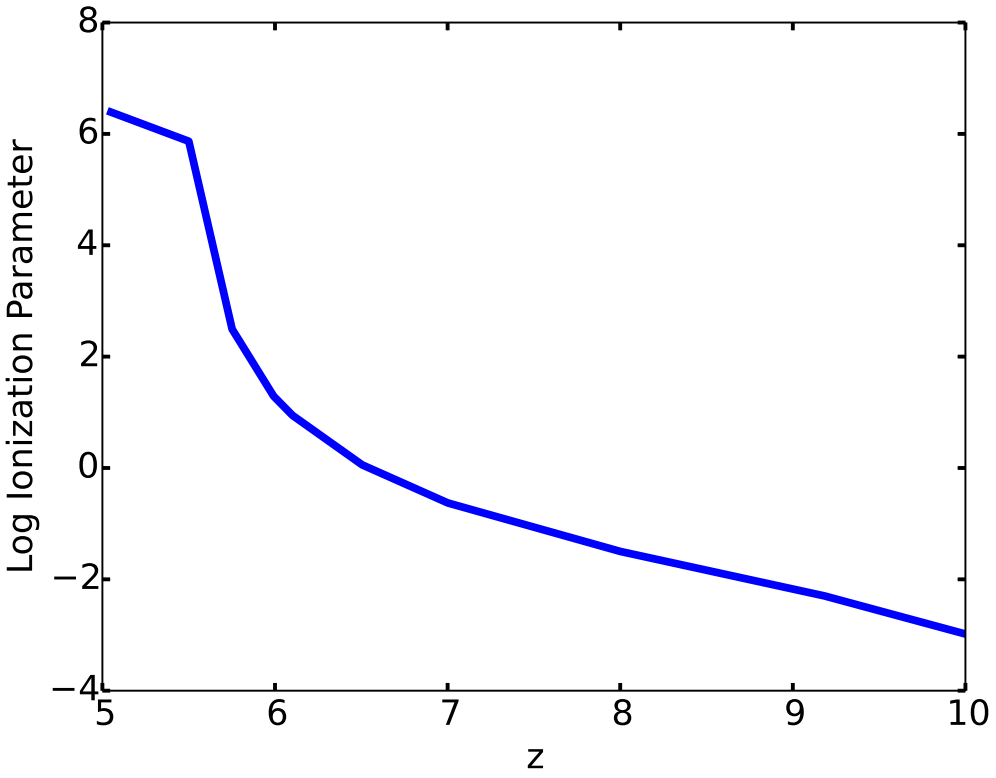

Figure 3.20: Redshift evolution of the global ionization parameter as defined in Eq. (3.29).

magnitude, as it must be if the ionized volume filling fraction is to grow. As overlap is approached ionizations and recombinations come into balance, but the recombination rate density has dropped considerably since it reached its maximum value at $z \approx 6.5$. This is also the redshift at which the ionization rate achieves a maximum, and when the global ionization parameter reaches unity. We also observe that the f_{esc} curve in Fig. 3.18 begins its precipitous drop at this redshift. We believe all of these events signal the rapid rise in the global ionization parameter below $z = 6.5$, and not some change in the escape fraction of young galaxies.

Counting the fraction of all ionizations occurring outside halos is not a reliable estimate of the escape fraction for $\Gamma_{IP} \gg 1$ because it does not count the photons in the radiation field that have nothing to ionize. Therefore we need to modify Eq. (3.27) to include photons which build up the background of the radiation field:

$$\bar{f}_{esc} = \int_{V_t} (n_{\rm H\,I}\Gamma^{ph}_{\rm H\,I} + \frac{1}{\bar{\epsilon}}\frac{dE}{dt})d^3x \Big/ \int_V (\eta/\bar{\epsilon})d^3x. \tag{3.30}$$

Here the numerator is the rate at which ionizing photons are causing ionizations in the IGM and building up the UV background, and the denominator is volume integrated ionizing photon production rate.

Fig. 3.21 plots $\bar{f}_{esc}$ calculated according to Eq. (3.30). Each contribution to $\bar{f}_{esc}$ is plotted separately, as well as the sum. We see that $\bar{f}_{esc}$ is roughly constant with redshift with a value of around 0.6. We see that as the contribution due to ionizations declines below $z \sim 7$, the contribution due to the change in radiation background intensity increases in a compensating fashion. This confirms our earlier suspicions and gives us a better estimate of the mean circumgalactic attenuation of ionizing radiation from young galaxies.

To complete the picture we plot in Fig. 3.19 the number density of ionizing photons escaping into the IGM, calculated as $\dot{N}_{IGM} = \bar{f}_{esc}\dot{N}_{sim}$, where $\dot{N}_{sim}$ is the ionizing photon production rate in the simulation, and $\bar{f}_{esc}$ is the improved estimate for the escape fraction calculated using Equation (3.30). We see that at high redshifts the $\dot{N}_{IGM}$ and $\dot{N}_t$ track each other closely. This tells us two things. First, that reionization at high redshifts when $Q_{\rm H\,II} \ll 1$ is photon starved, in the

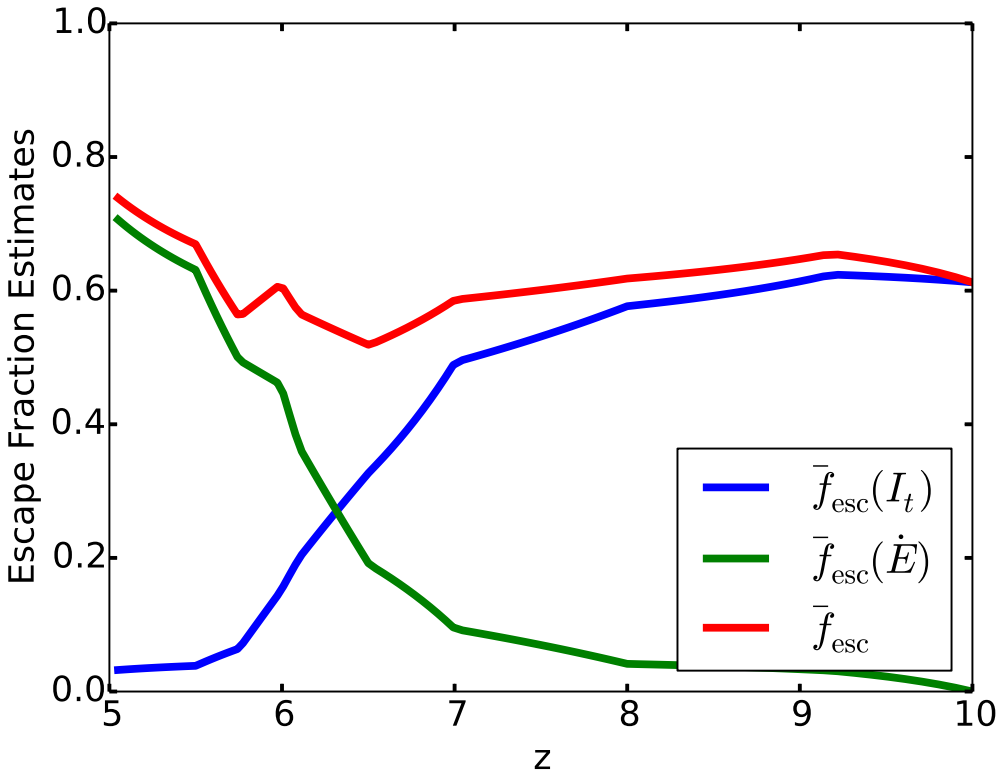

Figure 3.21: Redshift evolution of the globally averaged escape fraction contribution from circumgalactic absorption as estimated by the number of ionizations occuring in the IGM and the buildup of the ionizing radiation background. The curves labeled $\bar{f}_{esc}(I_t), \bar{f}_{esc}(\dot{E})$ plot the contributions of the first and second terms in Eq. (3.30), while the curve labeled $\bar{f}_{esc}$ plots their sum.

sense that every ionizing photon emitted results in an ionization. And second that our estimate of $\bar{f}_{esc}$ is reasonably accurate at these redshifts. However, as redshift decreases, the two curves systematically begin to deviate from one another in the sense that $\dot{N}_t < \dot{N}_{IGM}$. Beginning at $z = 6.5$ the ionization rate density begins to decrease while the ionizing photon production rate into the IGM continues to rise. After overlap the large disparity between the $\dot{N}_{IGM}$ and $\dot{N}_t$ curves can then be understood as saying that the IGM becomes photon abundant.

The ratio of ionization rate density and the photon injection rate into the IGM is plotted in Fig. 3.22. The ratio is unity initially, and slowly decreases until $z \approx 7$, and then drops rapidly as overlap is approached. After overlap the ratio is about 0.05. In other words, after overlap, the photon production rate is about 20× the ionization rate in a volume averaged sense. Since the ionization and recombination rates are in balance after overlap, we conclude that the volume averaged photon injection rate is about 20× the recombination rate.

3.6 An Improved Model for the Evolution of $Q_{\rm H\,II}$

In this section we compare the evolution of the ionized volume fraction $Q_{\rm H\,II}$ from our simulation with the analytic model introduced by Madau et al. (1999). We are motivated to do this because as we have seen from §3.4, Equation (3.1) is not a useful predictor of when $Q_{\rm H\,II}$ reaches unity. We therefore want to investigate the accuracy of the time dependent model from which Equation (3.1) is derived as a limiting case.

Madau et al. (1999) derived the following ODE for the evolution of $Q_{\rm H\,II}$ (their Equation 20):

$$\frac{dQ_{\rm H\,II}}{dt} = \frac{\dot{n}_{ion}}{\bar{n}_{\rm H}} - \frac{Q_{\rm H\,II}}{\bar{t}_{rec}} \tag{3.31}$$

where $\dot{n}_{ion}$ is ionizing photon injection rate, $\bar{n}_{\rm H}$ is the mean density of H atoms in the universe, and $\bar{t}_{rec}$ is some characteristic recombination time taking the clumpiness of the IGM into account. For a constant clumping factor and comoving

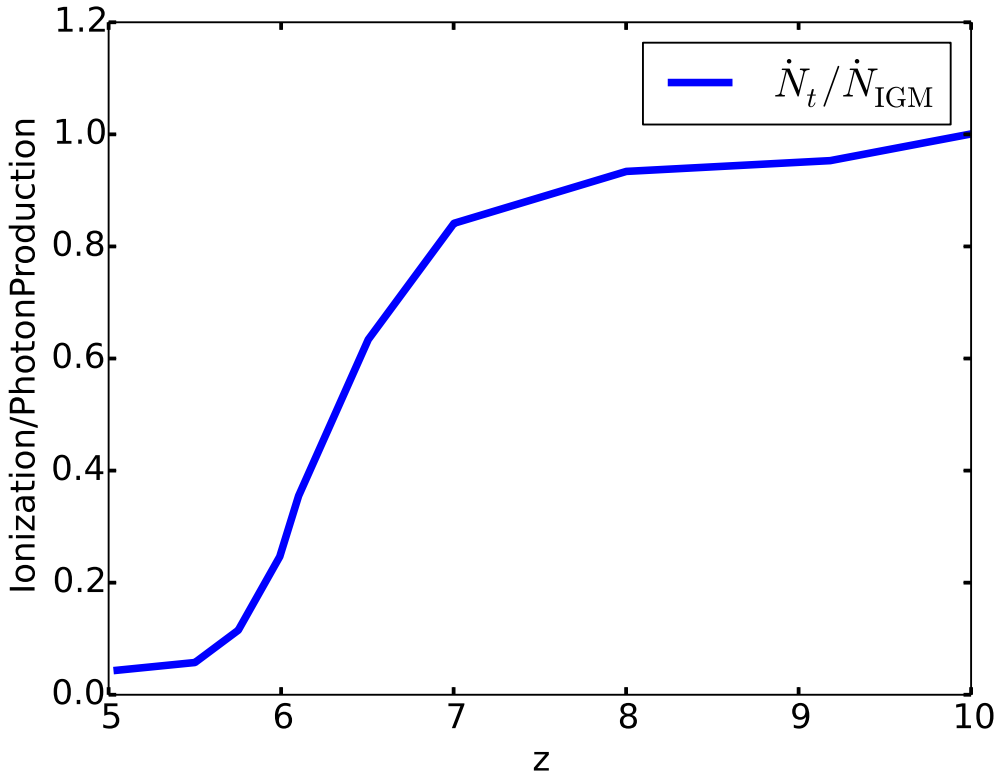

Figure 3.22: Ratio of the volume integrated photoionization rate in the IGM $\dot{N}_t$ to the integrated photon injection rate into the IGM $\dot{N}_{IGM}$, where the IGM is defined as cells with $\Delta_b < 100$. The ratio is near unity initilly, remains high until $z \approx 7$ ($Q_{HII} \approx 0.5$), and then drops rapidly as overlap is approached and the IGM becomes highly ionized.

emissivity Madau et al. (1999) show that

$$Q_{\rm H\,II}(t) \approx \frac{\dot{n}_{ion}}{\bar{n}_{\rm H}} \bar{t}_{rec}. \tag{3.32}$$

Setting $Q = 1$ one arrives at $\dot{n}_{ion}\bar{t}_{rec} = \bar{n}_{\rm H}$, the basis for deriving Equation (3.1). Madau et al. (1999) state that this relation should still be valid provided the clumping factor and comoving emissivity are slowly varying on a timescale of $\bar{t}_{rec}$. We utilize the differential form for our comparison because our emissivity is not a constant value, nor is it slowly varying on a recombination time as $Q \to 1$, as we show below.

A practical issue when testing Equation (3.31) is how $\bar{t}_{rec}$ should be evaluated when $Q < 1$, and in particular when $Q \ll 1$. In the limit $Q \ll 1$ one is dealing with isolated H II regions evolving under the influence of local conditions. Yet the definition for $\bar{t}_{rec}$ in Equation (3.21) invokes *global* values for C and $\langle n_{\rm H\,II} \rangle$. Should these quantitles be evaluated locally only within ionized regions? Or are global estimates good enough? In particular, since Madau et al. (1999)'s Equation (20) uses $\bar{n}_{\rm H}$ as a proxy for $\langle n_{\rm H\,II} \rangle$, what is the appropriate value for C to use?

A second practical issue is what to take for $\dot{n}_{ion}$. This is commonly understood to be the rate at which ionizing photons are injected into the IGM (e.g., Haardt & Madau 2012, §9.3), which in our parlance is $\dot{N}_{IGM}$. Or should we take the actual ionization rate density measured in the simulation $\dot{N}_t$? As we saw in the previous section, these two rates diverge as overlap is approached, and differ by more than an order of magnitude after overlap (Fig. 3.22).

To examine these issues we plot in Figure 3.23 $Q(z)$ from our simulation, as well as theoretical curves obtained by integrating Equation (3.31) under various assumptions. The curve labelled $Q(sim)$ is the ionized volume fraction from our simulation that is at least 99.9% ionized (Well Ionized). The other four curves are obtained by integrating Equation (3.31) setting $\dot{n}_{ion} = \dot{N}_t$ for various choices for $\bar{t}_{rec}$ (we investigate the $\dot{n}_{ion} = \dot{N}_{IGM}$ case at the end of this section.) The integral is approximated by summing a piecewise linear interpolation of the two terms on

the RHS of Equation (3.31) using the trapezoidal rule:

$$Q(t) = \int_{t*}^{t} \frac{dQ}{dt} dt \approx \sum \frac{dQ}{dt} \Delta t$$
$$= \sum_i (\mathrm{Term}_1 - \mathrm{Term}_2)_i \Delta t_i \tag{3.33}$$

where $t*$ is the time when the first star forms in the simulation.

The curve labeled $Q(\langle t_{rec} \rangle)$ uses the volume averaged recombination time (volume average of Equation 3.18). The two curves labeled $Q(t_{\mathrm{Madau}})$ use Equation (3.21) to evaluate $\bar{t}_{rec}$ for $C = 2$ and 3, substituting $\bar{n}_{\mathrm{H}}$ for $\langle n_{\mathrm{H\,II}} \rangle$ and assuming a constant T=10^4K for the IGM. The curve labeled $Q(t_{rec,eff})$ uses the effective recombination time definition

$$\bar{t}_{rec} = t_{rec,eff} \equiv \frac{\langle n_{\mathrm{H\,II}} \rangle}{\langle n_{\mathrm{H\,II}} n_e \alpha_B(T) \rangle}. \tag{3.34}$$

This particular definition makes the last line of Equation (3.20) true trivially, with no assumption about the IGM temperature or ionization state of the hydrogen. It involves no *ad hoc* clumping factors, and represents the actual appropriately averaged recombination time in the simulation. All the above volume averaged quantities have the threshold of $\Delta_b < 100$ applied, and thus exclude dense gas bound to halos. Several of the curves derived from integrating $\frac{dQ}{dt}$ reach values above unity at the end of the overlapping phase. While it is physically impossible to have $Q > 1$ it is not mathematically forbidden, and so we show the complete curves because they give us some insight about the relative contribution of the recombination term (Term_2) as compared to the ionization term (Term_1).

The $Q(\langle t_{rec} \rangle)$ curve ionizes the quickest, reaching $Q = 1$ at $z \sim 6.5$, which is substantially before the simulation which achieves it at $z \approx 5.8$. The reason for this, as we will analyze shortly, is that recombinations play essentially no role in this model. The $Q(t_{rec,eff})$ curve has the same shape as the $Q(sim)$, but is everywhere higher, and crosses $Q = 1$ at $z \sim 6.1$. Given that this integration uses the actual ionization rate density and effective recombination time in the simulation, this discrepancy demands an explanation. We address this below. Finally the $Q(t_{\mathrm{Madau}})$ curves do not match the shape of the $Q(sim)$ curve, ionizing more quickly at early times, and exhibiting a maximum value for Q at $z \sim 6$.

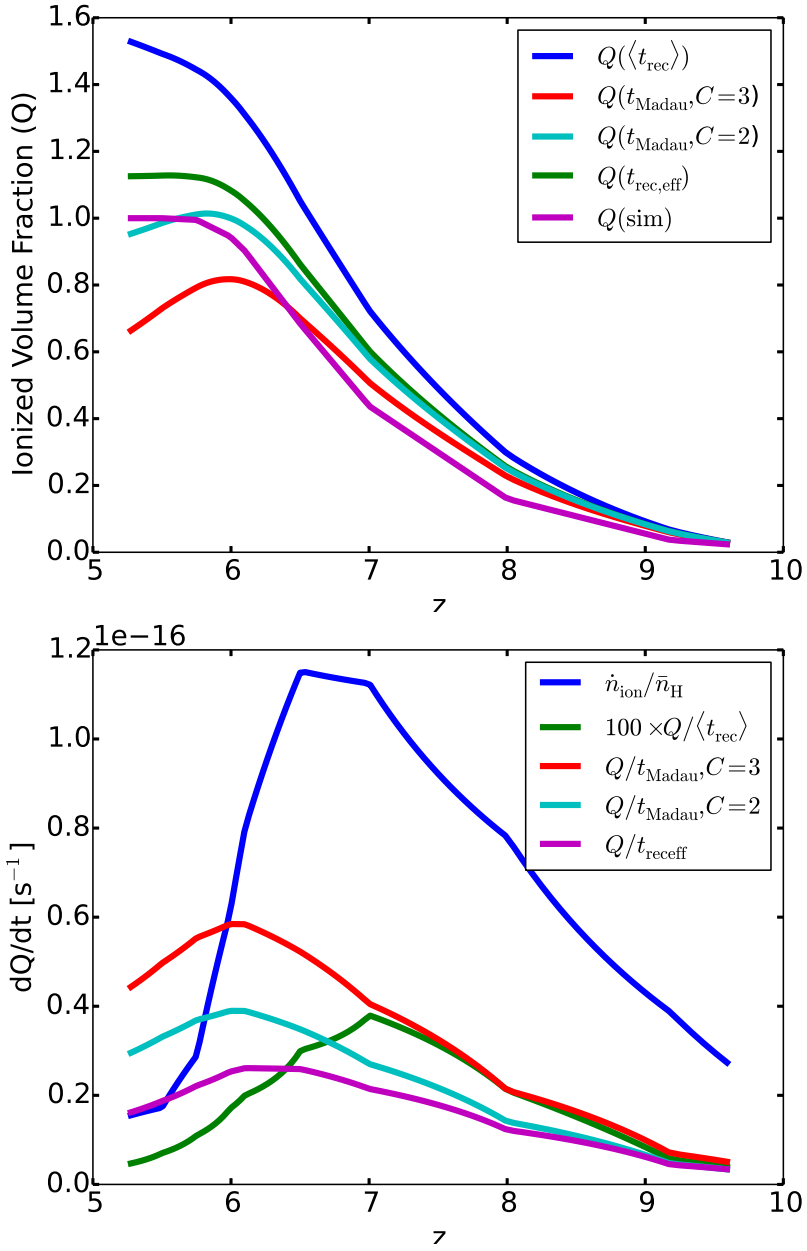

Figure 3.23: *Top*: Comparison of the evolution of the ionized volume fraction Q from our simulation with the analytic model introduced by Madau et al. (1999). Q(sim) is calculated directly from counting the cells satisfying the Well Ionized threshold of $f_i > 0.999$. The other curves are calculated from integrating Equation (3.33) with the different expressions for $\bar{t}_{rec}$ in Term$_2$, as described in the text. *Bottom*: Plot of Term$_1$ and Term$_2$ individually using the different expressions for $\bar{t}_{rec}$.

To understand this behavior more fully we plot in Figure 3.23 *bottom* the values for Term_1 and Term_2 in Equation (3.31). The blue curve is Term_1 of Equation (3.31). The other four curves plot Term_2 with their respective values for $\bar{t}_{rec}$. The ionization curve dominates all the recombination curves at high redshifts, and reaches a maximum at $z \sim 6.5$. This is a partial reflection of the plateauing and subsequent decline of the SFRD shown in Figure 3.3. More fundamentally, it is a reflection of the rapid drop in the neutral fraction of the IGM as overlap is approached. The curve using the volume averaged recombination time $\langle t_{rec} \rangle$ yields such low values compared to the others that we multiply it by 100 to make it more visible. Although this is not the relevant recombination time to use, since it weights low density regions, it is effectively the limiting case $\bar{t}_{rec} \to \infty$. We can therefore interpret the blue curve in Figure 3.23a as an integration of the ionization term only. It is significantly higher than the $Q(sim)$ curve, suggesting that recombinations are important in the simulation at some level. The ionization term dominates the recombination term by factors of $6 - 10$ in the $t_{rec,eff}$ curve until just before overlap, and the two terms come into balance after overlap. The two t_{Madau} recombination curves are subdominant to the ionization term until $z \sim 6$, and at lower redshifts they become dominant. This explains the turnaround in the corresponding Q curves in Figure 3.23a.

The differences in the magnitude of the recombination curves in Figure 3.23b, especially at higher redshifts, is directly attributable to the magnitude of $\bar{t}_{rec}$. For completeness we plot $\bar{t}_{rec}$ versus redshift in Figure 3.24, both unnormalized and normalized by t_{Hubble}. In addition to the three curves for $t_{rec,eff}$ and t_{Madau} for $C = 2, 3$, we also plot t_{Madau} for $C = C_{\mathrm{ttH\,II}}$ and $C = C_{\mathrm{tdm}}$. We see that all the curves with the exception of the Madau formula curve using the thresholded dark matter clumping factor exhibit an increasing recombination time with decreasing redshift, in line with our expections. The latter curve shows the opposite trend, which is due to the fact that the dark matter clumping factor increases with decreasing redshift, even if it is thresholded to exclude halos (see Figure 3.12 bottom). Among the remaining curves the $t_{rec,eff}$ has the highest values, and increases more sharply than the t_{Madau} curves due to the temperature of the IGM. To demonstrate that, we

plot one additional curve (dashed curve) for $t_{rec,eff}$ evaluated assuming a constant $T = 10^4$K in the recombination rate coefficient.

We now comment on the often-made assumption in reionization models that $\bar{t}_{rec} \ll t$. Madau et al. (1999) make this assumption in order to derive Equation (3.1). It is this assumption that allows for an instantaneous analysis of the photon budget to maintain the universe in an ionized state while ignoring history dependent effects. Referring to Figure 3.24b we see this is never true for $t_{rec,eff}$ and it is not true for $t_{\rm Madau}$ at redshifts approaching overlap for any sensible value of C. We therefore conclude that history-dependent effects cannot be ignored, and that this is the reason Equations (3.1), (3.22) and (3.26) mis-predict the epoch of reionization completion. For the same reason applying these formulae at lower redshifts is highly suspect.

Returning to the discrepancy between the $Q(sim)$ and $Q(t_{rec,eff})$ curves in Figure 3.23a, since the most sensible choice for t_{rec} did not give us satisfactory agreement, we wondered what the origin of the discrepancy could be. Since we have shown that recombinations are relatively unimportant at high redshifts, but that the discrepancy is already present at high redshifts, the only possibility is that there is something wrong with the first term of Equation (3.33). Examining the derivation for Equation (3.31) in Madau et al. (1999), it is stated that it "approximately holds for every isolated source of ionizing photon in the IGM." That suggested that our calculation of $\bar{n}_{\rm H}$ may be off from what is originally intended if it is a global average over the entire simulation box. Since the original $\frac{dQ}{dt}$ is derived from the analytical Strömgren sphere model, it assumed a single ionizing source at the center of the volume, and the the average density of the box is just the uniform density everywhere, which might be the discrepancy. In an Inside-out model, I-fronts are not initially propagating in a gas with an average density given by $\bar{n}_H$, but somewhat higher density. Would agreement improve if instead of using $\bar{n}_H$ in the first term of Equation (3.31), we used the local average density?

We therefore modify Equation (3.31) as follows:

$$\frac{dQ}{dt} = \frac{\dot{n}_{ion}}{\delta_b \bar{n}_{\rm H}} - \frac{Q}{\bar{t}_{rec}} \tag{3.35}$$

where we have introduced in the denominator of the first term a factor $\delta_b \geq 1$

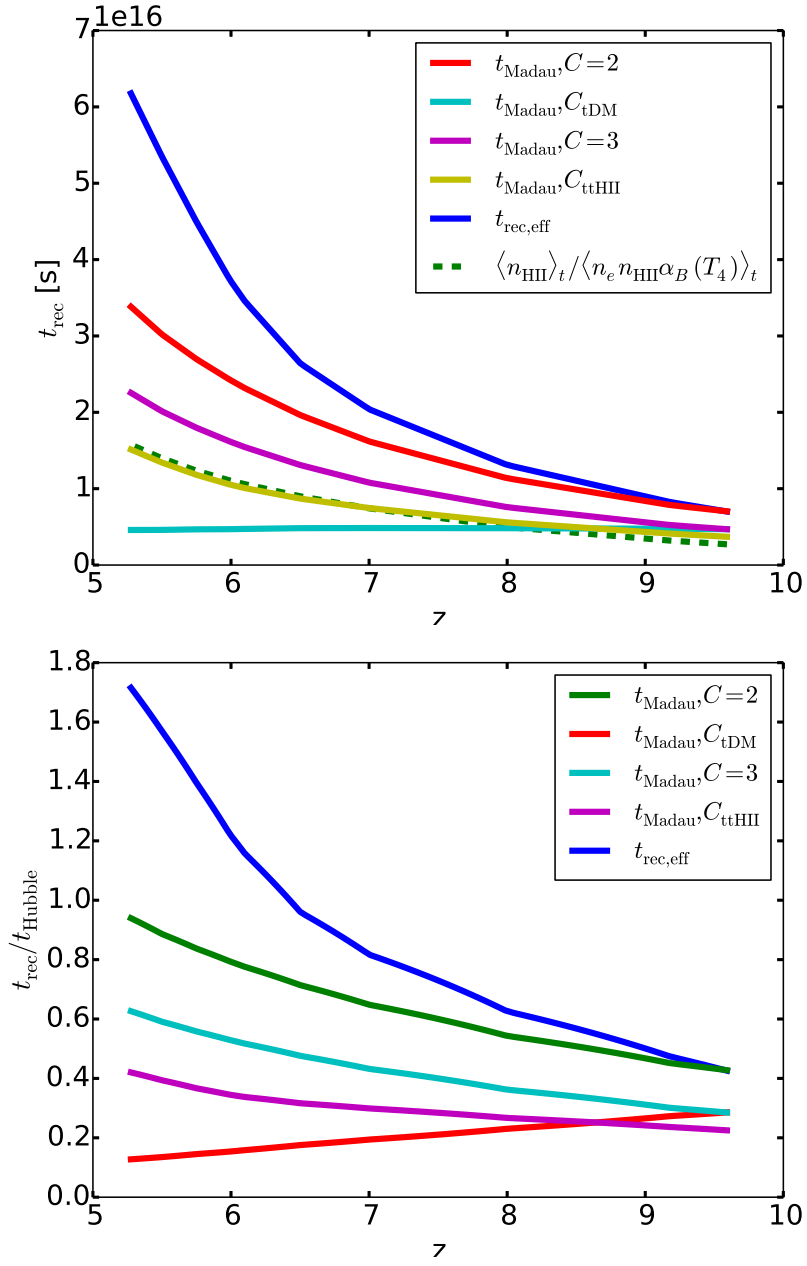

Figure 3.24: *Top*: Recombination time versus redshift, for various expressions for $\bar{t}_{rec}$ as described in the text. Curve labeled $t_{rec,eff}$ is the characteristic recombination time measured directly in the simulation. Curves labeled t_{Madau} evaluate Eq. (3.21) for various choices for the clumping factor C. *Bottom*: Recombination time versus redshift normalized by the Hubble time, for various expressions for $\bar{t}_{rec}$.

which corrects for the higher mean density within ionized bubbles. We measure δ_b from each redshift output as follows: $\delta_b = \langle\rho_b\rangle_{tt}/\langle\rho_b\rangle_t$. The volume average $\langle\rangle$ with subscript t is the usual $\Delta_b < 100$ threshold, the double subscript tt indicates the additional threshold of $x_e > 0.1$. Thus δ_b is the average baryon overdensity within Ionized regions excluding gas inside halos. Figure 3.26 shows a plot of δ_b versus Q together with a simple fitting formula which fits the data extremely well over the domain $0.01 \leq Q \leq 1$.

To see if this formulation improves agreement with our simulated data, in Figure 3.25 we integrate Equation (3.35) again setting $\dot{n}_{ion} = \dot{N}_t$ and using $t_{rec,eff}$ to evaluate the second term. For comparison we show the curve obtained setting $\delta_b = 1$, which repeats a curve already presented in Figure 3.23. Although the simulated and integrated analytic model curves do not agree exactly, the $Q(\delta_b, t_{rec,eff})$ curve shows much better agreement with the simulation, with error on the order of 1% instead of 10%.

By not assuming a constant emissivity and using the modified differential form in determining the volume filling fraction of Equation (3.35), we are able to more accurately model the evolution of the simulated volume filling fraction of H II to the Well Ionized level. For completeness we plot in Figure 3.27 the evolution of $t_{rec,eff}$ used in the above integration, including a reasonably good fit to the data.

Finally, we return to the question of what is the appropriate choice for $\dot{n}_{ion}$ in Equation (3.35). This is commonly taken to be the rate at which ionizing photons are injected into the IGM (e.g., Haardt & Madau 2012, §9.3), because this can be connected to the observed UV luminosity density ρ_{UV} by the formula $\dot{n}_{ion} = f_{esc}\xi_{ion}\rho_{UV}$, where f_{esc} is the escape fraction for ionizing radiation, and ξ_{ion} is the rate of ionizing photons per unit UV (1500 Å) luminosity for the stellar population (Robertson et al., 2013). However we have obtained excellent agreement between simulation and Equation (3.35) using the mean ionization rate density in the IGM $\dot{N}_t$, which differs from the ionizing photon injection rate density $\dot{N}_{IGM}$ as $Q \to 1$. In Figure 3.28 we show the result of integrating Equations (3.31) and (3.35) with the choice $\dot{n}_{ion} = \dot{N}_{IGM}$, as originally proposed by Madau et al. (1999). Also plotted in Figure 3.28 is $Q(sim)$ (blue line) and our best agreeing model (green

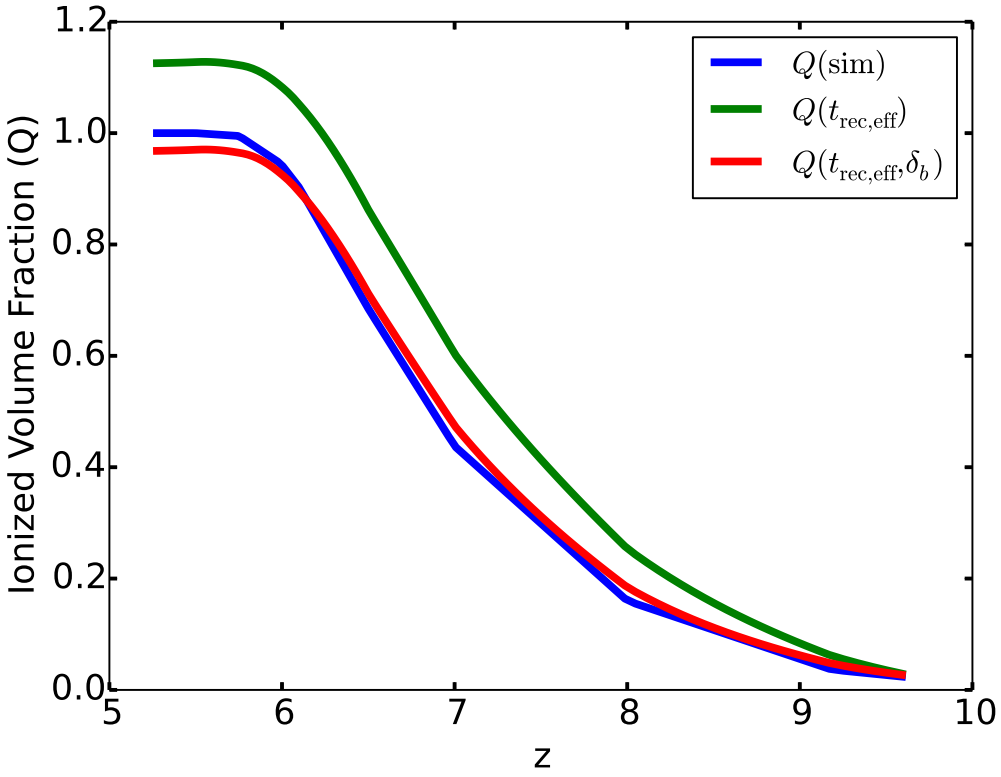

Figure 3.25: Improved agreement between theory and simulation. Green and blue curves are as in Fig. 3.23. Red curve is obtained by integrating modified evolution equation for Q taking into account the overdensity effect of Inside-out reionization (Equation (3.35)).

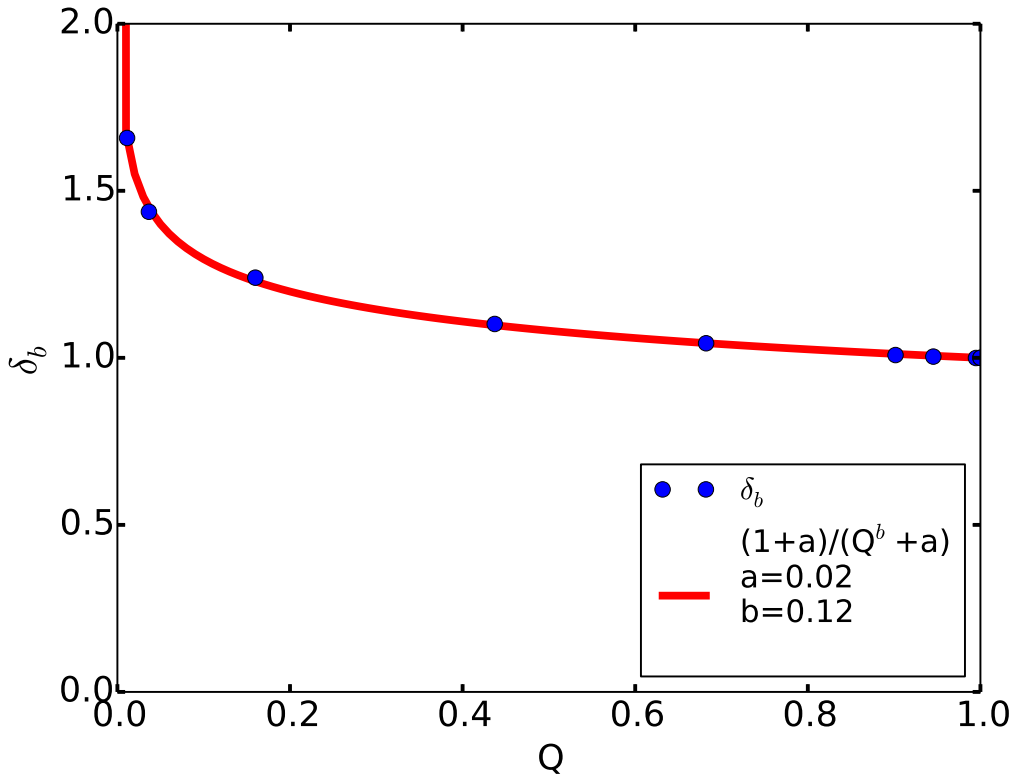

Figure 3.26: Mean baryon overdensity of ionized gas as a function of the ionized volume filling fraction Q. Blue points are measured in the simulation by averaging over the doubly thresholded cells obeying $\Delta_b < 100$ and $x_e > 0.1$. Red curve is a fit to the data.

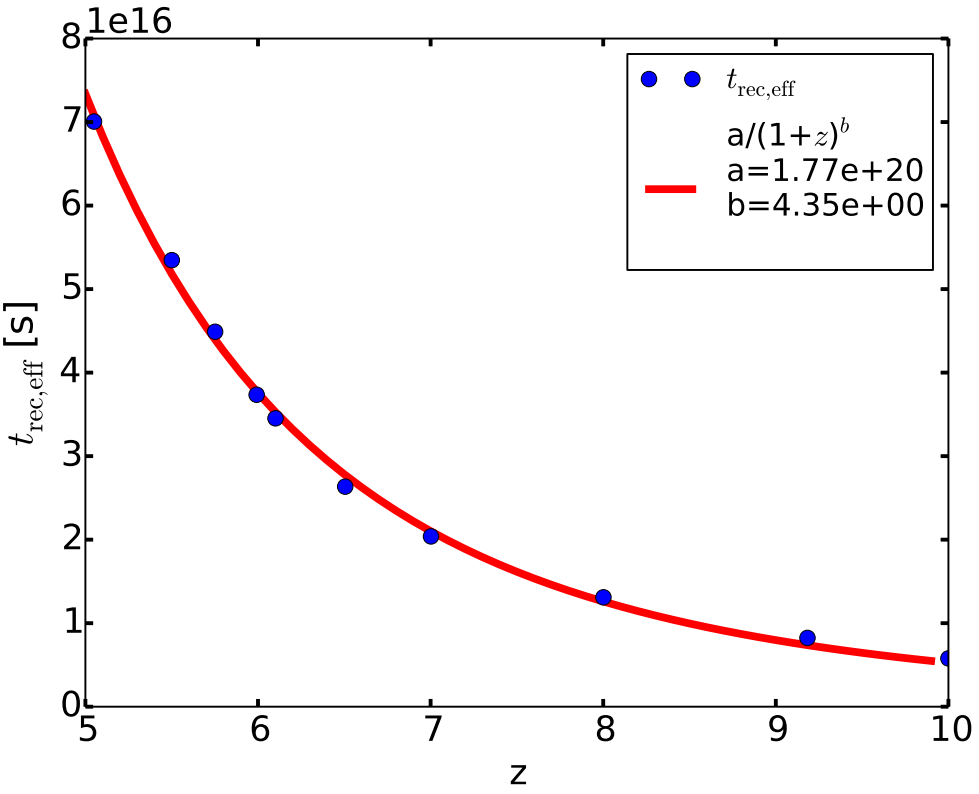

Figure 3.27: Analytic fit to $t_{rec,eff}$ (red line) , evaluated using simulation data (blue points) via Equation (3.34).

line). The red line ignores the δ_b correction, and deviates to the high side of $Q(sim)$ almost immediately, for reasons we discussed earlier. It crosses $Q = 1$ at $z \approx 6.6$, which is too early by $\Delta z = 0.8$. The teal line includes the δ_b correction, and tracks the $Q(sim)$ closely to $z \approx 7$, and thereafter deviates on the high side. It crosses $Q = 1$ at $z \approx 6.4$, which is too early by $\Delta z = 0.6$. Both curves show an accelerated change in Q as z decreases, which is characteristic of standard analytic ionization models (e.g., Haardt & Madau 2012, Fig.14). By contrast, the simulation and our best fit model using $\dot{n}_{ion} = \dot{N}_t$ show a decelerated change in $Q(z)$ as $Q \to 1$. This is clearly due to the fact that the ratio of ionizations to emitted photons decreases as $Q \to 1$, as illustrated in Figure 3.22. The consequence of this flattening in the $Q(z)$ curve is a delay in redshift of overlap of $\Delta z = 0.6 - 0.8$, relative to the predictions of Equations (3.35) and (3.31), respectively, using the photon injection rate as the source term.

We have seen above that the ionization rate density is the appropriate quantity to use to source the dQ/dt equation, independent of δ_b corrections. Because the ionization rate density is not directly observable, but since $\dot{n}_{ion}$ can be derived from observables, we introduce a correction factor to convert from one to the other. Defining

$$\gamma \equiv \frac{\langle n_{HI}\Gamma^{ph}_{HI}\rangle}{\dot{n}_{ion}} = \frac{\dot{N}_t}{\dot{n}_{ion}} \tag{3.36}$$

where the angle brackets denote an average over the singly thresholded volume (IGM), we can recast Equation (3.35) into a form useful for observers:

$$\frac{dQ}{dt} = \frac{\gamma \dot{n}_{ion}}{\delta_b \bar{n}_{\rm H}} - \frac{Q}{\bar{t}_{rec}}, \tag{3.37}$$

where γ and δ_b are functions of Q. In Fig. 3.29 we plot data values for $\gamma(Q)$ taken from our simulation, as well as a simple powerlaw fit. The fit is not meant to be definitive, but merely illustrative. More simulations need to be performed under various circumstances, and better fits made, to see whether our $\gamma(Q)$ is approximately universal, or merely anecdotal.

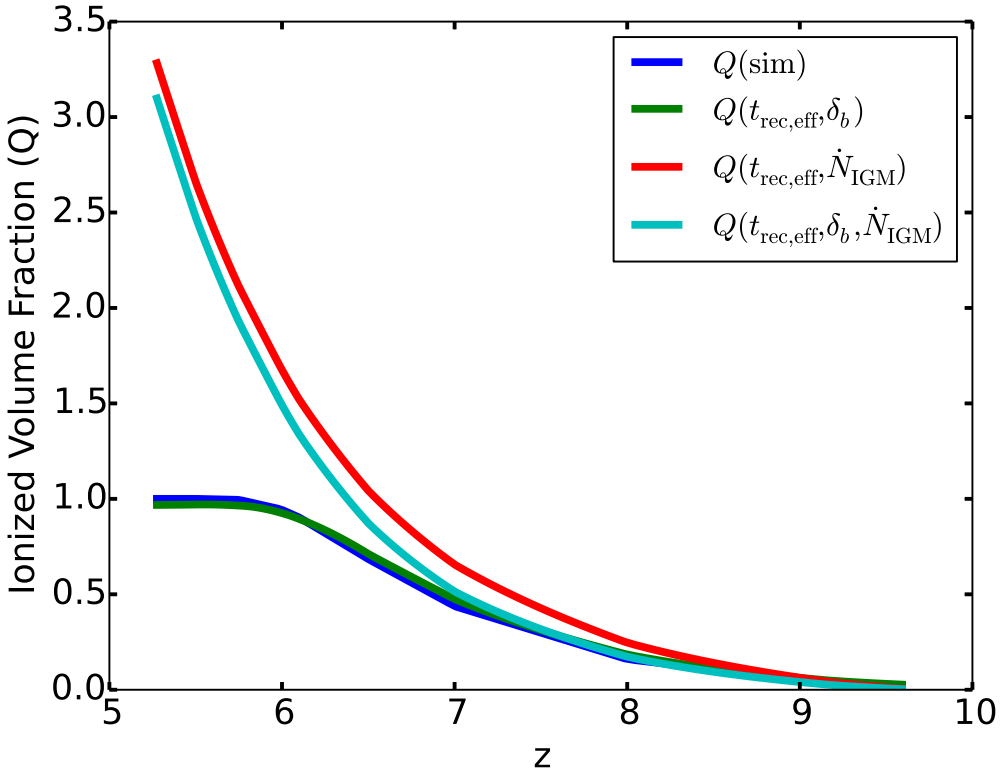

Figure 3.28: Dependence of analytic models on the choice for $\dot{n}_{ion}$. Red and teal curves assume $\dot{n}_{ion} = \dot{N}_{IGM}$; i.e., the photon injection rate into the IGM. Green curve assumes $\dot{n}_{ion} = \dot{N}_t$; i.e., the measured photoionization rate in the IGM. Blue curve is $Q(sim)$–the measured ionized volume filling fraction in the simulation. The green and teal curves take into account the overdensity effect of inside-out reionization (Equation (3.37)), while the red curve assumes $\delta_b = 1$. All models assume $\bar{t}_{rec} = t_{rec,eff}$ as measured in the simulation (Fig. 3.27.

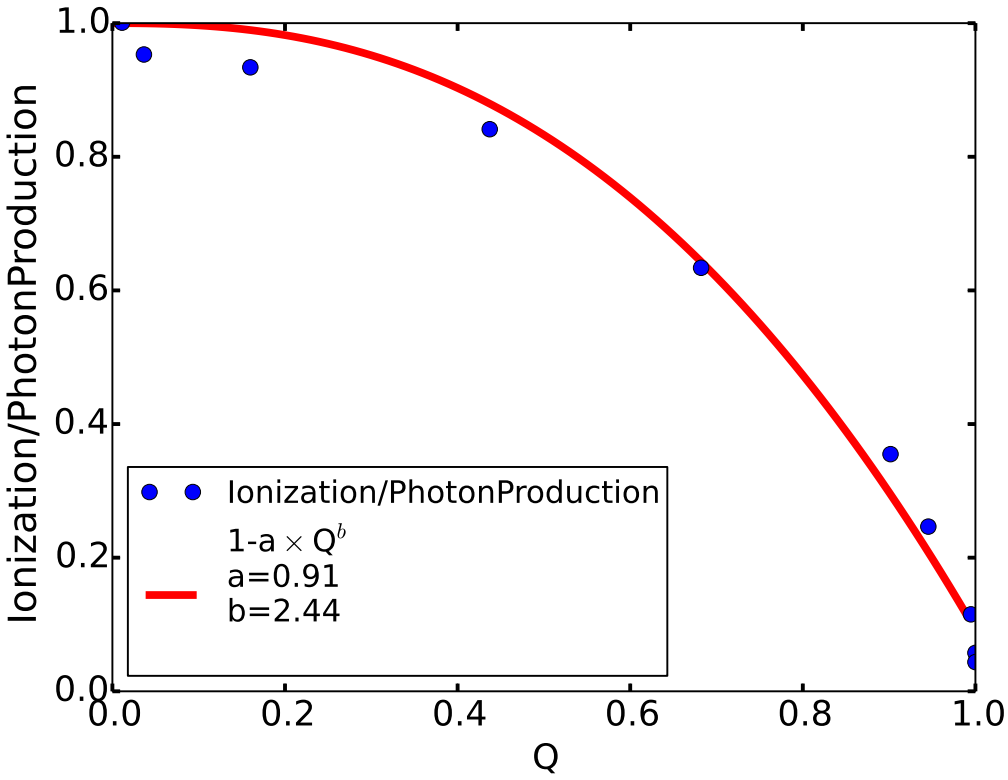

Figure 3.29: Ratio of the volume averaged H I photoionization rate to photon injection rate in the IGM as a function of Q. Data points are measured from the simulation; line is a simple powerlaw fit.

3.7 Discussion

3.7.1 Significance of our Main Results

We have carried out a fully-coupled radiation hydrodynamic cosmological simulation of hydrogen reionization by stellar sources using an efficient flux-limited diffusion radiation transport solver coupled to the Enzo code (Paper I). This method has the virtue of a high degree of scalability with respect to the number of sources, which allows us to simulate reionization in large cosmological volumes including hydrodynamic and radiative feedback effects self-consistently. In this paper we have presented first results from a simulation in a cosmological volume of modest size–20 Mpc comoving–to investigate the detailed radiative transfer, nonequilibrium photoionization, photoheating and recombination processes that operate during reionization and dictate its progress. In a future paper we apply our method to larger volumes to examine the large scale structure of reionization, evolution of the bubble size distribution, etc.

The simulation presented here is carried out on a uniform mesh of 800^3 cells and with an equivalent number of dark matter particles. As such, the mass resolution is sufficiently high to evolve a dark matter halo population which is complete down to ($M_{halo} \approx 10^8 M_{\odot}$) and cools via H and He atomic lines. However, a spatial resolution of 25 kpc comoving poorly resolves internal processes within early galaxies, but does an excellent job of resolving the Jeans length in the photoionized IGM (Bryan et al., 1999). Our simulation is most appropriately thought of as a high redshift IGM simulation which evolves an inhomogeneous ionizing radiation field sourced by star-forming early galaxies. Star formation is modeled using a modified version of the Cen & Ostriker (1992) recipe that can be tuned to reproduce the observed star formation rate density (SFRD) (Smith et al., 2011). We have tuned our simulation to roughly match the observed SFRD (Bouwens et al., 2011a; Robertson et al., 2013) for $z \geq 7$, but due to the small boxsize, it somewhat underpredicts the SFRD for $z < 7$. Our simulation also matches the observed $z = 6$ galaxy luminosity function well, which gives us some confidence that our ionizing souce population is representative of the real universe. However

a substantial fraction of our ionizing flux comes from sources that are too faint to be observed; we defer a discussion of this topic to Paper III in this series (So et al., *in prep.*)

Our goal was not to predict the precise redshift of ionization completion, as this would depend on details such as escape fraction of ionizing radiation from galaxies and their stellar populations that we do not model directly. Rather our goal was to examine the mechanics of reionization in its early, intermediate, and late phases within a model which is calibrated to the observed source population. Nonetheless, we present a model in which reionization completes at $z \approx 6$, consistent with observations.

At early and intermediate times we find that reionization proceeds "inside-out", confirming the results of many previous investigations (Gnedin, 2000a; Razoumov et al., 2002; Sokasian et al., 2003; Furlanetto et al., 2004a; Iliev et al., 2006; Trac & Cen, 2007; Trac et al., 2008). However, at late times isolated islands of neutral gas are ionized from the outside-in as they have no internal sources of ionization. Even this characterization is somewhat oversimplified when *degree of ionization* is considered, as we discussed in Sec. 3.3.2. It accurately depicts how reionization proceeds for a low degree of ionization (> 0). However for high degrees of ionization, "inside-out-middle" is more appropriate, as filaments lag behind low and high density regions, as discussed by Finlator et al. (2009b).

Our most interesting findings concern the widely used analytic model of reionization introduced by Madau et al. (1999). Both the instantaneous (Equation 3.1) and time-dependent (Equation 3.31) versions of this model underpredict the time (overpredict the redshift) when reionization completes, when applied to our simulation. There are two reasons for this having to do with the detailed mechanics of reionization at early and late times respectively. At early times, I-fronts are propagating in regions of higher density than the cosmic mean since the first sources are highly biased. Higher densities translate into slower bubble expansion rates, retarding Q_{HII} (z) relative to a solution which assumes the cosmic mean density (Figure 3.25). At late times, which we loosely define as $Q_{HII} > 0.5$, conversion of ionizing photons into new ionized hydrogen atoms becomes inefficient. This can

be seen by forming this ratio directly from the simulation data (Figure 3.22), or by defining a global H I ionization parameter (Equation (3.29) and Figure 3.20). The consequence of this dropping ionization efficiency, which is as low as 0.05 at overlap in our simulation, is to further retard Q_{HII} (z) relative to a solution which assumes an ionization efficiency of unity (Figure 3.28).

We have introduced a modified version of Madau et al. (1999)'s time-dependent analytic reionization model in Equation (3.37). Modifications which correct for the above-mentioned effects apply to the source term only, *not to the recombination term.* These corrections are therefore totally independent of issues like clumping factors and the temperature of the IGM, which enter into the characteristic recombination time of the IGM. The modifications are introduced as correction factors to the mean density of baryons in the vicinity of ionizing sources at early times (δ_b), and the ratio of ionizing photons emitted to H I photoionization rate at late times (γ). Fits of these two correction factors versus Q_{HII} are presented in Figures 3.26 and 3.29 for consumption by other researchers. At this point we do not know how general these results are. However we have indications based on another simulation we have analyzed with a softer source SED that the functional forms are representative of this class of reionization model.

The significance of these results to high redshift galaxy observers is the following. Setting $Q_{HII} = 1$ and $\delta_b = 1$ in Equation (3.37), we derive

$$\dot{n}_{ion} = \frac{1}{\gamma}\frac{\bar{n}_H}{\bar{t}_{rec}}. \tag{3.38}$$

This differs from the usual expression used to assess whether a given ionizing photon injection rate can maintain an ionized IGM by the factor $1/\gamma$, which is a factor of $\sim$ 20 at overlap in our simulation. If this result is correct, then it means that the required UV luminosity density to maintain an ionized IGM has been underestimated by a factor of approximately 20. However, a more precise statement would be that the UV luminosity density required to maintain the IGM in a *highly ionized state;* $f_n = 10^{-5}$ is 20 times higher than what has been previously estimated. Lower levels of UV luminosity density than that specified in Equation (3.38) could still maintain the IGM in an ionized state, but one with a higher neutral fraction.

As we showed in Figure 3.24, the effective recombination time at and after overlap in our model is comparable to the Hubble time, whether we use the Madau formula to evaluate it for reasonable values for the clumping factor, or we evaluate it directly from our simulation data. This fact casts in doubt the entire instantaneous photon counting argument which is the basis of Equation 3.1, and the equation becomes less useful for the purposes to which it has been applied (e.g., Robertson et al. 2013). It means that the ionization state of the IGM has a memory on the timescale of $\bar{t}_{rec}$ which is always a significant fraction of t_{Hubble} before overlap, and of order the Hubble time after overlap. We therefore recommend observers use the time-dependent version Equation (3.37) in future assessments of high redshift galaxy populations and their role in reionization.

3.7.2 Limitations of the Simulation

We conclude this section with a brief discussion of the known limitations of our simulation and a comparison of our results with others in the published literature. First the limitations. The principal limitation is the use of a uniform grid, which prevents us from resolving processes occuring inside galaxy halos. The main defect this introduces is an inability to calculate the ionizing escape fraction directly, as is done in some high resolution simulations; e.g., Wise & Cen (2009); Fernandez & Shull (2011). In our simulation, we calibrate our star formation recipe to match the observed SFRD, and then use that that to calculate UV feedback cell-by-cell via Equation (3.15). We use a value for ϵ_{UV} taken from Ricotti et al. (2002) for an unattenuated low metallicity stellar population. We underestimate the amount of internal attenuation of ionizing flux due to our limited resolution within halos, and we do not incorporate an explicit escape fraction parameter in Equation (3.15). Effectively, we assume $f_{esc}(ISM) = 1$. Using a lower value for f_{esc} would result in a lower overlap redshift (Petkova & Springel, 2011b). Clearly, it would be desirable to vary this parameter in future studies.

A second limitation of our simulation is that we have presented only one realization in a relatively small box. Previous studies have shown that H II bubbles reach a characteristic size of ~ 10 Mpc comoving in the lates stages of reionization

(Furlanetto et al., 2004a; Zahn et al., 2007a; Shin et al., 2008). At 20 Mpc on a side, our box is scarcely larger than this. Therefore one can ask how robust our results are to boxsize. We have addressed this by carrying out a simulation of identical physics, spatial, and mass resolution in a volume 64 times as large as the one described in this paper. The simulation is carried out in a box 80 Mpc on a side on a uniform mesh of 3200^3 cells, and with an equivalent number of dark matter particles. Results of this simulation will be presented in a forthcoming paper (So et al., in preparation). For the present we merely state that the Q_{HII} (z) curve for the 800^3 simulation falls within the $\pm 1\sigma$ band for the larger simulation, where this band is obtained by subdividing the large simulation into 64 cubes of size 20 Mpc on a side, and calculating the mean and standard deviation. While the larger box begins to ionize at a slightly earlier redshift, due to the presence of higher sigma peaks forming galaxies, both simulations complete reionization at the same redshift, $z_{reion} = 5.8$. The Q_{HII} (z) curve for the 800^3 simulation is near the lower edge of the band, which means that at intermediate redshifts ($7 \leq z \leq 8$), where the difference is largest, the small box simulation underestimates the fraction of the volume that is ionized by about 20%, with differences smoothly decreasing to lower and higher redshift.

A third limitation is that our SFRD systematically deviates from observations below $z \sim 7$, flattening and then decreasing slightly, rather than continuing to rise (Figure 3.3). The large box simulation does not show this effect, but rather tracks the observed SFRD over the entire range of redshifts. The difference in the mean SFRD between the large and small box simulations increases smoothly from 0.1 dex at $z = 9$ to 0.3 dex at $z = 6$. The higher levels of star formation in the large box simulation account for the higher ionized volume fraction at intermediate redshifts. Nonetheless, the two simulations complete reionization at virtually the same redshift, which is a curious result which we address in a subsequent paper.

Another limitation of our method is the use of flux-limited diffusion (FLD) to transport radiation. It is well known that FLD does not cast shadows behind opaque blobs. This could potentially overestimate how rapidly the IGM ionizes, and hence overestimate z_{reion}. In Paper I we showed through a direct comparison

between FLD and an adaptive ray tracing method incorporated in the *Enzo* code on a standard test problem that the differences in the volume- and mass-weighted ionized volume fraction are small. This was for a rather small volume with a small number of ionizing sources. The differences will likely be even smaller as larger volumes containing larger numbers of sources are considered. At the present time, no fully-coupled radiation hydrodynamic simulations of reionization using ray tracing in large volumes are available to compare our method against, to confirm or deny this conjecture.

3.7.3 Comparison with Other Self-Consistent Simulations

Finally, we compare our results to the results of several recent fully-coupled simulations of reionization including hydrodynamics, star formation, and radiative transfer. Petkova & Springel (2011b) simulated a (10 Mpc/h)^3 volume with the `Gadget-2` code coupled to a variable tensor Eddington factor moment method for the ionizing radiation field sourced by star forming galaxies. They carried out a suite of simulations with 2×128^3 gas and dark matter particles, varying the ionizing escape fraction and the mean energy per photon from hot, young stars. The also performed one simulation at 2×256^3 resolution to check for convergence. Our simulation has 80/10 times superior mass resolution as their $128^3/256^3$ simulations. Because `Gadget` is a Lagrangian code, our Eulerian simulation has 8/16 times lower resolution in the highest density regions, but 4.46/2.23 times higher resolution at mean density, and even higher resolution compared to the `Gadget` simulations in low density voids. Our method also has a more accurate adaptive subcycling timestepping scheme for the coupled radiation-ionization-energy equations, obviating the need to model nonequilibrium effects by means of a gas heating parameter ϵ.

Morphologically, our results are qualitatively similar, as are the neutral hydrogen fraction versus overdensity phase diagrams. As might be expected from the two methods, the phase diagrams show some differences at the highest and lowest overdensities which is likely a resolution effect. The SFRD in the Petkova & Springel (2011b) simulation is about an order of magnitude higher than observed,

making a direct comparison on Q_{HII} (z) somewhat problematic. However, since they vary the ionizing escape fraction, we can roughly compare their $f_{esc} = 0.1$ case with our results. Their model completes reionization at $z \approx 5$ compared to our own which completes at $z \approx 5.8$. They plot the quantity $log[1 - Q_{HII}\ (z)]$, which makes the end of reionization look abrupt. We plot Q_{HII} (z), which makes the end of reionization look slow. When we plot $log[1 - Q_{HII}\ (z)]$ using our data, it looks very similar to their curves, and shows a rapid plunge in the average neutral fraction at late times. Petkova & Springel (2011b) do not compare with the predictions of the Madau et al. (1999) model, nor do they investigate the evolution of clumping factors, recombination times, or the number of photons per H atom to achieve overlap as we do. We do not investigate the properties of the $z = 3$ IGM via Lyman α forest statistics, as they do. Therefore further comparisons are not possible at this time.

Finlator et al. (2012) examined some of the same issues we have, hence a comparison with their results is informative. They carried out a suite of `Gadget-2` simulations in small volumes (3, 6)Mpc/h coupled to a variable tensor Eddington factor moment method. Unlike Petkova & Springel (2011b), the radiation transport is solved on a uniform Cartesian grid, rather than evaluated using the SPH formalism. The results presented in Finlator et al. (2012) use 2×256^3 dark matter and gas particles, which given their small volumes, yields a similar mass resolution to our simulation, superior spatial resolution in high density regions, and slightly coarser spatial resolution at mean density and below. However, their radiation transport is done on coarse 16^3 mesh, which in their fiducial run is 536 comoving kpc $\approx 20\times$ as coarse as ours. Their simulation thus coarse-grains the radiation field relative to the density field, which necessitates the introduction of a sub (radiation) grid model for unresolved self-shielded gas (i.e., Lyman limit systems). The effect of their subgrid model is to remove some gas in the overdensity regime $1 \leq \Delta_b \leq 50$ in the calculation of the H II clumping factor, thereby lowering it. Since our radiation field is evolved on the same grid as the density field, we have not included an explicit subgrid model for unresolved self-shielded gas. Lyman limit systems, with neutral column densities of $\sim 10^{17}$ cm^{-2}, have a characteristic

size of 10 physical kpc (Schaye, 2001; McQuinn et al., 2011). At $z = 6$ this is 70 comoving kpc, which is resolved by 3 grid cells in our simulation. While this is lower than one would ideally like (5-10 cells), we believe we can make an apples-to-apples comparison between our resolution-matched simulation results and Finlator et al.'s results.

Our results are in broad agreement with those of Finlator et al. (2012), with some minor quantitative differences. We both find that the unthresholded baryon clumping factor C_b significantly overestimates the clumping in ionized gas at redshifts approaching overlap, and therefore that it should not be used to estimate the mean recombination rate in the IGM. We confirm their findings that properly accounting for the ionization state and temperature of gas of moderate overdensities lowers the clumping factor to less than ≈ 6 (in our case less than 5; see Figure 3.17). Finlator et al. quote a value for C_{HII} of 4.9 at $z = 6$ taking self-shielding into account, which is in good agreement with our value of $C_{ttHII} \approx 4.8$. However, they favor a lower value for C of 2.7-3.3 taking temperature corrections into account. This can be compared with our value for $C_{RR} \approx 2.3$, which includes temperature corrections but also excludes gas with $\Delta_b < 1$. Including this low density gas, as Finlator et al. do, would raise this value somewhat since a larger range of densities enter into the average. We conclude therefore that clumping factors derived from our simulation are in good agreement with those reported by Finlator et al. (2012).

We find that approximately 2 photons per hydrogen atom ($\gamma/H \approx 2$) are required to reionize gas satisfying $\Delta_b < 100$–our proxy for the fluctuating IGM. Finlator et al. (2012) quote a model-dependent value for γ/H which depends on the redshift at which the IGM becomes photoheated and thereby Jeans smoothed (their Fig. 7). For $z = 6$, $\gamma/H \approx 5$, significantly higher than our number evaluated directly from the simulation. However, for $z = 8$, when our box is already significantly ionized, $\gamma/H \approx 3$. Because there are many model-dependent assumptions that go into the Finlator et al. estimate, we consider this reasonably good agreement. However we point out that our estimate is the first to be derived from a self-consistent simulation of reionization with no subgrid models aside from the

star formation/radiative feedback recipe.

Finally, Finlator et al. (2012) compare $Q_{HI}(z) = 1 - Q_{HII}(z)$ for their fiducial model with the time-dependent model of Madau et al. (1999). They point out the sensitivity of the redshift of overlap on the choice of clumping factor, which enters into the recombination time, and showed that C_{HII} provides better agreement with theory at early times than C_b, consistent with our findings. Since small discrepancies in $Q_{HII}(z)$ at early times are masked by plotting $Q_{HI}(z)$, Finlator et al. did not discover the need for our overdensity correction δ_b. Similar to us, they found that even with the best clumping factor estimate the analytic model predicts that reionization completes earlier than the simulation by $\Delta z \approx 1$. They ascribe this delay to finite speed-of-light effects (which can only account for $\Delta z = 0.1$), while we ascribe it to nonequilibrium ionization effects. Finlator et al. (2012) did not propose modifications to the Madau et al. (1999) model to improve agreement with simulation, as we do in Equation (3.37).

3.8 Summary and Conclusions

We now summarize our main results.

1. We use a fully self-consistent simulation including self-gravity, dark matter dynamics, cosmological hydrodynamics, chemical ionization and flux limited diffusion radiation transport, to look at the epoch of hydrogen reionization in detail. By tuning our star formation recipe to approximately match the observed high redshift star formation rate density and galaxy luminosity function, we have created a fully coupled radiation hydrodynamical realization of hydrogen reionization which begins to ionize at $z \approx 10$ and completes at $z \approx 5.8$ without further tuning. While our goal is not the detailed prediction of the redshift of ionization completion, the simulation is a realistic enough to analyze in detail the role of recombinations in the clumpy IGM on the progress of reionization.

2. We find that roughly 2 ionizing photons per H atom are required to convert the neutral IGM to a highly ionized state, which supports the "photon

starved" reionization scenario discussed by Bolton & Haehnelt (2007).

3. Reionization proceeds initially "inside-out", meaning that regions of higher mean density ionize first, consistent with previous studies. However the late stages of reionization are better characterized as "outside-in" as isolated neutral islands are swept over by externally driven I-fronts. Intermediate stages of reionization exhibit both characteristics as I-fronts propagate from dense regions to voids to filaments of moderate overdensity. In general, the appropriateness of a given descriptor depends on the level of ionization of the gas, and the reionization process is rather more complicated that these simple descriptions imply.

4. The evolution of the ionized volume fraction with time Q_{HII} (z) depends on the level of ionization chosen to define a parcel of gas as ionized. The curves for ionization fractions $f_i = 0.1$ and $f_i = 0.999$ are very similar, but the curve for $f_i = 0.99999$ is significantly lower at a given redshift, amounting to delay of $\Delta z \approx 1$ relative to the other curves for $Q_{HII} \ll 1$, smoothly decreasing to 0 as the redshift of overlap is approached.

5. Before overlap, 30-40% of the total recombinations occur outside halos in our simulation, where this refers to gas with $\Delta_b < 100$. After overlap, this fraction decreases to 20% and continues to decrease to lower redshifts.

6. Before and after overlap, 3-4% of the total recombinations occur in voids (defined as $\Delta_b < 1$.) While this is a small fraction of all recombinations, it is about 10% of recombinations before overlap, increasing to about 20% by $z = 5$. The contribution of voids to the ionization balance of the IGM is therefore not negligible.

7. The formula for the ionizing photon production rate needed to maintain the IGM in an ionized state derived by Madau et al. (1999) (Eq. 3.1) should not be used to predict the epoch of reionization completion because it ignores history-dependent terms in the global ionization balance which are not ignorable. While not originally intended for this purpose, it is being used

by observers to assess whether increasingly higher redshift populations of star forming galaxies can account for the ionized state of the IGM. A direct application of the formula to our simulation predicts an overlap redshift of $z = 7.4$ compared to the actual value of $z = 5.8$.

8. Estimating the recombination rate density in the IGM before overlap through the use of clumping factors based on density alone is unreliable because it ignores large variations in local ionization state and temperature which increase the effective recombination time compared to density-based estimates. For a currently popular value of the clumping factor $C = 3$ (Shull et al., 2012), the formula for $\bar{t}_{rec}$ from Madau et al. (1999)(Eq. (3.21)) understimates by $2\times$ at all redshifts the effective recombination time measured directly from the simulation. If we adjust C downward so that Eq. (3.21) matches $t_{rec,eff}$ from the simulation, then it is too low by 60% at $z = 6$ due to the aforementioned effects.

9. The assumption that $\bar{t}_{rec}/t \ll 1$ which underlies the derivation of Eq. (3.1) is never valid over the range of reionization redshifts explored by our simulation (Fig. 3.24). Depending on how $\bar{t}_{rec}$ is evaluated, $\bar{t}_{rec}/t$ increases from $0.3-0.4$ at $z = 9.7$ to ≥ 1 at overlap. This means that an instantaneous analysis of the ionization balance in the IGM post overlap is invalid because recombination times are so long.

10. Retaining time-dependent effects is important for the creation of analytic models of global reionization. The analytic model for the evolution of $Q_{\rm HII}$ introduced by Madau et al. (1999)(Eq. (3.31)) retains the important time-dependent effects, and predicts well the shape of our simulated curve, but overpredicts Q_{HII} at all redshifts because it does not take into account that reionization begins in overdense regions consistent with the inside-out paradigm. It also assumes every emitted ionizing photon results in a prompt photoionization, which is not true in our simulation at late times $Q_{HII} > 0.5$. The Madau model, which ignores these effects, predicts a universe which reionizes too soon by $\Delta z \approx 1$. When we introduce correction factors for

these effects into Eq. (3.37) the simulation and model curves agree to approximately 1% accuracy. We recommend researchers use Eq. (3.37) for future analytic studies of reionization.

11. Finally, we present in Figs. 3.26, 3.27, and 3.29 fitting functions for the overdensity correction $\delta_b(Q)$, the effective recombination time derived from our simulation, and the ionization efficiency parameter $\gamma(Q)$ which may be useful for other researchers in the field.

This research was partially supported by National Science Foundation grants AST-0808184 and AST-1109243 and Department of Energy INCITE award AST025 to MLN and DRR. Simulations were performed on the *Kraken* supercomputer operated for the Extreme Science and Engineering Discovery Environment (XSEDE) by the National Institute for Computational Science (NICS), ORNL with support from XRAC allocation MCA-TG98N020 to MLN. MLN, DRR and GS would like to especially acknowledge the tireless devotion to this project by our co-author Robert Harkness who passed away shortly before this manuscript was completed.

Chapter 3 is a reprint of a paper submitted to Astrophysical Journal without the abstract, G. C. So, M. L. Norman, D. R. Reynolds, and R. P. Harkness,"Direct Numerical Simulation of Reionization II: Clumping Factor Evolution and the Photon Budget for Reionization", (submitted ApJ), (2013).

Chapter 4

Radiative Feedback and the Suppression of Star Formation in Low Mass Haloes

4.1 Introduction

Throughout Chapter 2 and 3 we referenced how we calibrated the simulation input against observations. We have done this in the hopes that it will enable us to create a realistic simulation of reionization including all the relevant physical processes given roughly the same amount of ionizing photons as observed. The result is what we think of as a representative history of how the universe transitioned from being mostly neutral to mostly ionized during EoR. Having the series of events during EoR clearly mapped out in Chapter 3, we are poised to identify the physics that are responsible. Of course, the one question that is of paramount importance is what is the role of radiation transport during EoR? Since we expended considerable efforts in the implementation of the FLD radiation transport module in *Enzo*, it is natural that we want to quantify its contribution to the more realistic simulation results.

By comparing different simulations with and without radiation transport, we can get a feel of how the different simulation parameters affect their overall SFR

density. However, to isolate the effects of radiation we have to compare a simulation with radiation against another simulation with similar parameters, differing only in having the radiation effects turned off. Therefore, we also ran a simulation that is identical to the fiducial run but with the FLD radiation transport module switched off. We went another step further and ran an adiabatic simulation with no cooling and supernova feedback. In this way, we would be able to judge how radiation runs are different compared to other works in the literature that have hydrodynamics but no SN feedback, or those with SN feedback but no radiation transport.

Besides isolating the effects of radiation, we also want to make sure that the SFR we arrived at was from careful tuning of the parameters and not by luck or accident. When we first looked at the SFR density of our fiducial simulation, we were content with our tuning of the input parameters because the SFR density was able to match quite well with observations. However, we did not have another simulation with different parameters to compare against to see if this SFR density is stable against small changes in the physics. Since ultimately, we wanted to simulate a larger, more representative volume of the universe, we ran a simulation that is 64× bigger in volume. Additionally, when we later realized that photons with energies above 4 Ryd should not be able to escape into the IGM, we ran another simulation that is identical in all respects with our fiducial simulation except that the input SED is truncated above 4 Ryd.

Another focus of this chapter is to better characterize the population of radiating sources. In our model, the UV emissivity of a given galaxy (halo) is proportional to its instantaneous SFR. Thus far, we have only considered the SFR density, which is the integrated SFR in all galaxies, divided by the volume of the box. Now we wish to examine the SFR in individual galaxies, and look for correlations of SFR with dark matter halo mass. This would tell us the relative contribution of galaxies of different mass to the overall ionizing photon budget.

The distribution of star formation would also shed light on the galaxy luminosity function (LF). We have shown that given our star formation from the fiducial run, we were also able to obtain a luminosity function that is similar to

observations, even though that was not our intention to start off with (see §3.3). It is unclear whether a different SFR in the radiation simulations can yield a LF that stays consistent with the observed LF. As we will show below, there is no one-to-one mapping between the two, and we examine how galaxies of different mass and luminosity contribute to the composite LF.

In order to investigate these questions, we present and discuss the following analysis results. First, we list the suite of simulations that will be used in the analysis in §4.2. There, we give a brief description of each simulation and note the key differences between them. Then in §4.3, we compare and contrast the SFR densities between the radiation simulations. Here, we will focus on the three simulations with FLD radiation transport. After that, we want to compare the SFR of halos of different mass ranges in §4.4. Again this is for the three simulations with radiation, looking for trends and patterns. In §4.5, we compare the fiducial radiation run with non-radiation runs. We want to see if we can spot any obvious radiation effects on the halos' gas content. In §4.6, we turn our attention to how the radiation runs distribute their luminosity by comparing LF of the two smaller radiation simulations against observation. We want to see if we can still recover roughly the same LF by having similar SFR density earlier in §4.3. Then, in §4.7 we look at the overall ionized volume history between the radiation runs. We want to make sure they do not reach EoR too quickly or slowly and identify any odd behaviors.

4.2 Suite of Simulations

We list the suite of simulations for comparisons in Table 4.1. They all have slightly different key input physics. The first simulation on the list BSM10RAD800 (*BSM*) is our fiducial run that was introduced in Chapter 2 and analyzed in detail in Chapter 3. It is simulated in a box of sidelength 20 Mpc comoving with a uniform grid of 800^3 cells, using a distributed star formation and feedback recipe described in Smith et al. (2011) and SED from Pop II stars (Ricotti et al., 2002). The SED800B (*SED*) simulation differs from *BSM* by not having a component of

the SED that is greater than 4 Ryd (>4 Ryd in the table); this has the effect of slightly lowering the overall IGM temperature but increases slightly the ionization rate (see §4.3). The NORAD800B (*NORAD*) simulation uses the same cosmology input parameters as those of the *BSM* run but with the FLD radiation transport module turned off, while keeping the same star formation and supernova (SN) feedback. This simulation has only hydro+N body. The ADIAB800B (*ADIAB*) simulation again uses the same cosmology as those of *NORAD* but this time turning off star formation and SN feedback. This simulation has no cooling and does not form any stars, and no SN winds to blow off collapsing gas. And finally the R3200B (*R32*) simulation uses the same parameters as *BSM* but is now 80 Mpc comoving on a side, with 64× the volume as *BSM*. This simulation is conducted at the same mass and spatial resolution as *BSM* and includes higher order of the matter power spectrum, resulting in more massive rare peaks of highly dense gas.

Table 4.1: Suite of simulations exploring the robustness of the results presented in §4. Simulations will be referred to by *italicized* portion of names.

Simulation Names	box size	resolution	SF/FB	FLD RT	>4Ryd
*BSM*10RAD800	$(20\ \mathrm{Mpc})^3$	800^3	Yes	Yes	Yes
*SED*800B	$(20\ \mathrm{Mpc})^3$	800^3	Yes	Yes	No
*NORAD*800B	$(20\ \mathrm{Mpc})^3$	800^3	Yes	No	N/A
*ADIAB*800B	$(20\ \mathrm{Mpc})^3$	800^3	No	No	N/A
*R32*00B	$(80\ \mathrm{Mpc})^3$	3200^3	Yes	Yes	Yes

4.3 Star Formation Rate Density

The star formation rate of our fiducial run described in §3 assumes the SED from Ricotti et al. (2002), which models the UV emissivity of a low metallicity Population II stellar population with a standard mass function (Salpeter). Since we do not resolve the internal structures of the galaxies in the simulation, we model the feedback processes via a subgrid model described in §2, which includes photons in excess of 4 Ryd. However, there is evidence that these photons with energies higher than 4 Ryd do not leave the galaxy and are absorbed within the galaxy itself, therefore we ran a simulation with the same cosmology only slightly

modifying the SED. The modification is only to zero out the distribution of UV photons with energies higher than 4 Ryd. As a side effect of this modification, the amount of radiation energy that was distributed beyond 4 Ryd is now distributed to below 4 Ryd, contributing more energy to the 1 Ryd ionization threshold of hydrogen. This in turn lowers the overall IGM temperature, but increases the amount of ionization slightly, speeding up the process of reionization.

In Figure 4.1, we plot the different star formation rate densities (SFRD) in units of $M_{\odot}yr^{-1}Mpc^{-3}$ comoving vs. z. The blue curve is from our fiducial run and is the same as in Figure 3.3. In green is the *SED* run with the modified SED where UV photons with energies higher than 4 Ryd are absent. In red is *R32* with the fiducial cosmological parameters except the bigger volume of 80 Mpc comoving on a side. In the process of trying to analyze the simulation with the bigger volume, we ran into the trouble of the analysis machine not having enough memory to hold all the data at once ($\sim O(\mathrm{TB})$). Therefore we resorted to analyzing smaller chunks of them separately and tabulating the results for comparison afterwards. We divided the halo finding into 64 equal subvolumes, each having the same volume as our fiducial run of 20 Mpc comoving on a side. We then calculated a mean and a standard deviation of the SFRD and plot the mean as the red curve and +/- one standard deviation as the yellow region around the red curve.

The point of showing Figure 4.1 is that although resolution and the SED of the star particles do affect the resultant SFRD in the box, the changes we applied do not alter SFRD dramatically by orders of magnitude. We are still relatively close to the observational constraints from Bouwens et al. (2007).

We see that the SFRDs in the *SED* and *R32* simulations are higher than the fiducial simulation, and in fact, in better agreement with observations (compare with Figure 3.3). Therefore we can say that there is some sensitivity of the average SFR on box size and radiation spectrum.

Regarding the box size sensitivity, a larger box samples the ΛCDM matter power spectrum to lower wavenumbers, and therefore there is more total power in the box. This increases the number of dark matter halos of a given mass, and introduces the rare, more massive halos that were excluded by the smaller box.

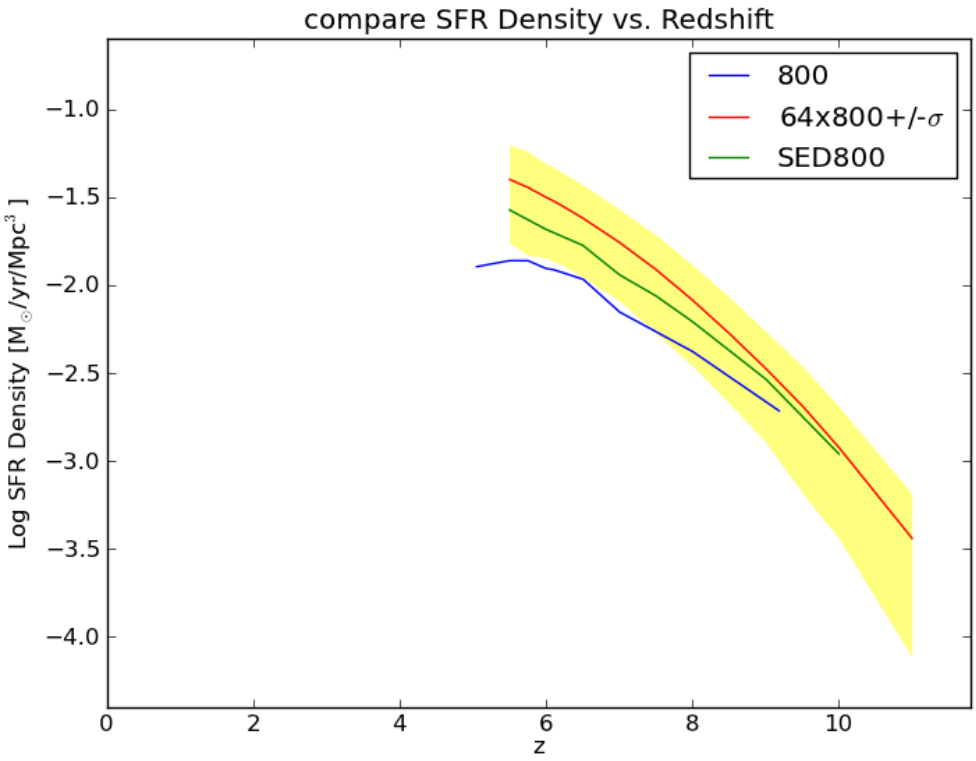

Figure 4.1: Plot of star formation rate density vs. redshift for three simulations. Blue: Our fiducial run. Green: Run with a modified SED where UV photons with energies higher than 4 Ryd are neglected. Red: Run with the fiducial cosmological parameters except the bigger volume of $(80\ \mathrm{Mpc})^3$ comoving. Halo analysis done by cutting the halo finding to 1/64th of volume at a time, red represents the mean and yellow the +/- one standard deviation.

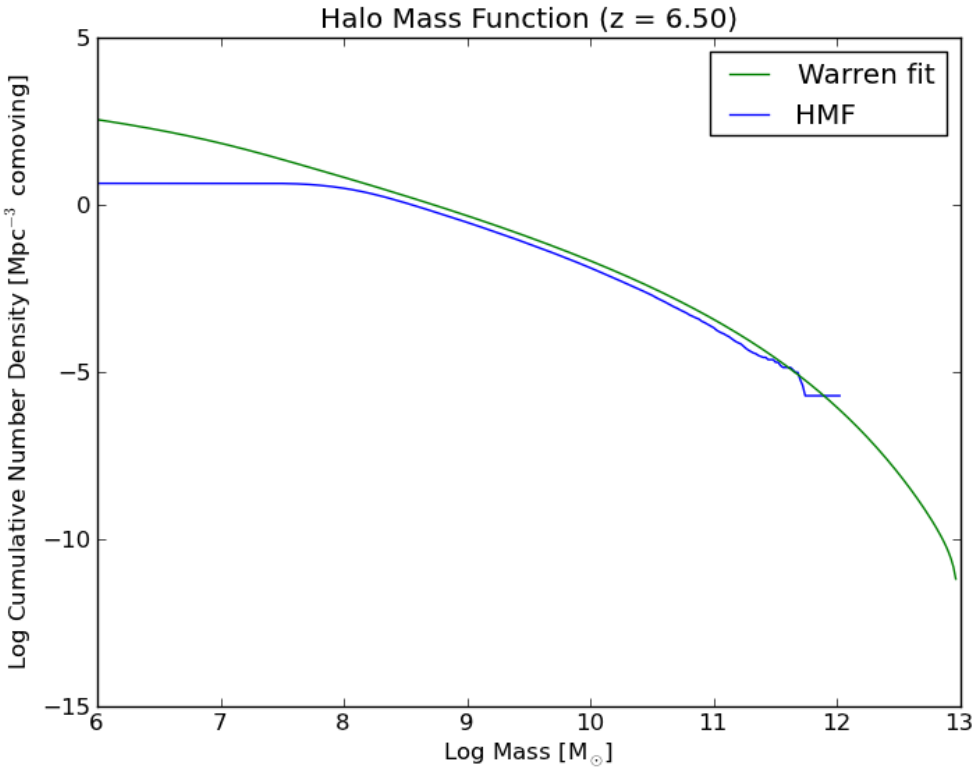

Figure 4.2: Halo Mass Function of *R32* at a redshift of 6.5. Even at this earlier redshift we see that the box size samples the rarer density peak and produced halo with roughly 10^{12}M$_\odot$, larger than the largest halo of *BSM* at a $z = 5.0$ shown in Figure 3.4.

This is shown in Figure 4.2 which shows that the *R32* simulation has generated halos with mass of 10^{12}M$_\odot$. This compares directly with the halo mass functions for the fiducial *BSM* shown in Figure 3.4. This also results in more star formation overall for *R32*. We see in Figure 4.1 that the *BSM* run falls within the band for redshifts $z > 6$, albeit close to the -1σ lower boundary.

Regarding the SED sensitivity, we speculate that the softer radiation spectrum heats the IGM to a lower temperature and hence pressure, which allows halos to retain somewhat more of their gas. This supports slightly more star formation in a halo of a given mass. This conjecture will be investigated in the next section.

4.4 Star Formation Rate vs. Dark Matter Mass

Knowing that the SFRD is not significantly different gives us confidence in our comparisons between the different simulations. We want to look at how different halos of different mass (in this case we measured their dark matter mass only) formed stars. We plot in Figures 4.3, 4.4, 4.5 the SFR versus the dark matter mass of the host halos for the *BSM*, *SED*, and *R32* simulations respectively. We compare these three here because they all have radiation transport and we would like to know what the simulations yield in terms of SFR of halos when radiation is present.

The halos are found using the `yt` (Turk et al., 2011) parallel HOP halo finder, then encapsulated in the ellipsoid 3D data object when determining its SFR and gas mass. Since the 3D object wraps around all the dark matter particles found during the halo finder phase, this can potentially lead to some region being counted toward multiple halos. If the double counted region includes emissivity, this may lead to a slight over-counting of the total emissivity. The alternative is to use the virial radius to encapsulate halos in small spheres, but this would lead to star forming regions not being accounted for. We deliberately choose the former because we also want to understand the local regional attributes that causes star formation, but perhaps a different approach will yield other interesting results which we will discuss in §5.

Looking at Figure 4.3, we plot at z=5 the SFR in units of $M_\odot yr^{-1}$ vs. halo dark matter mass in units of $M_\odot$ for 1215 star forming halos out of a total of 19879 halos found by the halo finder. This figure shows the most massive halo is around $10^{11.5}M_\odot$ for the *BSM* simulation. It has the most SFR shown in units of $M_\odot yr^{-1}$. For halos with smaller mass, the SFR decreases with a visible trend with scatter around the peak of the trend. However, below $10^9M_\odot$, the trend ends rather abruptly, at which point the scatter also increases. There is a significant spread of low mass ($<10^9M_\odot$) halo with SFR that is on par with those around $10^9M_\odot$, but also some roughly $10^9M_\odot$ halos that have orders of magnitude smaller SFR than their counterparts around the peak of the trend. We want to see if this spread happens in the other simulation with radiation transport as well.

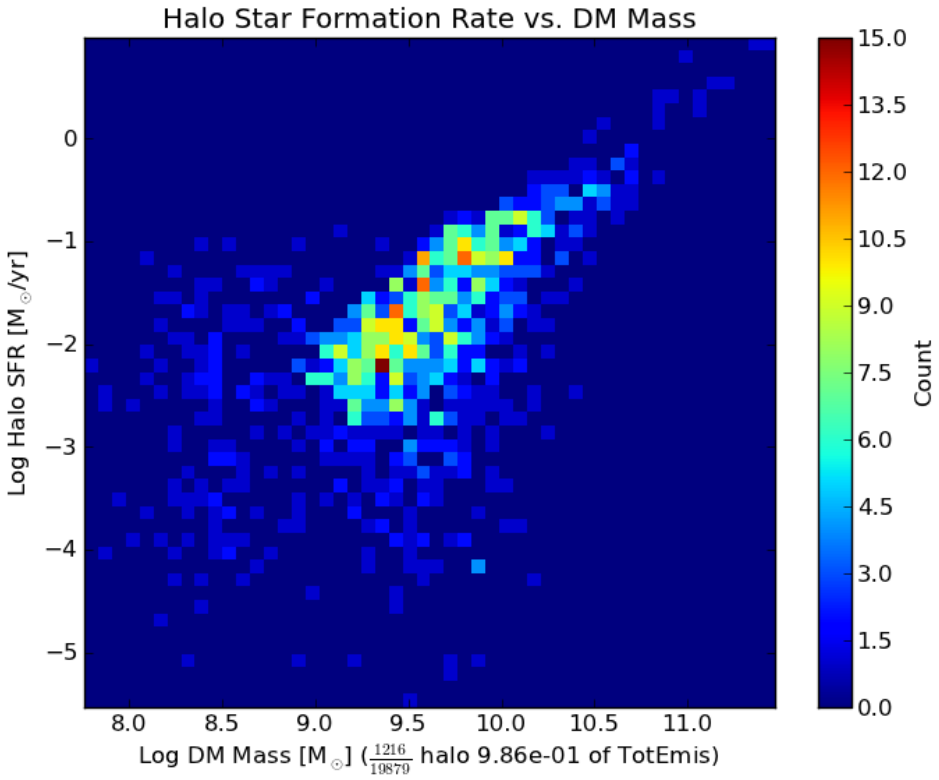

Figure 4.3: Star formation rate within each halo vs. the halo's dark matter mass at z=5 for *BSM*. SFR decreases with decreasing dark matter mass with a visible trend. There is a significant deviation from the trend when the dark matter mass falls below $10^9 M_\odot$. This is data from 1216 star forming halos out of a total of 19879 halos, which contains 98.6% of the emissivity in the simulation.

We plot the same quantities in Figure 4.4 for the *SED* run, and we see that the same general trend appears, but this time the data is from a slightly earlier redshift of z=6. Here, we have 1151 star forming halos out of 44660 halos found by the halo finder. The most massive halo at this earlier z have a mass of around $10^{11.3}M_{\odot}$, and SFR again follows a trend toward around $10^{9}M_{\odot}$ at which point the trend ceases. The spread of data points after the trend ceases below $10^{9}M_{\odot}$ does not seem as prominent in the case of the *SED* run suggesting less SFR there for the *SED*. The peak of the number distribution also seems to be shifted to slightly higher than $10^{9.5}M_{\odot}$ whereas it was slightly below $10^{9.5}M_{\odot}$ in the *BSM* run. We note that there is some overlap of the ellipsoid 3D object, because the emissivity summed from halos is 101% of the total in the box. We do not consider the overlap to be a substantial contribution of error to the trend in the figure because if there is contamination at the high end of the trend, the shape of the trend would be affected, and low end trend contamination would be buried in the trend where there are more halo samples.

There may be other more subtle effects from having a different SED that is not accounted for in this phase diagram, which we will discuss in §5.

Now we look at the simulation with a much bigger volume in Figure 4.5 from *R32*. The largest halo mass starts at around $10^{11.5}M_{\odot}$ at this earlier redshift of $z = 7.3$. There is a much bigger sample of 26336 star forming halos out of 669217 halos. The high mass of the largest halo is an indication that there is more large scale power in the matter power spectrum in the 64$\times$ bigger volume compared to *BSM*. Since objects formed in the hierarchical fashion will accrete more mass over time, we can safely assume that the most massive z=7.3 object will probably grow to larger mass than the most massive halo in the *BSM* run when it reaches the same z of 5. We again note the same slight overcounting of emissivity, but assume it does not change the trend of the SFR seen in the phase diagram.

To see the drop-off in SFR more simply, we plot the sum of the SFR in each mass bin from *R32* in Figure 4.6. We see that on the x-axis in units of $M_{\odot}$, between $10^{11.0}$ and $10^{9.7}$ there is a peak of total SFR in each mass bin, which are fairly stable with values around $10^{2.7}$-$10^{3.0}M_{\odot}yr^{-1}$. Between $10^{9.7}$-$10^{9.0}M_{\odot}$ however, the total

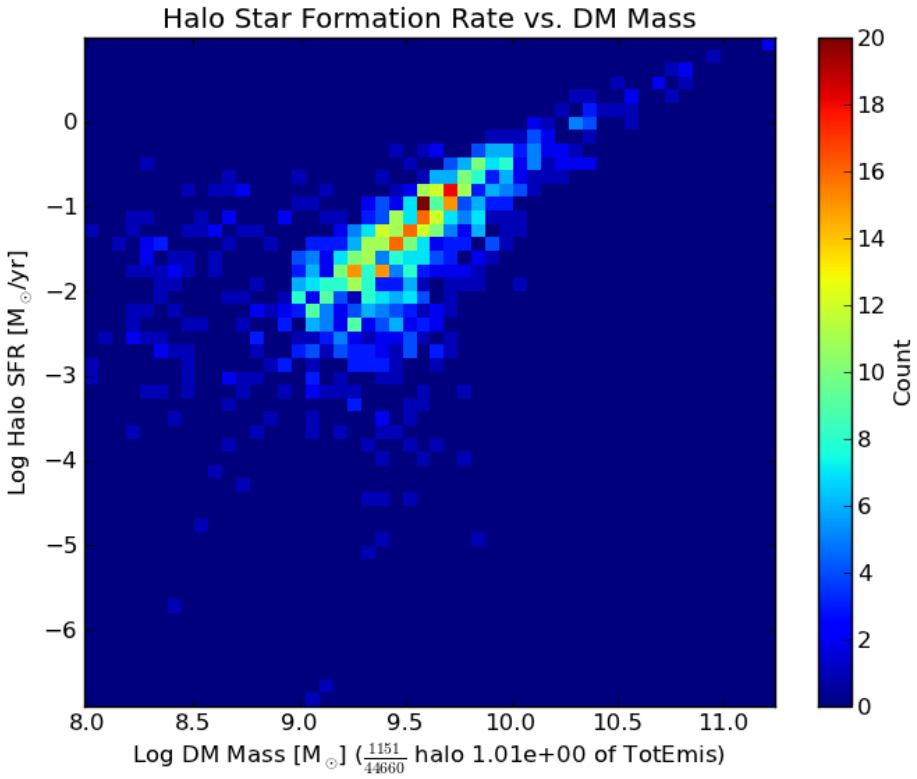

Figure 4.4: Star formation rate within each halo vs. the halo's dark matter mass at z=6 for *SED*. SFR decreases with decreasing dark matter mass with a visible trend. There is a significant deviation from the trend when the dark matter mass falls below $10^9 M_\odot$. This is data from 1151 star forming halos out of a total of 44660 halos, which contains 101% of the emissivity in the simulation. The total emissivity exceeded 100% due to some star forming region being double counted in halo analysis.

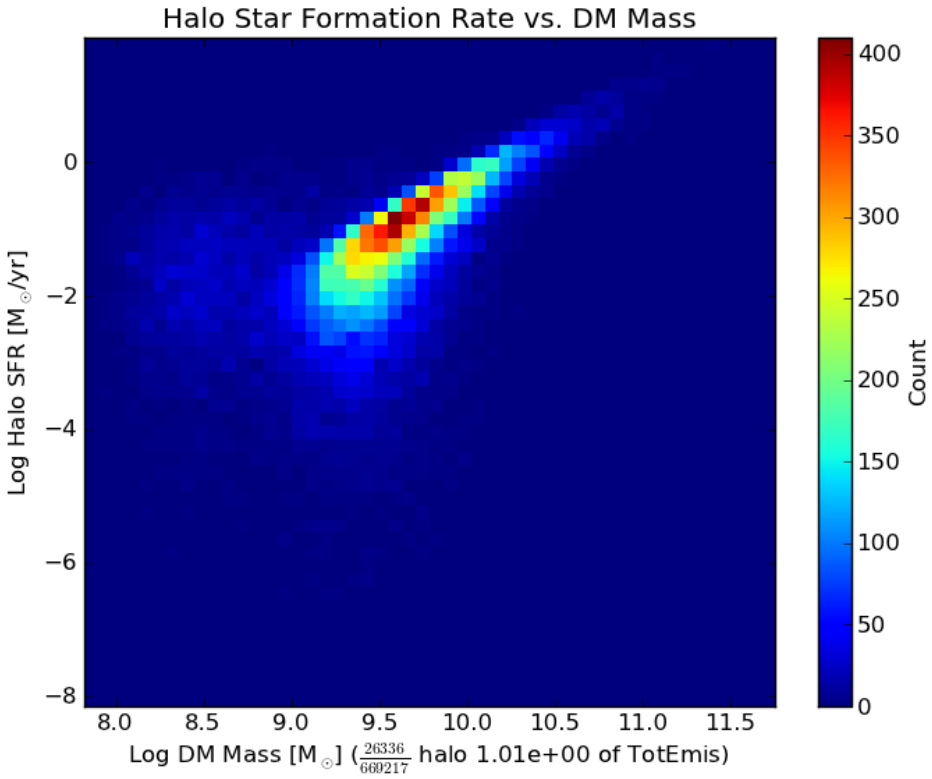

Figure 4.5: Star formation rate within each halo vs. the halo's dark matter mass at z=7.3 for *R32*. SFR decreases with decreasing dark matter mass with a visible trend. There is a significant deviation from the trend when the dark matter mass falls below $10^9 M_\odot$. This is data from 26336 star forming halos out of a total of 669217 halos, which contains 101% of the emissivity in the simulation. The total emissivity exceeded 100% due to some star forming regions being double counted in halo analysis.

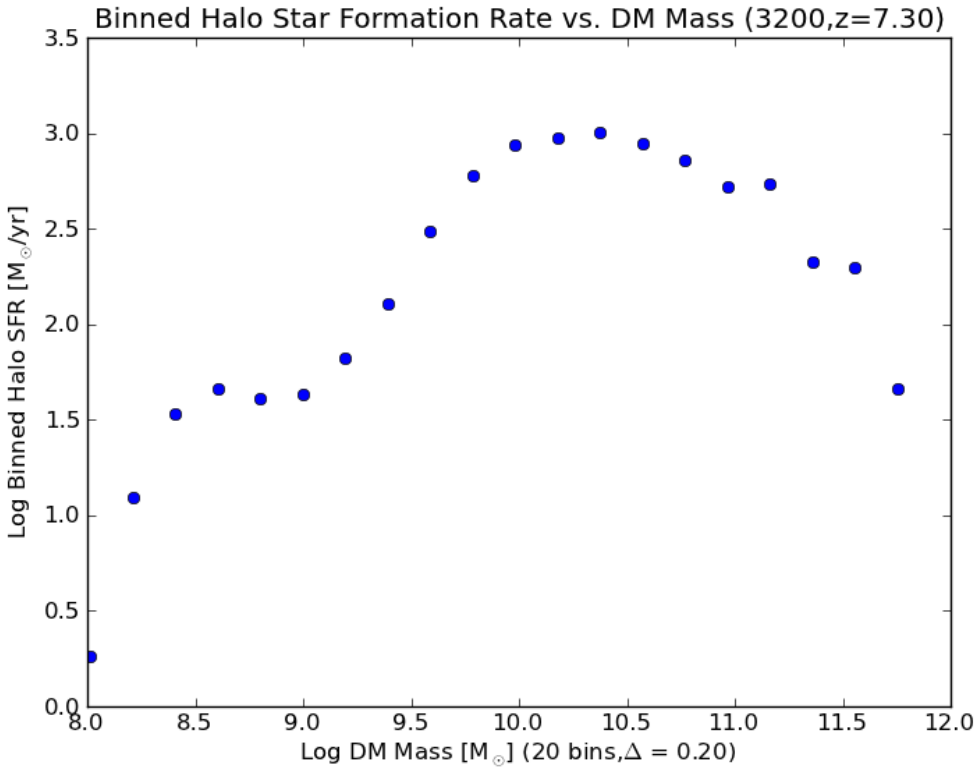

Figure 4.6: Sum of the binned star formation rate vs. halo dark matter mass from *R32* at z=7.3. This shows the order of magnitude drop in the total SFR per bin below $10^{9.7}\mathrm{M}_{\odot}$.

SFR in each bin drops by an order of magnitude over this halo mass range before reaching another plateau around $10^{1.5}\mathrm{M}_{\odot}\mathrm{yr}^{-1}$. This shows that the end of the trend of SFR is real, and not just dispersed into the larger cloud that spreads over different SFR values. We do not look at data for halos of dark matter mass below $10^{8}\mathrm{M}_{\odot}$ since in that regime we are limited by the mass resolution of this simulation.

4.5 Effects of Supernova and Star Formation Feedback

Here we investigate the origin of the suppression of star formation in low mass halos which we saw in the last section. Conventionally this is believed to be the consequence of two physical effects (Finlator et al., 2012; Geha et al., 2012): (1) reionization, which raises the gas temperature to $T \approx 10^4$ K, and hence its pressure, which allows it to escape the shallow potential wells of low mass galaxies; and (2) supernova energy feedback, in which gas is ejected from low mass galaxies kinetically. Here we compare three simulations, where *ADIAB* has neither cooling nor star formation, *NORAD* has star formation and supernova feedback turned on (which injects thermal energy into 27 neighboring cells (Smith et al., 2011)), and the *BSM* run has the addition of radiation transport with the FLD module turned on. We compare them by dividing the total gas mass in each dark matter mass bins of *NORAD* and *BSM* by the same quantity in the *ADIAB* run. This way, we can see the relative effects of adding supernovae, then adding radiation on the halo gas mass. We study gas mass because it feeds star formation, and we wanted a quantity we could measure in all three simulations.

In Figure 4.7, we plot the gas content of *BSM* and *SED* relative to *ADIAB* at z=5. Examining the green curve labeled *NORAD*/*ADIAB*, we see that if we add supernova feedback, the highest mass halos are having their gas blown away by the energetic explosion. In our feedback recipe, the SN energy injection rate is proportional to the SFR, which is much higher in the high mass halos. This may have caused the high mass halos to lose much of their gas. The halos with masses below $\sim 10^{9.7} M_\odot$ are not affected as much. Some of these low mass halos even have slightly higher gas content than halos of similar masses in the *ADIAB* with no supernova effects. This might be due to gas accretion onto the low mass halos from the gas blown out by the more massive halos. To confirm these hypotheses we have to compare the SN energy injection to the gravitational binding energy.

The blue line of *BSM*/*ADAIB* shows a more global effect. The added radiation decreases gas mass in halos across all mass ranges. The effect is more

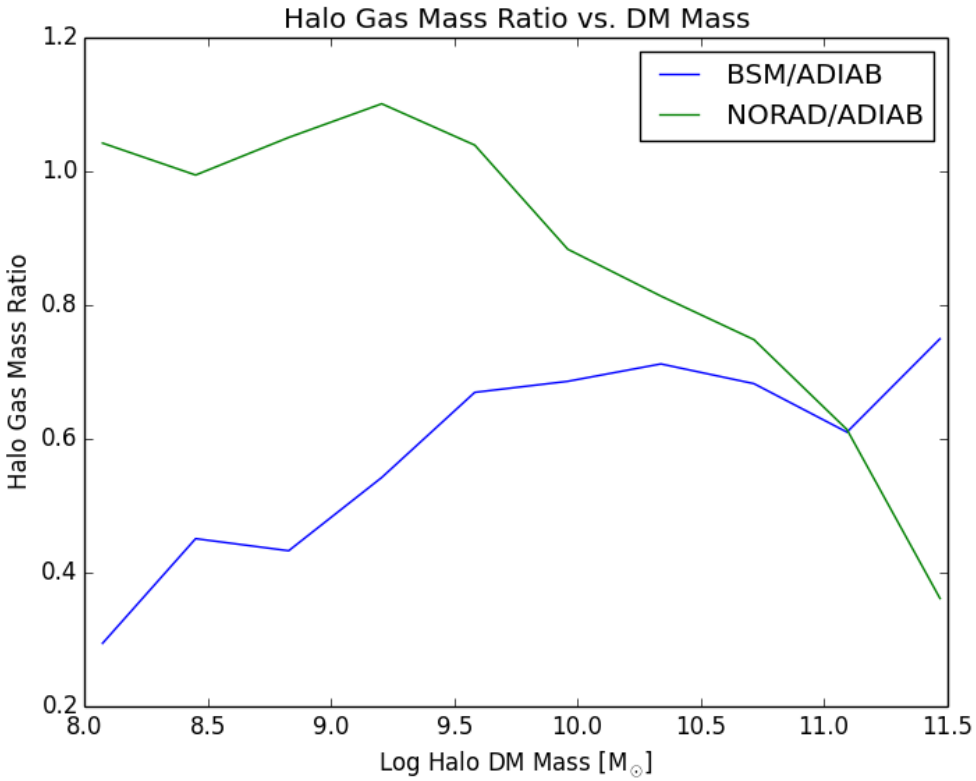

Figure 4.7: Halo gas mass ratio vs. dark matter mass for *BSM* and *SED* relative to *ADIAB* run at z=5.

apparent in the lower mass halos, but even the most massive halo feels the effect. Interestingly, the most massive halos in the *BSM* run have more gas mass relative to the *NORAD* simulation. This could be due to the non-linear nature of the feedback process of structure formation, supernova feedback, and radiation feedback. The radiation could have lowered the formation of new stars by heating up the gas, thus resulting in less energetic supernova feedback that blows away less gas, therefore retaining more gas as an end result. Another possibility is that the most massive halo is less efficient at turning gas into stars when radiation is present, therefore it has more gas than halos of similar masses in the *NORAD* simulation. Further study of the combined baryon mass (stars+gas) is warranted to draw any more convincing explanations. The proposed explanations are just speculations for now.

4.6 Halo Luminosity Function

To further validate our simulation against observations, we compare the simulations' luminosity function (LF) to those from observations. The LF is a measurement of how much do galaxies shine at a certain brightness level. Observers use the LF to try to determine the ionizing photon budget available to ionize the universe during EoR (Bunker et al., 2004; Bolton & Haehnelt, 2007). Therefore, it is important that we at least compare what our simulations yield in terms of the LF, or else we may over or under produce galaxies of different brightness compared to what was available in the early universe. In Figure 4.8, we plot in red the LF of *BSM* and in orange that of the *SED*, and compare the two with points in blue which are from Table 5 ($z\sim6$) of Bouwens et al. (2007). The error bars from the simulations are from one standard deviation of the available data points in each magnitude bin.

In the figure, we are able to roughly reproduce the observed luminosity function at the observable range ($-22 < M < -18$) at around the same redshift. Even with a relatively small sample of halos ($\sim$1,000), the standard deviation error bars in each mass bin are roughly the same size as those from observations. As a prediction we may even see a turn over of the luminosity function in the fainter end. However, the turnover may be due to the missing under-resolved low mass halo from the limitations of the mass resolution. Further simulations with better mass resolutions may be needed to definitively say whether the turn over of the LF will happen around a magnitude of -14 to -16.

We also note some limitations on this plot. The first limitation is that the magnitude plotted from our data is the bolometric magnitude, as opposed to the observational data which uses the AB magnitude system (Oke & Gunn, 1983; Bouwens et al., 2007). This is because our radiation field uses the grey approximation averaging over all frequencies, therefore it is not frequency dependent. The result is that we can only use the overall bolometric scale for magnitude calculations. Second, we see that we do not sample the brightest end of the LF well at this redshift. This is due to the physical size of the simulation. Given a bigger box with more large scale power in the matter power spectrum, we would have big-

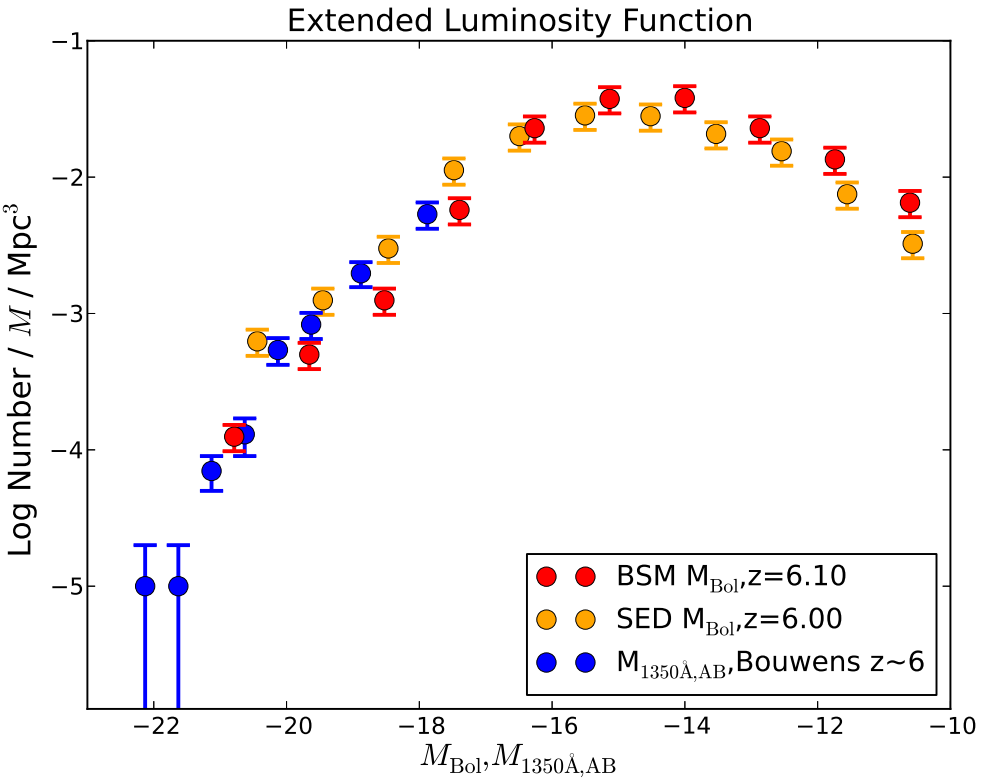

Figure 4.8: Red: Luminosity function measured in bolometric magnitude from *BSM*; Orange: Luminosity function measured from *SED*; Blue: Luminosity function measured in 1350Å, AB magnitude from Table 5 (z∼6) from Bouwens et al. (2007).

ger objects that are forming more luminous sources. We are expecting the same analysis on *R32* to give us brighter points near $M_{\rm Bol}$ ∼-22.

4.7 Ionization History

Finally, we compare the ionization histories of our three radiation simulations. The ionization history of the universe is one deceptively simple diagram. Usually it is regarded as the fractional volume of the universe that is deemed "ionized" (we continue to use the Well Ionized level of less than one part neutral in 10^3 hydrogen atoms) vs. redshift z. On the surface, this may tell us only when the universe starts to get significantly ionized and when EoR ends. Often people use volume fractions of 20% and 80% to set the duration of EoR, but as we have shown, the extended tail near reionization completion is rather important. It is hard to simulate all the physics involved in EoR accurately. By investigating the ionization history, photon production, and recombination rates we wish to understand more about the interplay between the physical processes (see §3.6).

Since so many processes are involved in modeling the flattening tail end of the volume fraction of ionized hydrogen ($Q_{\rm HII}$, to Well Ionized level), we want to make sure that $Q_{\rm HII}$ asymptotically approaching unity is not an anomaly of the *BSM* simulation (discussed in §3.7.3). We plot in Figure 4.9, $Q_{\rm HII}$ vs. z for the radiation runs *BSM*, *SED*, *R32*. The blue curve is the $Q_{\rm HII}$ evolution of *BSM*, green is *SED*, and red is the mean for *R32*, and the yellow region is the +/- one standard deviation from the mean of *R32*. Standard deviation comes from analyzing the bigger simulation *R32* in 64 cubic subvolumes of size (20 Mpc)^3. Although Q can never exceed 1.0, the yellow region where it exceeded the maximum value is just an artifact of plotting + and - of one standard deviation. We clearly see that having a different SED (softer spectrum but with more energy distributed toward the ionization threshold of hydrogen), enables the *SED* run to achieve a higher $Q_{\rm HII}$ at earlier z than 6.0. The bigger box with more matter power and hence more total star formation in *R32* has a similar effect on $Q_{\rm HII}$ compared to *BSM*, reaching higher $Q_{\rm HII}$ quicker before z of 6.0.

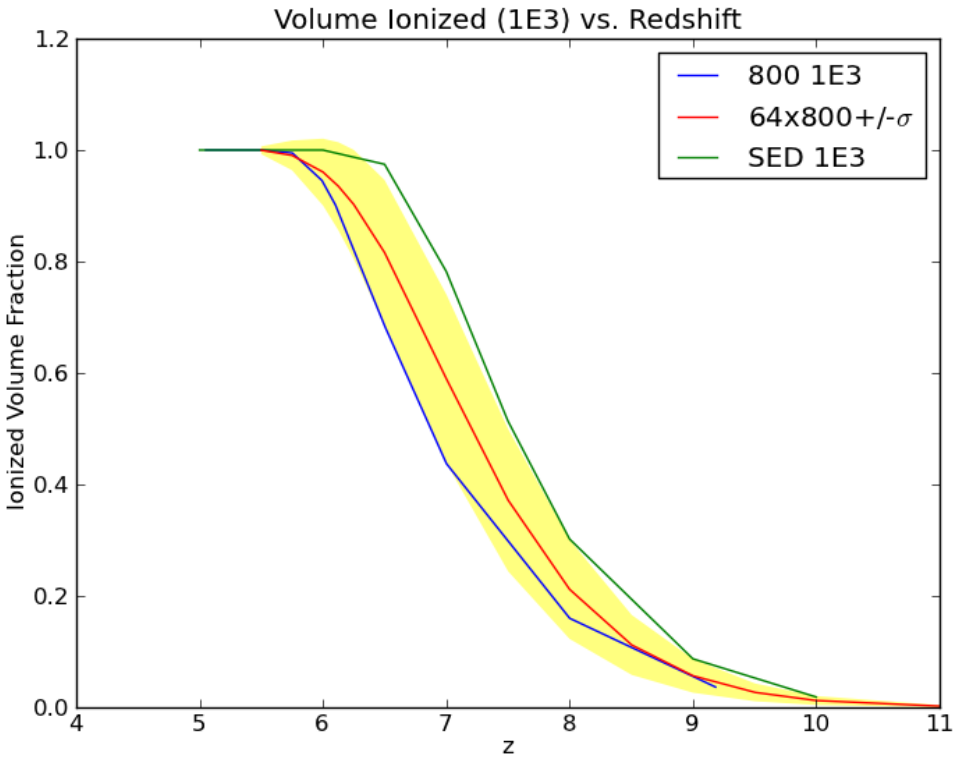

Figure 4.9: Plot of ionized volume fraction (to Well Ionized level) vs. redshift. Blue: *BSM*; Green: *SED*; Red: mean of *R32*; Yellow: mean of *R32*$\pm\sigma$.

This is the expected behavior given the different physics we put into the simulations. What is interesting and perhaps even surprising is, again, the tail end of $Q_{\rm HII}$ as it approaches unity. Notice how the yellow region, the standard deviation for *R32* narrows after $z \sim 6.0$. And around the same z both *BSM* and *SED* also converge to the same ionized volume fraction. *SED* has a earlier rise, but also flattens earlier, whereas *BSM* gets to the same ionized fraction later, but catches up at the end. There was no input parameter that directly forced these simulations to finish EoR at the same time, so having them all finish EoR at around the same time is unexpected.

Chapter 5

Conclusions and Future Work

Here I will summarize the conclusions from the first two chapters of the thesis (Chapter 2 and Chapter 3), and update the last chapter based on our latest work. In Chapter 2, we find that we were able to implement a radiation transport module in Enzo. The tests show that the code is parallelized to be scalable, and is sufficiently fast to finish our cosmological simulation. The accuracy of the FLD solver is verified and validated through comparisons with analytical solutions and other numerical solutions. With the code deemed acceptable, we used it to run a moderate size cosmology run aimed at revealing the details of physical processes during the epoch of reionization. Although there are known shortcomings to using the FLD approximation for radiation transport, principally the lack of shadows behind opaque clouds, we have seen from tests that on a cosmological scale, those errors should not affect the end results we care about such as ionization fraction in the volume.

In Chapter 3, we used the methods described in Chapter 2 in a cosmological simulation that gives us a moderate sample of the universe. We matched the observed star formation rate density as a starting point to investigate the mechanics of accounting for photoionizations and recombinations. We found support for the "Inside-Out" scenario at the beginning of reionization as it progressed in a "photon starved" environment. Later when the universe is in a "photon abundant" situation, the left over neutral region is ionized in a generally "Outside-In" fashion, and of course the details depend on where one draws the line for gas characterized as

ionized. Upon detailed analysis of the clumping factor, we concluded that it is unreliable in predicting the end of reionization using the instantaneous model of Madau et al. (1999) and one must account for history effects when calculating for $Q_{\rm HII}$. This is because the recombination time is not much smaller than the Hubble time, an argument used originally to justify the instantaneous balance of recombinations and photoionizations. We eventually found an appropriate way of calculating for an effective (*not* a volume averaged) recombination time for the purpose of estimating $Q_{\rm HII}$. We also noticed that the sources of ionization term in the original formulation of the Madau et al. formula should be photoionization instead of photon production rate in the numerator. The denominator should be the average density of the ionized bubble region where the ionization front has passed. With these appropriate modifications, we are able to get good ($\sim O(1\%)$) agreement of $Q_{\rm HII}$ from the formula with our simulation. We hope the observation and simulation communities find the distinction between photoionization rate and photon production rate to be a step in the right direction in estimating the photon budget required to achieve end of epoch of reionization.

In Chapter 4, we set out to analyze various simulations with different physics input. We want to compare and contrast the different simulations to see what happens when we vary the input physics slightly and the result of having radiation transport. We first look at the effect of having slightly varying physics on halo star formation rates. We showed that in the three runs *BSM*, *SED*, *R32* that even at different z we see the same halo star formation vs halo dark matter mass trend, which drops out starting below the dark matter mass of around 10^{10} to $10^{9}{\rm M}_{\odot}$. The phenomenon indicates that there is a halo mass threshold below which star formation is much reduced by some mechanism which we do not fully understand, merely observe at this point. Due to the limitation of previous version of the analysis code, we were not able to analyze the stellar mass content of the halos derived from this ellipsoidal container, but since this limitation no longer exists, it is something that we plan to look into for a much better comparison with the literature.

There are limitations to our simulations, many of them are discussed in

§3.7.2. However, for the newer topics we want to investigate in Chapter 4, we will mention a few more because they are now more relevant. There is a possibility that the lower mass halos around $10^8 M_\odot$ are not resolved enough spatially. This will affect their ability to form stars and contribute to the ionization locally. In fact, they may become sinks for the radiation coming from larger halos instead, thus skewing the result of how many photons per hydrogen atom are needed to ionize the IGM. If they do indeed form stars, this will also change the 2D histogram and possibly continue the trend of star formation to below $10^9 M_\odot$. What is needed is to check the *NORAD* star formation rate for these low mass halos against the star formation rate of halos in *BSM* or *SED*.

Throughout this thesis, we investigated ionization due to photons, but there is also collisional ionization happening that the simulations keep track of. This effect is significant in the high density and high temperature regions, where supernova feedback raises the temperature to near 10^7K and the gas is dense locally. Most of our later results are based on the thresholded regions where we mask out these dense hot spots, so we do not expect our results to be affected much even if we do account for this type of ionization. We also failed to count the ionizations that come from singly or doubly ionized helium, but due to their relative abundance, we do not expect a difference much more than 10%. We also neglected the Hubble term by using the differential form from Madau et al. (1999) because we believe that is a small contribution, but we will investigate further in future work.

In Bouwens et al. (2011a), the calculation of star formation rate density and luminosity function required the observers to make dust corrections. When we did the SFRD comparison it is with points after the dust corrections. In the future, we could do some comparison of the *R32*'s SFRD and LF with dust and compare them to the uncorrected observations. If dust is taken into account, this can potentially change the amount of ionizations in the intergalactic medium.

As suggested in Geha et al. (2012), the apparent quenching of star formation rate within small mass halos can be due to a number of things. The proximity (2$\sim$4 virial radii) from a much larger halo as neighbor would be a likely culprit. A low mass halo's radiation pressure from stellar and SN sources can blow away the

gas within the halo, preventing further star formation. Another possibility is the neighboring high mass halo's radiation may simply be heating the gas in the smaller halo, preventing collapse of gas in the smaller halo to form stars. Another culprit could be quenching due to ram stripping if the smaller halo passes by the much larger halo in its orbit. The presence of AGN feedback or stellar wind feedback due to the halo's intrinsic star formation may also hinder the formation of newer stars.

A point that may need reconciliation is the mass cutoff for the star formation trend seen in Figures 4.3, 4.4, 4.5. The mass cut off may seem like 10^9, but in Figure 4.6, the drop off is shown to start around $10^{10}M_{\odot}$ and ends around $10^9M_{\odot}$. It is unclear whether following the same proxy for SFR (Balogh et al., 1999) that was used in Geha et al. (2012) would show the trend ending at the same halo mass. A second point that needs addressing is that the point of cut off used in Geha et al. (2012) is based on stellar masses, but the graph we plotted is the halo's dark matter mass. This will require the halo analysis to include the stellar content which we are ready to tackle in the near future. A third point is that although the trend ends, the lower mass halos have a large scatter of star formation rates. In other words, there are low mass halos with much less star formation due to quenching, but also some with much bigger star formation than expected had the trend continued to this mass regime. Some possible explanations could be the star formation is newly collapsed halos that are just forming due to the hierarchical structure formation, lower masses collapse later in time. Or that these small mass halos have undergone an episode of recent merger with a neighbor, therefore experiencing enhanced star formation for a short duration.

The stellar content would be an easy check with simulation data, but the others such as proximity to a larger neighbor, ram stripping due to trajectory, radiation pressure from winds hypothesis will require very detailed analysis of the halo properties and possibly their environments. One thing that we can do is analyze the halos and see if any other halo centers are within a certain number of virial radii from the larger host. We need to re-run the halo catalog to include more information than is available right now (primarily to include the stellar content).

We can plot the SFR vs. distance to the host halo as a 2D scatter plot, with the size of the points indicating the halo's total mass, and the color of the dots indicating either the ratio of of stellar to gas mass, or stellar to dark matter mass. We should be able to draw some preliminary conclusion based on the graph to say whether proximity is an effect pending the plot's outcome.

We will also need to find a way to emulate the spectral index in order to do an apples-to-apples comparison for the cut off of SFR (Balogh et al., 1999). We currently do not have AGN feedback implemented in our subgrid model, therefore we will not be able to address that effect in this version of *Enzo*. If we are to use the public version of *Enzo*, however, we should be able to investigate this effect further.

In the near future, we would like to analyze and compare the effects of having a softer SED, between the *BSM* and *SED* run. We may want to be able to adjust the SED to properly represent the UV sources of radiation, which means going with the SED from the *SED* run. In addition, we would want to use this learning experience to gauge the effects of adding X-ray, a much harder form of radiation, and study the detail mechanism of Helium pre-heating and its effect on EoR. The different SED already have an effect on the $Q_{\rm HII}$, so we should also expect to see an effect by the addition of hard X-ray photons. The answer will come when more simulations are run, including the stellar content from the current suite of simulations. We need the analysis at more redshifts, so that a more substantial comparison can be made at different epoch during EoR, rather than the current single snapshots.

We also touched on the possibility that high redshift galaxies exhibit a turn over for the luminosity function. This may affect results that use a photon budget derived from the luminosity function. Together with the modification to the Madau et al. (1999) formula, this may require many to revisit predictions or limits set by the computational, semi-analytic, and observational community members such as Bunker et al. (2004); Bolton & Haehnelt (2007); Haardt & Madau (2012); Finkelstein et al. (2012); Robertson et al. (2013); Wang (2013) to name a few. Perhaps even new analysis that link together high, intermediate, and low redshift

observation data is needed in a comprehensive manner such as Kuhlen & Faucher-Giguère (2012), constraining parameter space by matching lower z observation of the luminosity function.

We also note the limitations of our simulations as discussed in §3.7. Our star particle maker uses the Cen & Ostriker (1992) recipe with the addition of distributed feedback from Smith et al. (2011). This is a simple and easy to implement subgrid model that neglects all the physics that is happening in the sub-kpc scale below our resolution. Therefore, it is possible for galaxies to exhibit a different SFR and hence a different overall LF if we were to change our star maker recipe. This remains to be checked and its effect quantified by people that focus on galactic scale star formation. Unfortunately, the lack of dynamic range due to limited CPU resources and scalable code is still very much a bottleneck in the field of computational cosmology simulations.

Finally, we note the interesting phenomenon that reionization completes at roughly the same redshift for three simulations with different SFR densities (compare Figure 4.1) This is not what is predicted by analytic models of reionization. This could be due to any number of things, but we suspect that this could the result of there being a favorable time to reionize the universe. Given the fact that we varied the SED, box size, and yet arrived at a sort of convergence for when more than 99.9% of the universe is considered to be ionized, we may be seeing a stability of the solution in the highly non-linear system of equations that describe the physics of EoR. Of course this result is only preliminary, and it awaits to be seen just how far do we have to nudge different parameters to break away from this stable point. Or, maybe it is not possible to reionize the universe at other redshifts given the physical laws we observe today at all. Either way, the epoch of reionization contains many other mysteries and discoveries that await us.

This research was partially supported by National Science Foundation grants AST-0808184 and AST-1109243 and Department of Energy INCITE award AST025 to MLN and DRR. Simulations were performed on the *Kraken* supercomputer operated for the Extreme Science and Engineering Discovery Environment (XSEDE) by the National Institute for Computational Science (NICS), ORNL with support

from XRAC allocation MCA-TG98N020 to MLN. MLN, DRR and GS would like to especially acknowledge the tireless devotion to this project by our co-author Robert Harkness who passed away shortly before this manuscript was completed.

Bibliography

2010, Enzo – Astrophysical Adaptive Mesh Refinement, ver. 2.0, http://enzo.googlecode.com

2011, HYPRE Code Project Page, http://www.llnl.gov/CASC/hypre/software.html

Abel, T., Anninos, P., Zhang, Y., & Norman, M. L. 1997, New A., 2, 181

Abel, T., Bryan, G. L., & Norman, M. L. 2002, Science, 295, 93

Abel, T., & Haehnelt, M. G. 1999, ApJ, 520, L13

Ahn, K., Iliev, I. T., Shapiro, P. R., et al. 2012, ApJ, 756, L16

Anninos, P., Zhang, Y., Abel, T., & Norman, M. L. 1997, New Astronomy, 2, 209

Balogh, M. L., Morris, S. L., Yee, H. K. C., Carlberg, R. G., & Ellingson, E. 1999, ApJ, 527, 54

Barkana, R., & Loeb, A. 2007, Reports on Progress in Physics, 70, 627

Berger, M. J., & Colella, P. 1989, Journal of Computational Physics, 82, 64

Bolton, J. S., & Haehnelt, M. G. 2007, MNRAS, 382, 325

Bouwens, R. J., Illingworth, G. D., Franx, M., & Ford, H. 2007, ApJ, 670, 928

Bouwens, R. J., Illingworth, G. D., Labbe, I., et al. 2011a, Nature, 469, 504

Bouwens, R. J., Illingworth, G. D., Oesch, P. A., et al. 2011b, ApJ, 737, 90

—. 2012, ApJ, 752, L5

Bromm, V., & Larson, R. B. 2004, ARA&A, 42, 79

Bryan, G. L., Machacek, M., Anninos, P., & Norman, M. L. 1999, ApJ, 517, 13

Bryan, G. L., Norman, M. L., Stone, J. M., Cen, R., & Ostriker, J. P. 1995, Computer Physics Communications, 89, 149

Bunker, A. J., Stanway, E. R., Ellis, R. S., & McMahon, R. G. 2004, MNRAS, 355, 374

Carilli, C. 2004, Radio Studies of Cosmic Reionization, http://www.aoc.nrao.edu/ ccarilli/TALKS.OLD.shtml

Cen, R., & Ostriker, J. P. 1992, ApJ, 399, L113

Ciardi, B., Ferrara, A., Marri, S., & Raimondo, G. 2001, MNRAS, 324, 381

Ciardi, B., Stoehr, F., & White, S. D. M. 2003, MNRAS, 343, 1101

Colella, P., & Woodward, P. R. 1984, J. Comp. Phys., 54, 174

Cooray, A., & Sheth, R. 2002, Phys. Rep., 372, 1

Cowie, L. L., Barger, A. J., & Trouille, L. 2009, ApJ, 692, 1476

Eisenstein, D. J., & Hu, W. 1999, ApJ, 511, 5

Fan, X., Carilli, C. L., & Keating, B. 2006, ARA&A, 44, 415

Fernandez, E. R., & Shull, J. M. 2011, ApJ, 731, 20

Finkelstein, S. L., Papovich, C., Ryan, R. E., et al. 2012, ApJ, 758, 93

Finlator, K., Oh, S. P., Özel, F., & Davé, R. 2012, MNRAS, 427, 2464

Finlator, K., Özel, F., & Davé, R. 2009a, MNRAS, 393, 1090

Finlator, K., Özel, F., Davé, R., & Oppenheimer, B. D. 2009b, MNRAS, 400, 1049

Furlanetto, S. R., Hernquist, L., & Zaldarriaga, M. 2004a, MNRAS, 354, 695

Furlanetto, S. R., McQuinn, M., & Hernquist, L. 2006, MNRAS, 365, 115

Furlanetto, S. R., Zaldarriaga, M., & Hernquist, L. 2004b, ApJ, 613, 1

Geha, M., Blanton, M. R., Yan, R., & Tinker, J. L. 2012, ApJ, 757, 85

Gnedin, N. Y. 2000a, ApJ, 535, 530

—. 2000b, ApJ, 542, 535

Gnedin, N. Y., & Abel, T. 2001, New A., 6, 437

Gnedin, N. Y., & Ostriker, J. P. 1997, ApJ, 486, 581

Gunn, J. E., & Peterson, B. A. 1965, ApJ, 142, 1633

Haardt, F., & Madau, P. 2012, ApJ, 746, 125

Hayes, J. C., & Norman, M. L. 2003, Ap. J. Supp., 147, 197

Hockney, R. W., & Eastwood, J. W. 1988, Computer simulation using particles, ed. R. W. Hockney & J. W. Eastwood

Hui, L., & Gnedin, N. Y. 1997, MNRAS, 292, 27

Iliev, I. T., Mellema, G., Pen, U.-L., et al. 2006, MNRAS, 369, 1625

Iliev, I. T., Whalen, D., Mellema, G., et al. 2009, MNRAS, 400, 1283

Jarosik, N., Bennett, C. L., Dunkley, J., et al. 2011, ApJS, 192, 14

Jena, T., Norman, M. L., Tytler, D., et al. 2005, MNRAS, 361, 70

Klypin, A. A., Trujillo-Gomez, S., & Primack, J. 2011, ApJ, 740, 102

Komatsu, E., Smith, K. M., Dunkley, J., et al. 2011, ApJS, 192, 18

Kuhlen, M., & Faucher-Giguère, C.-A. 2012, MNRAS, 423, 862

Labbé, I., González, V., Bouwens, R. J., et al. 2010, ApJ, 708, L26

Madau, P., Haardt, F., & Rees, M. J. 1999, ApJ, 514, 648

McQuinn, M., Oh, S. P., & Faucher-Giguère, C.-A. 2011, ApJ, 743, 82

Miralda-Escudé, J., Haehnelt, M., & Rees, M. J. 2000, ApJ, 530, 1

Mirocha, J., Skory, S., Burns, J., & Wise, J. 2012, ApJ, 756

Mitra, S., Ferrara, A., & Choudhury, T. R. 2013, MNRAS, 428, L1

Morel, J. E. 2000, J. Quant. Spectrosc. Radiat. Transfer, 65, 769

Norman, M. L., & Bryan, G. L. 1999, in Astrophysics and Space Science Library, Vol. 240, Numerical Astrophysics, ed. S. M. Miyama, K. Tomisaka, & T. Hanawa, 19

Norman, M. L., Bryan, G. L., Harkness, R., et al. 2007, Petascale Computing: Algorithms and Applications, ed. D. Bader (CRC Press)

Norman, M. L., Paschos, P., & Abel, T. 1998, Mem. Soc. Astron. Italiana, 69, 271

Norman, M. L., Reynolds, D. R., & So, G. C. 2009, in Recent Directions in Astrophysical Quantitative Spectroscopy and Radiation Hydrodynamics (AIP)

Norman, M. L., Reynolds, D. R., So, G. C., & Harkness, R. P. 2013, ArXiv e-prints

Oesch, P. A., Bouwens, R. J., Illingworth, G. D., et al. 2013, ArXiv e-prints

Oke, J. B., & Gunn, J. E. 1983, ApJ, 266, 713

O'Shea, B. W., Bryan, G., Bordner, J. O., et al. 2004, Adaptive Mesh Refinement – Theory and Applications, Lecture Notes in Computational Science and Engineering (Springer)

Osterbrock, D. E. 1989, Astrophysics of Gaseous Nebulae and Active Galactic Nuclei (Mill Valley, California: University Science Books)

Osterbrock, D. E., & Ferland, G. J. 2006, Astrophysics of Gaseous Nebulae and Active Galactic Nuclei, 2nd edn. (University Science Books), 38

Paschos, P. 2005, PhD thesis, University of Illinois at Urbana-Champaign

Pawlik, A. H., Schaye, J., & van Scherpenzeel, E. 2009, MNRAS, 394, 1812

Petkova, M., & Springel, V. 2009, MNRAS, 396, 1383

—. 2011a, MNRAS, 415, 3731

—. 2011b, MNRAS, 412, 935

Planck Collaboration, Ade, P. A. R., Aghanim, N., et al. 2013, ArXiv e-prints

Pritchard, J. R., & Loeb, A. 2012, Reports on Progress in Physics, 75, 086901

Raicevic, M., & Theuns, T. 2011, Monthly Notices of the Royal Astronomical Society: Letters

Razoumov, A. O., Norman, M. L., Abel, T., & Scott, D. 2002, ApJ, 572, 695

Reynolds, D. R. 2010, gFLDSplit: A FLD-based radiation and chemistry solver for Enzo, Tech. rep., Southern Methodist University, http://*enzo*.googlecode.com

Reynolds, D. R., Hayes, J. C., Paschos, P., & Norman, M. L. 2009, Journal of Computational Physics, 228, 6833

Ricotti, M., Gnedin, N. Y., & Shull, J. M. 2002, The Astrophysical Journal, 575, 33

Robertson, B. E., Ellis, R. S., Dunlop, J. S., McLure, R. J., & Stark, D. P. 2010, Nature, 468, 49

Robertson, B. E., Furlanetto, S. R., Schneider, E., et al. 2013, ApJ, 768, 71

Schaye, J. 2001, ApJ, 559, 507

Shapiro, P. R., & Giroux, M. L. 1987, Ap. J., 321, L107

Shapiro, P. R., Giroux, M. L., & Babul, A. 1994, ApJ, 427, 25

Shapiro, P. R., Iliev, I. T., & Raga, A. C. 2004, MNRAS, 348, 753

Shin, M.-S., Trac, H., & Cen, R. 2008, ApJ, 681, 756

Shull, J. M., Harness, A., Trenti, M., & Smith, B. D. 2012, ApJ, 747, 100

Skory, S., Turk, M. J., Norman, M. L., & Coil, A. L. 2010, ApJS, 191, 43

Smith, B. D., Hallman, E. J., Shull, J. M., & O'Shea, B. W. 2011, ApJ, 731, 6

Sokasian, A., Abel, T., Hernquist, L., & Springel, V. 2003, MNRAS, 344, 607

Sokasian, A., Abel, T., & Hernquist, L. E. 2001, New A, 6, 359

Sokasian, A., Yoshida, N., Abel, T., Hernquist, L., & Springel, V. 2004, MNRAS, 350, 47

Songaila, A. 2004, AJ, 127, 2598

Springel, V., White, S. D. M., Jenkins, A., et al. 2005, Nature, 435, 629

Stone, J. M., Mihalas, D., & Norman, M. L. 1992, ApJS, 80, 819

The Enzo Collaboration, Bryan, G. L., Norman, M. L., et al. 2013, ArXiv e-prints

Trac, H., & Cen, R. 2007, ApJ, 671, 1

Trac, H., Cen, R., & Loeb, A. 2008, ApJ, 689, L81

Trac, H. Y., & Gnedin, N. Y. 2011, Advanced Science Letters, 4, 228

Trenti, M., Smith, B. D., Hallman, E. J., Skillman, S. W., & Shull, J. M. 2010, ApJ, 711, 1198

Turk, M. J., Smith, B. D., Oishi, J. S., et al. 2011, ApJS, 192, 9

Valageas, P., & Silk, J. 1999, AAP, 347, 1

Wang, F. Y. 2013, A&A, 556, A90

Warren, M. S., Abazajian, K., Holz, D. E., & Teodoro, L. 2006, ApJ, 646, 881

Willott, C. J., Delorme, P., Reylé, C., et al. 2010, AJ, 139, 906

Wise, J. H., & Abel, T. 2011, MNRAS, 414, 3458

Wise, J. H., & Cen, R. 2009, ApJ, 693, 984

Wise, J. H., Turk, M. J., Norman, M. L., & Abel, T. 2012, ApJ, 745, 50

Wyithe, J. S. B., Hopkins, A. M., Kistler, M. D., Yüksel, H., & Beacom, J. F. 2010, MNRAS, 401, 2561

Xu, H., Wise, J. H., & Norman, M. L. 2013, ArXiv e-prints

Yajima, H., Choi, J.-H., & Nagamine, K. 2011, MNRAS, 412, 411

Yoshida, N., Abel, T., Hernquist, L., & Sugiyama, N. 2003, ApJ, 592, 645

Zahn, O., Lidz, A., McQuinn, M., et al. 2007a, ApJ, 654, 12

—. 2007b, ApJ, 654, 12

Zahn, O., Mesinger, A., McQuinn, M., et al. 2011, MNRAS, 414, 727